NTNU

Norwegian University of
Science and Technology

Corrosion fatigue of an extruded 7046 alloy

Kyrre Stefansson Christiansen

Materials Science and Engineering (MTMT)
Submission date: July 2018
Supervisor: Ola Jensrud, IMA
Co-supervisor: Hans Jørgen Roven, IMA
Otto Lunder, IMA

Norwegian University of Science and Technology
Department of Materials Science and Engineering

Preface

This thesis is submitted in fulfillment of the degree Master of Science (MSc). The work was conducted at the Department of Materials Science and Engineering during the spring semester of 2018, at the Norwegian University of Science and Technology (NTNU). The thesis have been done in collaboration with Benteler Aluminium Systems Norway AS.

I would like to express my deepest gratitude to my supervisor, Professor Ola Jensrud, and co-supervisors Professor Otto Lunder and Professor Hans Jørgen Roven for much appreciated guidance throughout this work. Further I would also like to thank Trygve Lindahl Schanke for help at the metallography laboratory, Pål Skaret for help with fatigue- and tensile testing and Yingda Yu for help at the EM laboratory. Thanks are also due to Helen Langeng, SINTEF, for providing me with the chambers used for corrosion fatigue testing. Final thanks go to Lars Lodgaard, Benteler, for providing the material and participating in discussions of the results obtained in this thesis.

The aim of this thesis is to achieve a better understanding of the corrosion fatigue properties of a 7046 alloy with emphasis on understanding how the corrosive environment effects the material, in order to understand the applicability of this alloy in automotive parts. The 7xxx alloys are among the strongest aluminium series, but is in return one of the series most prone to corrosion.

I declare that this master´s thesis is done independently and in accordance with the regulations at NTNU.

Abstract

The corrosion fatigue properties of a 7046 alloy were investigated and compared to previously reported work by SINTEF on the same alloy tested in air. To establish the corrosion fatigue properties, samples were either fatigue tested in a 5 wt% NaCl solution or pre-corroded in the same solution and subsequently tested in laboratory air. For the fatigue testing in 5 wt% NaCl solution, both T6 and T7 tempered samples were considered. To better understand how the corrosive environment influences the samples, SEM was used.

The simultaneous effect of corrosion and fatigue was found to have a detrimental effect on fatigue life for this alloy, with a clearly reduced lifetime at all tested stress amplitudes. Additional heat treatment to T7 condition did not yield any lifetime differences compared to T6, suggesting a similar crack initiation mechanism for both temper states. For pre-corroded samples, lifetime differences were only found at longer exposure times (1 week and more).

For the samples tested in 5 wt% NaCl, an initiation mechanism caused by oxide film rupture is proposed. For the samples pre-corroded for longer times (1 week and more), corrosion pits are thought to be the site for crack initiation.

Sammendrag

Egenskapene til en 7046 aluminiumslegering i et korrosivt miljø ble undersøkt og sammenlignet med tidligere arbeid av SINTEF på den same legeringen i luft. For å stadfeste korrosjonsutmattingegenskapene ble prøvestaver enten utmattingtestet i en 5 wt% NaCl løsning eller for-korrodert i den samme løsningen og deretter testet i luft. For utmattingtestingen i 5 wt% NaCl løsningen, ble bade temperaturtilstand T6 og T7 vurdert. For å øke forståelsen av hvordan det korrosive miljøet påvirker prøvene ble SEM brukt.

Den simultane effekten av korrosjon og utmatting hadde en svært negativ effekt på levetiden til denne legeringen, noe som var synlig ved alle spenninger. Ekstra varmebehandling til T7 tilstand ga ikke noen forskjell i levetid sammenlignet med T6, noe som antyder at sprekkinitieringen var lignende for begge temperaturtilstandene. For for-korroderte prøver var det kun mulig å se forskjell i levetid ved lengre eksponeringstider (1 uke eller mer).

For prøvestavene utmattingtestet i saltløsningen ble en initieringsmekanisme forårsaket av en sprukket oksidfilm foreslått. For prøver som ble for-korrodert ved lengre tider (1 uke eller mer), ble korrosjonsgroper foreslått som initieringsmekanisme.

Contents

1. Introduction

The increasing focus on improving fuel economy, triggered by concerns over global warming combined with stricter emission policies, has had a significant impact on the material choice in the automotive industry. An obvious way of reducing emissions is by weight reduction. By replacing steel with Aluminium, a weight reduction of 20-30% is possible. [1] A lighter car will influence the fuel economy both directly and indirectly. Directly in the way that less energy is required for acceleration, and indirectly as a smaller engine is required in a lighter car. The use of aluminium in automotive components is not new, and its history can be traced as far back as 1922[2]. However, its use was limited for a long time due to less developed manufacturing processes and higher costs. In the last 30 years, the use of aluminium components in cars have been increasing steadily. Mainly as cast engine blocks and engine parts[1, 3], but in recent years also safety critical components like suspension control arms and brake components where steel used to dominate.

Automotive parts are subjected to varying loads, and fatigue is an important factor to consider. Fatigue studies have been conducted for more than 150 years, and fatigue is still of major concern industrially. Estimations show that 90% of failures of mechanical art are due to fatigue. [4]

Automotive parts are exposed to varying environmental conditions, often in combination with varying loads, i.e. a combination of corrosion and fatigue. A corrosive environment amplifies fatigue, and the combined action of fatigue and corrosion is known as corrosion fatigue. A current example, in an automotive context, is salted winter roads. For a car to be sustainable in such an environment, it is of high importance that it is resistant both to the corrosive environment and fluctuating loads and vibrations. With this in mind, the importance of studying corrosion fatigue is apparent.

2. Theory

2.1 Aluminium

Aluminium is the most common metallic material in the earth crust, and has been second only to iron in industrial use over the last 50 years. Aluminium is characterized as a light metal, with a density one-third of steel. Further, Aluminium possess qualities like corrosion resistance, formability and recyclability. Recycling aluminium only accounts for 5% of the energy required for producing aluminium in the first place, and 75% of the aluminium ever produced is still in use. [5]

Aluminium alloys are divided into two classes – cast and wrought alloys. Cast alloys are directly cast into their final shape, while wrought alloys are first cast and subsequently deformed by e.g. rolling or extrusion. [6] Both these groups can be divided into heat-treatable and non-heat treatable alloys. The non-heat treatable alloys mainly get their strengthening effect from alloying elements in solid solution, while heat treatable alloys can achieve a significant further strengthening by controlled precipitation, either at room temperature, “natural ageing”, or at an elevated temperature, called “artificial ageing”. The alloys are further divided into series within each class, depending on alloying elements. [7] This study is concerned with a wrought alloy.

2.1.1 Characterization and temper designations

Wrought aluminum alloys are classified in accordance with the international alloy designation system. The alloys are given an AA prefix for Aluminum Association, which are responsible for the designation. [8] An overview of the wrought alloys, with main alloying elements and whether they are heat-treatable or not, is shown in figure 1.

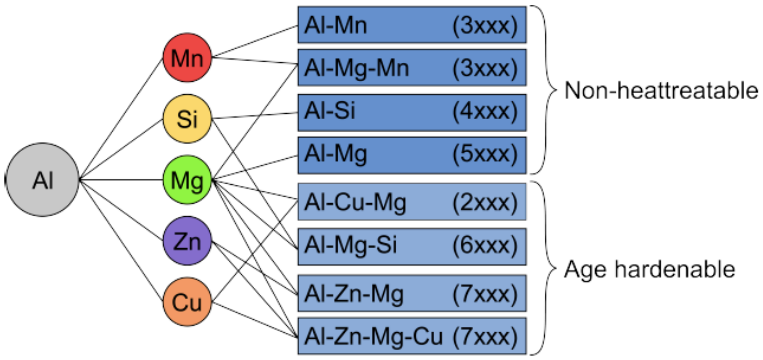

Figure 1: Wrought aluminum alloys associated with their main alloying elements and strengthening categories. Adopted from [9]

The alloys are further classified based on heat treatment procedure, or *tempers*, denoted TX. A list of some important temper states are given in table 1.

Table 1: Table representing the temper states of Aluminium. From [6]

Temper state	Description
T1	Cooled from an elevated temperature-shaping process and naturally aged.
T2	Cold worked after cooling from an elevated temperature shaping process and then naturally aged.
T3	Solution heat treated, cold worked and naturally aged.
T4	Solution heat treated and naturally aged.
T5	Artificially aged after cooling from an elevated temperature shaping process.
T6	Solution heat treated and artificially aged to peak hardness.
T7	Solution heat treated and overaged.

2.1.2 7XXX SERIES

AlZnMg alloys can be used as both castings and wrought products. However, due to poor castability, it is primarily used as wrought products. [10] Al-Zn-Mg alloys are characterized by their high strength and low density, making them widely used within the transportation industry. [10, 11] Together with the 2xxx series[10], they are known as high strength aluminium alloys. The AlZnMg alloys are heat-treatable, meaning that strength is achieved by controlled precipitation during heat treatment. High Zn:Mg ratios has been found to yield the highest strength and best heat treatment response but is in return the most susceptible to stress corrosion cracking. Common aluminum impurities like Fe and Si are often present, but their effect is limited. Cr, Mn and Zr has a slight strengthening effect, but is primarily added to increase the SSC resistance.[10] Zr also participates in the formation of dispersoids, and therefore increases the recrystallization resistance of the material. [12] Typical mechanical properties for 7xxx alloys are given in table 2.

Table 2: Typical mechanical properties of 7xxx alloys. [13]

	$R_{p0.2}$ [MPa]	R_m [MPa]	Elongation [%]
Al-Zn-Mg (7xxx)	225-625	340-675	7-18

2.1.3 PROCESSING ROUTE FOR EXTRUDED PRODUCTS

A cheap and efficient way of producing aluminium alloys of complex shapes is by extrusion. Of the production volume worldwide, one third comes in the form of extruded products.[14]

The processing steps before and after extrusion are presented in figure 2. First, the molten aluminium is heat treated to remove or prevent impurities from forming. Secondly, the aluminium is cast into billets and then homogenized. After casting the billets have a low workability [15], and by homogenization the effects causing this low workability is reduced. The final step prior to extrusion is pre-heating of the billet, in order to reduce the deformation resistance of the alloy.

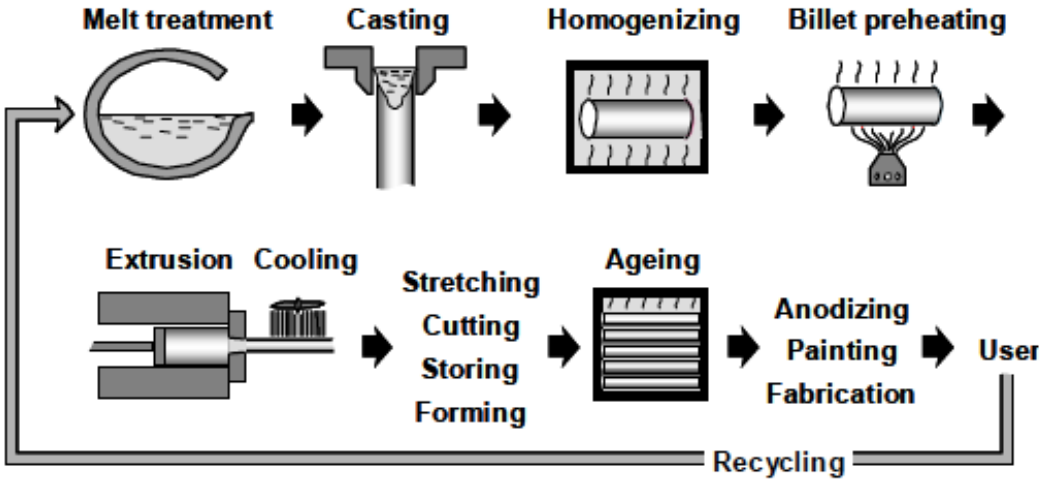

Figure 2: Common processing steps before and after extrusion. From[14]

During extrusion, the billet is forced through a die by a ram, reducing the cross-sectional area of the extrudate and altering its shape. Due to the large deformations involved in the extrusion process, the grains will attain a preferred orientation, called texture, which can have a significant effect on the mechanical properties of the extrudate dependent on direction. This is further described in section 2.8.

2.1.4 Strengthening mechanisms of 7xxx alloys

Aluminium in its pure state has a low strength. By alloying and mechanical/thermal processing, a much higher strength is achievable. In aluminium, there are three major strengthening mechanisms: work hardening, solid solution hardening and age hardening.

When plastically deforming a metal, lattice defects like dislocations are set in motion. By dislocation interaction, new dislocations are formed. The increased density of dislocations will result in dislocation networks, hindering the dislocation movement. To continue the plastic deformation, a larger applied load is required, a process known as work hardening.

Solid solution hardening refers to the strengthening effect by foreign atoms in the crystal lattice. These foreign atoms, either smaller or larger than the solvent atoms, create stress fields in the lattice, which impedes dislocation movement.

The final and most important strengthening mechanism is age hardening, also known as precipitation hardening. This is a heat-treatment procedure and consequently only possible for the heat-treatable aluminium alloys. Age hardening is divided into several steps. The first step, solution heat treatment, involves heating above the solvus line, where all particles are dissolved and goes into solid solution with Al. The alloy is then rapidly cooled to the two-phase region, where a supersaturated solid solution (SSSS) will form.

The next step involves precipitation of finely dispersed precipitates that impedes dislocation movement. By heating the material to an intermediate temperature, the precipitation kinetics are increased due to faster diffusion. [7] This is called artificial ageing, whilst it is known as natural ageing if it takes place at room temperature.

The strengthening effect of the precipitates depends on their distribution and coherency. There are two distinct ways the precipitated particles can impede dislocation movement; they can either be cut by dislocations or they can force the dislocations to bypass them. [4] Small

precipitates are coherent and deformable, and can be cut. Larger precipitates are incoherent and non-deformable, and the dislocations will bypass them.

The generally accepted precipitation sequence in AlZnMg-alloys can be divided into:

$$SSSS(\alpha) \rightarrow GP\ zones \rightarrow \eta' \rightarrow \eta\ (\mathrm{MgZn_2})$$

where the precipitates of each stage is characterized by different chemical compositions and structure. The GP-zones are coherent spheres of Mg and Zn. They have a large strengthening effect due to their bonds and coherency, which halts dislocation movement. [7] The main hardening precipitate η' is a metastable hexagonal phase, semi-coherent with the Al-matrix. [16] The equilibrium phase, η, is hexagonal and incoherent.

2.2 Corrosion of Aluminium

Aluminium owes its corrosion properties to the stable oxide film covering its surface, protecting the underlying metal against corrosion attacks. If broken, the oxide film re-forms immediately in most atmospheres. [17] The formation of the oxide film is given by the following equation:

$4\ Al + 3\ O_2 \rightarrow 2\ Al_2O_3$ (1)

The conditions for stability of the oxide film can be illustrated by the Pourbaix diagram for Aluminium, figure 3. As can be seen by the diagram, Aluminium is protected by its oxide film (passivation) in the pH region of approximately 4-8.5. [17] This range will however also depend on factors such as temperature and alloying content. For pH levels below and beyond the passive range, aluminium corrodes in aqueous solutions as its oxide is soluble in several acids and bases.

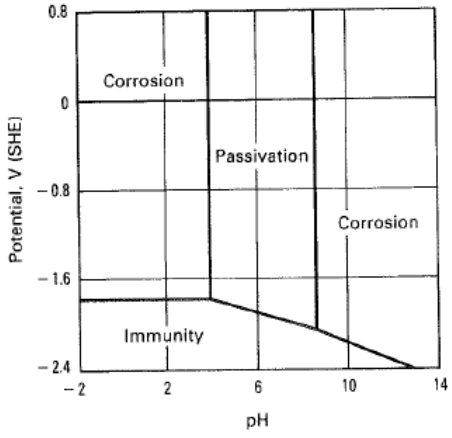

Figure 3: Pourbaix diagram for Aluminium. From [6].

Compared to the other aluminum series, only the 2xxx series are less corrosion resistant than the 7xxx series. The corrosion resistance can, however, be increased by careful alloying.

AlZnMg alloys often contain significant amounts of Cu due to its strengthening effect, as well as making the precipitates stable at higher temperatures. [7] The side effect of Cu is a reduced general corrosion resistance, although the SCC resistance actually increases.[17] Therefore, Cu-free AlZnMg alloys has achieved increasing recognition in recent years. They combine good corrosion resistance, approaching that of 3xxx, 5xxx and 6xxx, with moderate-to-high strength and good toughness. [17]

2.2.1 Pitting corrosion

Through breakdown of the passivating oxide film, aluminium can corrode by pitting. This localized corrosion form appears as pits on the metal surface with varying width and depth, dependent on alloy and quality of the oxide film. [17] For pitting to occur, the critical pitting potential (E_C) must be exceeded (although only locally), in the presence of aggressive anions such as chlorides. The critical pitting potential is a material property and will vary with pH, chloride content and temperature. [18]

The exact mechanism of pit initiation is not well understood[18], although typical initiation sites are well established. Examples of this are inclusions, intermetallic particles, flaws and dislocations. [19] For Al alloys, the pit formation is typically associated with intermetallic particles. These particles are commonly found in the material after casting. By homogenization, some of the intermetallic particles can be dissolved. Non-soluble intermetallic particles are commonly Fe-containing[20], due to the negligible solubility of Fe in the Al matrix. The intermetallic particles have a different electrochemical potential relative to the surrounding matrix, and this potential difference can cause pitting of the surrounding matrix around intermetallic particles acting as cathodes. [21]

In the literature review conducted in this work, not much was found on the chemical composition of intermetallic particles in AA7046. However, more information was found on other 7xxx alloys. For AA7075, the presence of $Al_{23}CuFe_4$, Al_7Cu_2Fe, Al_2CuMg and Fe_3SiAl_{12}

have been suggested[20, 22, 23]. For AA7108, the presence of Al_3Fe and AlFeSi have been reported. [24]

It is widely recognized that pitting corrosion is random by nature, where both pit initiation and pit growth are stochastic variables. Consequently, stochastic models are better suited to describe pitting corrosion than kinetic and thermodynamic treatments of the corrosion reactions. [23, 25]

2.2.2 Intergranular Corrosion (IGC)

Intergranular corrosion is a localized corrosion form where material along the grain boundaries are attacked. Like pitting, intergranular corrosion attacks may have a severe effect on the mechanical integrity of the material. [17] IGC is caused by coupling between zones with a difference in electrochemical potential, creating micro galvanic cells. During the ageing treatment, alloying elements diffuse to the grain boundaries and precipitate, as the grain boundaries are more suitable diffusion paths. [26] Adjacent to the grain boundaries, there will be a zone depleted of alloying elements and precipitates, known as a precipitate free zone (PFZ). The difference in composition between PFZ, grain boundaries and matrix lead to a difference in electrochemical potential. [27] If a corrosive environment is present and the difference in electrochemical potential exceeds 100mV, micro galvanic effects between the PFZ and the surroundings arise. [28] Typical initiation sites for IGC is corrosion pits.

2.3 TENSILE TESTING

To determine the mechanical properties of a metal, uni-axial tensile testing is commonly used. During tensile testing, a specimen is subject to a controlled tension until failure. Due to work hardening, the stress required to continue plastic deformation will increase with increasing plastic strain. In figure 4, the engineering stress-strain curve is plotted together with the true stress-strain curve.

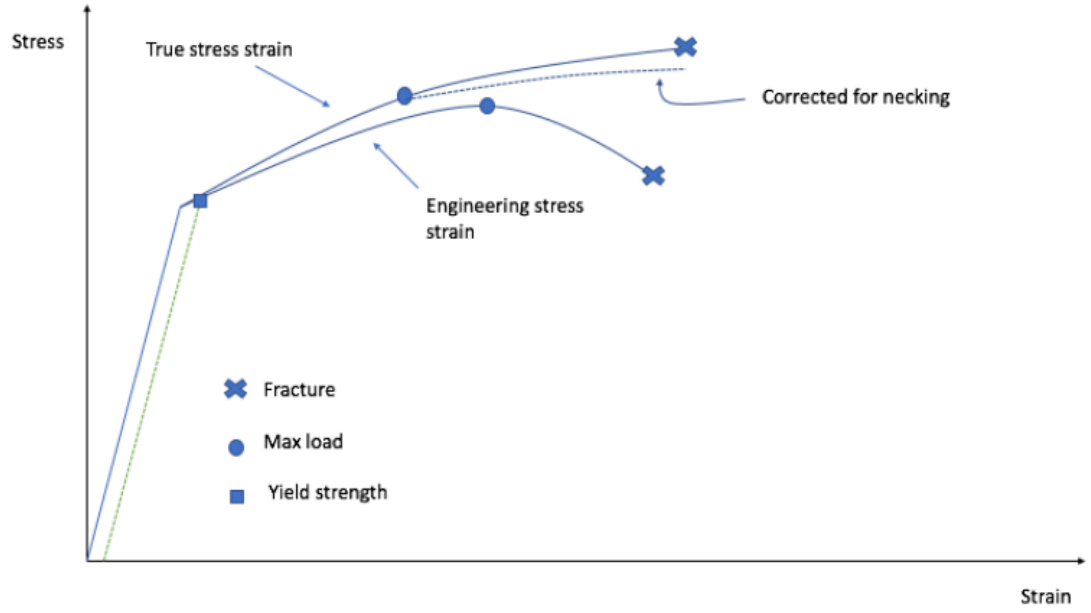

Figure 4: Stress-strain curve, illustrating the difference between engineering and true stress-strain. Reproduced from [4].

In this context, it is important to make a distinction between the engineering stress-strain relationship and the true stress-strain relationship. The engineering stress can be calculated as the applied force (P) divided by the original cross sectional area (A_0) [29]:

$$S = \frac{P}{A_0} \quad (2)$$

As the cross-sectional area decreases during tensile testing, a more precise description is given by the true-stress strain relationship, where the instantaneous cross-sectional area is taken into account. This expression can also be related to the engineering stress and strain, as shown below.

$$\sigma = \frac{P}{A} = s(1 + e) \quad (3)$$

Similarly, true strain can be calculated and related to the engineering strain through the following relation

$$\epsilon = \ln\left(\frac{A_0}{A}\right) = \ln(1 + e) \quad (4)$$

where A is the instantaneous cross-sectional area and A_0 is the original area.
The relationship between the engineering stress and strain and the true stress and strain is only valid up to necking, as it assumes both volume constancy and homogenous distribution of strain. [4]

From figure 4, the differences between the engineering stress-strain curve and the true stress-strain curve is evident. In the elastic region there is no difference, but as plastic deformation proceeds, and the cross-sectional area is reduced, the differences in stress required for continued deformation become more and more pronounced. Beyond necking, a triaxial stress state appears in the necked region, resulting in a larger predicted stress than for uniaxial tension. The dotted line shows a correction for this behaviour. [4]

For materials with is no well-defined transition between the elastic and plastic region, the yield strength is regarded as the stress required to produce a small, specified amount of plastic deformation. The usual definition is the *offset yield strength*, which is found by constructing a line parallel to the elastic part of the stress strain curve, at a specified strain. This is shown as the green line in figure 4. A common strain offset is 0.002, and the expression for the yield strength becomes,

$$\sigma_y = \frac{P_{0.002}}{A_0} \quad (5)$$

2.4 FATIGUE

Fatigue is regarded as failure of a material subjected to cyclic stresses. There are three basic conditions necessary to cause fatigue failure: a sufficient amount of cycles of the applied stress, a high enough fluctuation in the applied stress and a sufficing maximum tensile stress. [4] Almost all fatigue failures initiate at the surface, and the surface state is therefore of high importance. The important surface features can be divided into surface roughness, surface microstructure and residual stresses. These parameters will generally be different for the actual component and the specimens used to construct a fatigue life curve, which is accounted for by using reduction factors. Fatigue is described as a three-step process; consisting of crack nucleation, crack propagation and overload failure. A more detailed explanation of the various stages is given in section 2.7.3.

To understand why fatigue failure occur, it is necessary to describe it from a microscopic level. Figure 5 shows a group of grains orientated randomly to each other, with the lines within each grain indicating the slip planes. Grain A is the only grain with its slip planes aligned parallel to the direction of maximum shear stress, labelled as $\tau_{max,}$ and will slip at a certain level of shear stress. The other grains with its slip planes oriented differently will only experience elastic deformations.

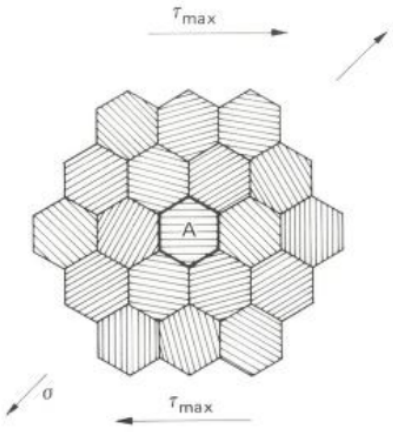

Figure 5: Collection of grains with differently oriented slip planes. A is the only grain with its slip planes aligned parallel to maximum shear stress. From [30].

The scenario can be illustrated by a σ – ε diagram, figure 6. The collection of grains are stressed elastically to σ_1, which results in an elastic strain ε_1. Grain A, with a yield strength of σ_2, therefore experiences a combination of elastic and plastic strains equal to ε_1. When the stress is reversed, figure 6 (b), the outcome is identical with grain A experiencing both elastic and plastic strains. For every stress cycle, the distortion caused by plastic deformation of grain A will lead to a small disorder in nearby grains leading to separation of atomic planes. This will eventually lead to stress concentrations building up, making slip in neighbouring grains with a less suitable orientation possible. [30]

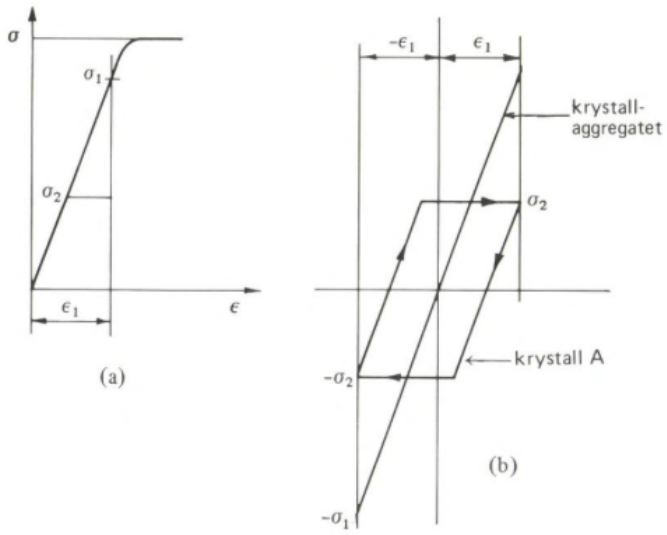

Figure 6: (a) Illustration of yield strength for grain A, σ_2, and applied stress on collection of grains σ_1. (b) if the applied stress is changed to $-\sigma_1$, the collection of grains experience an elastic strain from ε_1 to $-\varepsilon_1$. Grain A experiences the same strain, but it is both elastic and plastic. From [30].

It is important to separate high- and low cycle fatigue. High cycle fatigue is characterized by an applied stress below the yield stress of the material, where the initial deformations are elastic, while low cycle fatigue is characterized by a stress above the yield strength of the material, resulting in plastic deformation of the material and rapid crack growth. [31]

2.4.1 Corrosion fatigue

Corrosion fatigue refers to the combined effect of cyclic stresses and an embrittling medium. The embrittling medium can be solid, gas and liquid, with the latter being the most common adaption. [32] Under cyclic loading, the embrittling medium will interact with the imposed stress and cause a reduction in fatigue life compared to air. Due to the time dependent nature of corrosion, the frequency of testing is of importance. Specimens tested at a smaller frequency will be exposed to the corrosive environment for longer periods of time than a specimen tested at a higher frequency, which in turn will give the corrosive environment more time to influence the metal.

Several models have been proposed in order to explain the reduced lifetime in a corrosive environment. The influence of a corrosive environment is a complex interplay of chemical, mechanical and metallurgical factors. [33] Crack initiation is primarily a surface phenomenon and the interaction between the solution and the metal surface is therefore of high importance. The most commonly reported mechanism for crack initiation in an aqueous solution is[33]:

- Formation of corrosion pits and consequent stress concentrations at the pit base
- Preferential electrochemical attack at the surface where the oxide film is ruptured
- Hydrogen embrittlement

All the above-mentioned mechanisms involve interaction between chemical, mechanical and metallurgical factors. Some of the mechanisms are mainly governed by mechanical and metallurgical factors, while others are mainly influenced by chemical aspects. Due to the wide range of contributing factors, the literature suggests that the initiation stage in corrosion fatigue is extremely complex. [33] Therefore, discussions on corrosion fatigue should be based on a specific alloy/environmental system. Based on the available literature, the three mentioned mechanisms will be discussed in more detail.

Crack initiation at corrosion pits

The most widely reported initiation mechanism for corrosion fatigue in aluminium is the initiation at corrosion pits, as the corrosion pits induces a stress concentration leading to crack initiation [22, 34, 35] As corrosion pits are easily identifiable by microscopy it is tempting to suggest this as the crack initiation mechanism in corrosion fatigue. However, corrosion fatigue has also been observed for samples were pitting were not observed.[36] A more detailed explanation of the pitting phenomena is given in section 2.2.1.

In most of the available literature on corrosion fatigue, corrosion pits are considered the main localized corrosion site responsible for crack initiation. This is based on a mechanical approach, where one considers the stress concentration at the pit base detrimental for fatigue life. Work by Zuo-Yan Ye et. al [35] on a 7A85 aluminum alloy suggests that the microstructure plays a crucial role in determining the corrosion fatigue mechanism. For alloys with coarse precipitated particles, pitting corrosion is favoured, while fine and homogenously distributed precipitated particles is not very sensitive to pitting corrosion. Instead, the homogenously distributed particles lead to intergranular corrosion (IGC) susceptibility.

Rupture of oxide film

Another popular theory, for metals with an oxide film, is the rupture of the otherwise protective film on the metal surface. This model is an extension of the models proposed for anodic SCC under static loading. [37] When intact, the oxide film shields potential corrosion sites from the environment and prevents corrosion attacks. When the oxide film ruptures under continuous stresses, bare metal is exposed to the corrosive environment, acting as an anodic reaction site. Plastic deformation results in the exposure of very active slip planes, as illustrated by figure 7 (B). [38] The next step is dependent on the time of repassivation. If the time of repassivation is fast, one often avoids attacks. If the time of repassivation is slow, we get localized corrosion attacks as illustrated by 7 (C).

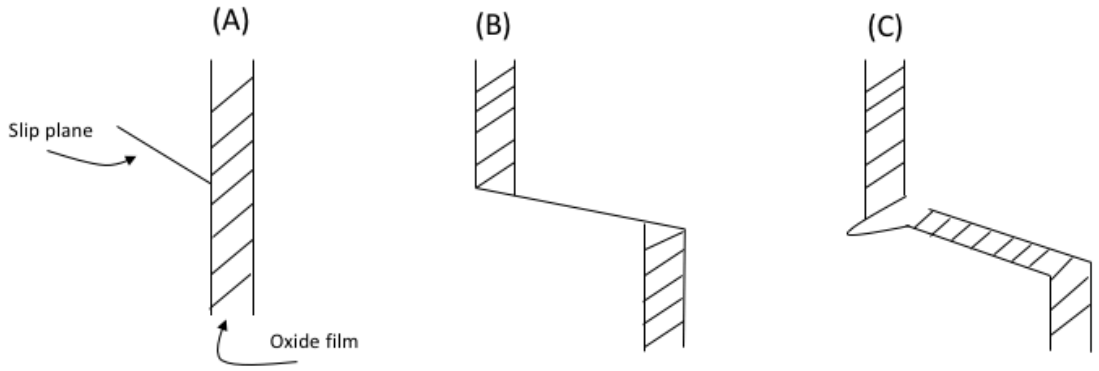

Figure 7: Mechanism of oxide film rupture. Made by the author, inspired by[38].

The pH of the solution will also be of importance. This was observed by Parkins [39], who examined the effects of pH on crack initiation for an aluminum alloy exposed to a sodium chloride solution. At low pH, the solubility of the oxide film is high, and film formation is therefore difficult. In neutral solutions, the oxide film is relatively insoluble until it is disrupted mechanically, exposing the underlying metal to the solution and subsequently causing crack initiation. At high pH, the solubility of the oxide film is again increased.

Hydrogen embrittlement

Hydrogen embrittlement is an important mechanism for environmental cracking under monotonic loading in several alloy/environmental systems, and this mechanism has also been observed for cyclic loading in the same systems. [37] Stoltz and Pelloux [40] proposed that adsorption of hydrogen caused crack initiation at local brittle areas, which was further documented by experimental studies on AlZnMg-alloys. Most of the published literature on corrosion fatigue has focused on crack propagation rather than crack initiation. It is generally accepted that a corrosive environment results in an increased fatigue crack growth (FCG) rate compared to samples tested in air or vacuum, and hydrogen embrittlement have been proposed as the cause. [34, 41] Hydrogen is formed by the reaction of water vapour and the freshly formed fracture surface. [38] In the next step, hydrogen diffuses to the region just ahead of the crack tip (often labelled the fatigue process zone, FPZ) and causes embrittlement by interacting with local stresses and dislocation structures. [41]

A clear difference is observed in the time needed for crack initiation for samples tested in "regular" fatigue and corrosion fatigue. In «regular» fatigue of smooth samples, the initiation stage consists of approximately 90% of its lifetime. For corrosion fatigue (CF) on the other hand, the percentage of fatigue life required for crack initiation may be as low as 10% [33]

As the environmental attacks are influenced by both the electrochemistry of the solution and the loading conditions, it is not possible to make unambiguous conclusions on the mechanisms of corrosion fatigue. [32] There are, however, some general guidelines on the effect of various factors. In neutral pH solutions, dissolved oxygen is essential to corrosion fatigue. By deaeration the fatigue life can be enhanced. Grain boundary precipitates also influences the corrosion fatigue behavior of aluminum alloys by three mechanisms[32]: (i) Influence the rate of electrochemical reactions by aiding in the removal of material from the crack tip and by affecting the rate of hydrogen evolution (ii) Influence the stability of the passivating layer at the crack tip (iii) The shape, distribution and size of grain boundary

precipitates can alter the fracture stress at the crack tip. This can again influence the interaction between the aqueous solution and the crack tip.

2.4.2 THE SN-CURVE

A traditional way of presenting fatigue data is through SN-curves, which is a plot of stress against number of cycles to failure. Normally, the stress levels plotted are nominal stresses, i.e. stress concentrations are not taken into account. [4] During high cycle fatigue testing, the test is usually performed under stress control, as the stress is low enough to limit the strain to elastic levels. [31]

Most nonferrous metals, like Aluminium, does normally not have a well-defined endurance limit. The endurance limit identifies a stress level below where the specimen theoretically will withstand an infinite life. For metals without an endurance limit, the SN-curve will slope gradually downwards with decreasing stresses, as illustrated in figure 8. For such metals, the endurance limit is often defined as the stress level required to reach a high number of cycles. (for example 10^6-10^7 cycles) [42]

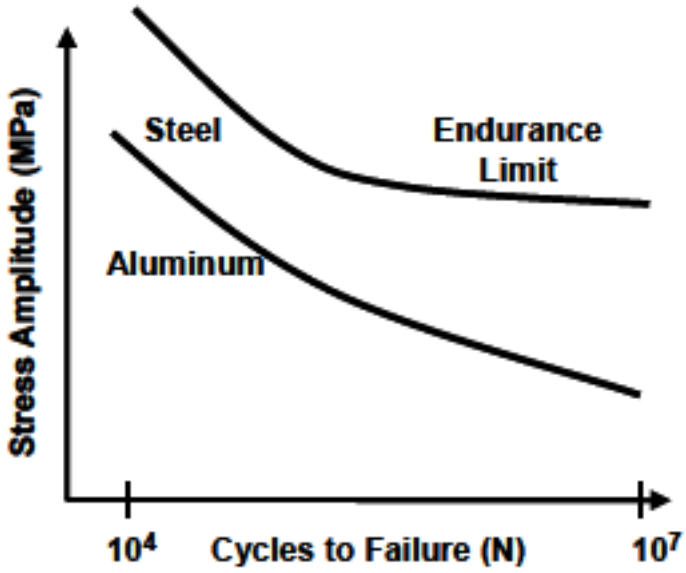

Figure 8: SN-curve illustrating the lack of endurance limit for Al. [31]

In figure 8, number of cycles is plotted against the stress amplitude (σ_a). This is not always the case, and σ_{max} or σ_{min} are also commonly plotted. The mathematical expression for these as well as the stress- and amplitude ratio is given below. A visualization of some of the parameters is given in figure 9.

Stress range: $\sigma_r = \sigma_{max} - \sigma_{min}$ (6)

Mean stress: $\sigma_m = \frac{\sigma_{max} + \sigma_{min}}{2}$ (7)

Stress amplitude: $\sigma_a = \frac{\sigma_r}{2}$ (8)

Stress ratio: $R = \frac{\sigma_{min}}{\sigma_{max}}$ (9)

Amplitude ratio: $A = \frac{\sigma_a}{\sigma_m}$ (10)

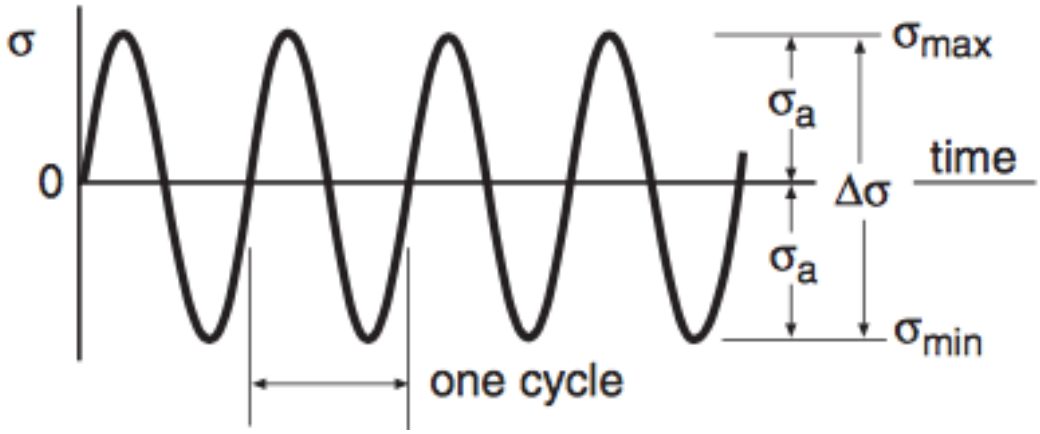

Figure 9: Cyclic loading and visualization of important fatigue parameters. [31]

There are several possibilities on how the stress is applied. To distinguish the different methods from each other, we refer to the R value. A common way of testing is *fully reversed cycling*, i.e. $\sigma_{max} = |\sigma_{min}|$ and R=-1. The SN-curve may be influenced by several factors such as testing frequency (for metals only at frequencies above 200 Hz typically[43]), mean stress and stress amplitude. To relate fatigue results obtained at different mean stresses, various empirical models exist. One of them is the Goodman relation, which will be further described in section 2.4.4. A common way of presenting corrosion fatigue results is to compare the lifetime in the corrosive environment with the lifetime in air, by SN curves. An

example of this is given in figure 10, where the dashed line represent dry air while the solid line represent the corrosive environment.

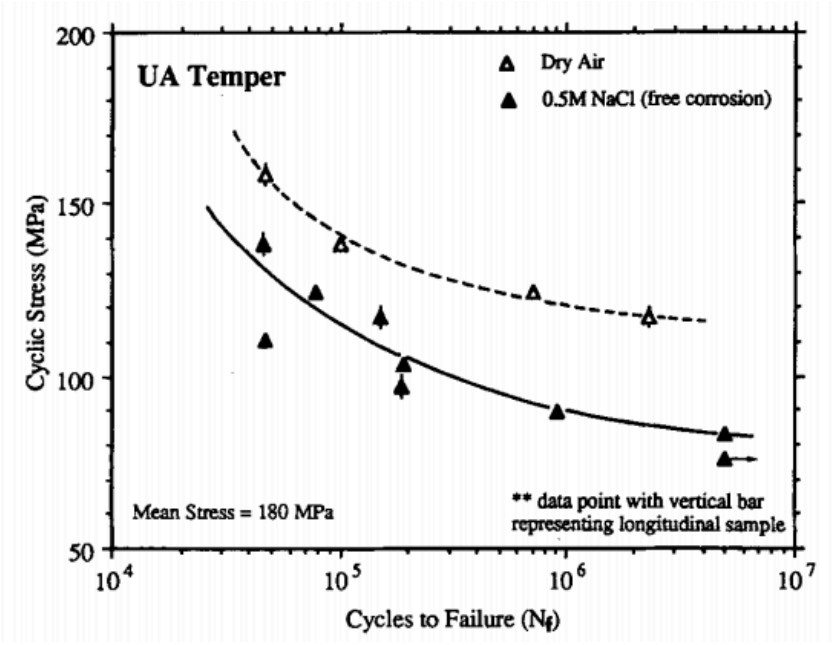

Figure 10: Comparison of lifetime in air and in a corrosive environment. From [44].

2.4.4 Goodman Diagram

The Goodman diagram illustrates how a change in mean stress (σ_m) influence the stress range (σ_r). [4] To construct a Goodman Diagram, the ultimate tensile strength (σ_{UTS}) and yield strength (σ_{YS}) is marked on the two axes. A straight line is then drawn from each of the marked points until they cross, marked 1 in figure 11. Then, straight lines (marked 2 and 3 in the figure) are drawn from this point to σ_{max} and σ_{min} for a given mean stress (marked $\sigma_{m\ ex}$ in the figure). These lines can be extended until they cross the y-axis, illustrating the stress range corresponding to a mean stress (σ_m) of 0, i.e. R = -1. The Goodman relation is known to be conservative, i.e. the experimental results tend to be better than the prediction by the Goodman relation. [42]

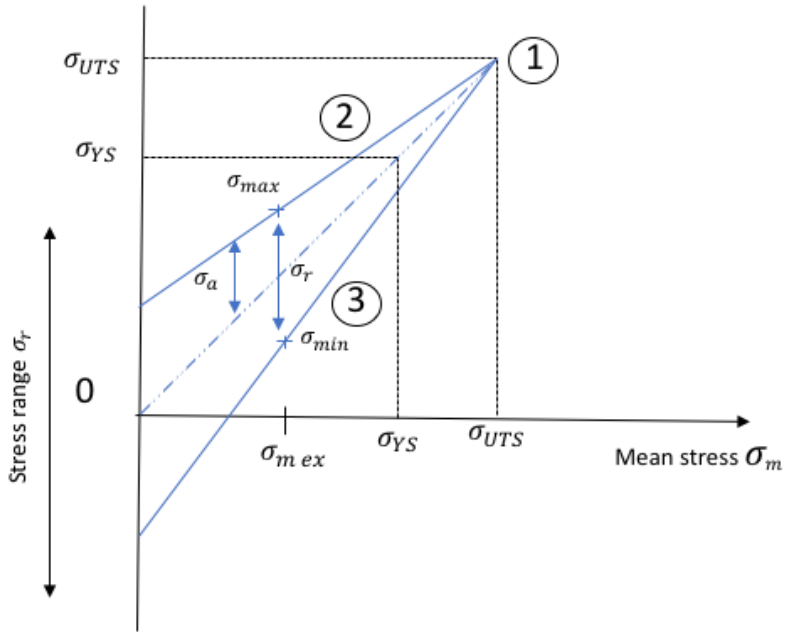

Figure 11: Construction of Goodman diagram. Made by the author, inspired by [4]

2.5 Surface condition

As practically all fatigue failures initiate at the surface, the surface condition is of high importance when discussing fatigue. The surface condition can be divided into three-sub sections: surface roughness, residual stresses and surface microstructure. In this section these features will be described in more detail.

2.5.1 Surface roughness

Since the first studies on fatigue failure it has been recognized that different surface finishes yield different fatigue performance, with the smooth surface having the longest fatigue life. The orientation of eventual scratches on the specimen surface also plays a role. Scratches oriented perpendicular to the tensile direction shows the worst properties, and scratches oriented parallel to the tensile direction the best. [4]

During extrusion it is unavoidable to introduce so-called die lines, which is seen as narrow lines in the extrusion direction. If these die lines are oriented perpendicular to the testing direction, they may act as stress concentrators, lowering the fatigue life of the specimen. [45]

The main cause of these lines is the build-up of material in the area between the die and the mandrel. When this metal work hardens and oxidizes, it can score the surface of the extruded material. [31]

To measure the surface roughness, both mechanical and optical methods are available. Optical methods has the advantage of being able to scan large areas relatively fast without damaging the surface. [46] Roughness values can either be calculated for a line (profile) or for a surface (area), with profile roughness most commonly used. The most common parameters in relation to fatigue is R_a, R_t and R_z [31]. R_a is the average roughness of the profile, R_z is the mean peak valley height; the average of the five largest peaks to valley height, while R_t is the maximum peak to valley height, i.e. the difference between the highest and lowest point in the scan. Which of these parameters that are most closely related to fatigue life is however debatable. [47, 48]

One of the issues regarding the traditional roughness parameters is that they are not well suited to describe surface appearances that are known to affect fatigue life, like valley spacing and valley tip radius. [49] An illustration of three different surfaces yielding the same roughness parameters is presented in figure 12.

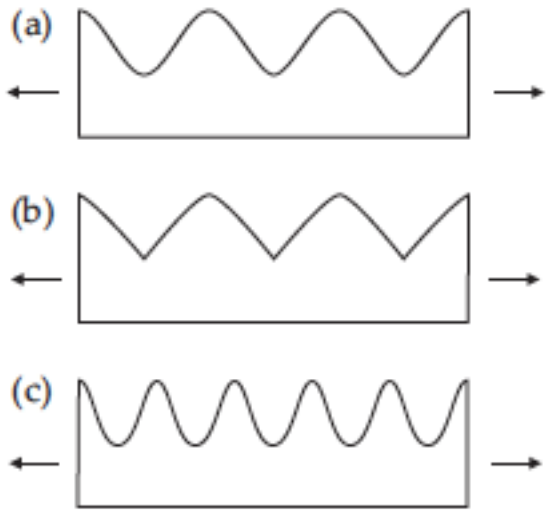

Figure 12: Three surfaces with the same Ra, Rt and Rz values but different fatigue properties. From [49]

The geometries in figure 12 are clearly different. The valley tip radius for geometry (b) is smaller than the valley tip radius for geometry (a) and (c), while the valley spacing is smaller for geometry (c) than (a) and (b). The stress concentrations leading to crack initiation and subsequently fatigue failure will therefore be different in these three cases[49], even though the R_a, R_t and R_z parameters display the same surface roughness.

2.5.2 Residual stresses

Residual stresses can be defined as "locked-in" stresses that are present in a part after fabrication or heat treatments. [4, 32] Residual stresses can be separated into tensile and compressive residual stresses, where the tensile residual stresses are detrimental to fatigue life and compressive residual stresses are beneficial. [4] A common way of introducing compressive surface residual stresses is by shot peening. Here, fatigue crack initiation has been observed in the subsurface, overriding effects of the surface roughness. [49, 50]

2.5.3 Surface microstructure

It is well documented that fatigue crack initiation is easier in coarse grained specimens compared to fine grained specimens. [51, 52] Consequently, time prior to crack initiation will be longer for fine grained specimens than for coarse grained specimens. A proposed theory for this is a locally higher cyclic stress to yield strength ratio for the coarse surface grains than the fibrous microstructure, which favours crack initiation in the coarse grain layer. Another proposed theory is the presence of precipitate free zones (PFZ) in age-hardenable aluminium alloys, which has a lower strength than the grain interior. During fatigue testing plastic strains may therefore be concentrated at the PFZ, leading to stress concentrations and crack initiation. This effect is increasingly pronounced at large grain sizes. [51] How the relation applies to corrosion fatigue is however less investigated. Pedersen[51] proposes that small differences in electrochemical potential between recrystallized and fibrous grains may cause galvanic corrosion and subsequent easier crack initiation.

2.6 SEM

Scanning electron microscope (SEM) is commonly used in characterization of materials. The specimen to be investigated is irradiated by an electron beam, giving raise to different detectable signals. Compared to a light microscope, SEM has a much higher resolution and depth of field. A high depth of field is especially important when investigating fracture surfaces, to ensure that the entire fracture surface is in focus at the same time. For texture analysis, SEM is also used with the electron backscatter diffraction (EBSD) technique. A tilted specimen is hit by an electron beam, and diffracted electrons from the specimen will hit a phosphorous screen generating a diffraction pattern. [53] The diffraction pattern is then indexed, followed by software analyses. For quantification of chemical composition, EDS is commonly used. When the electron beam impacts the sample, x-ray radiation is emitted. The x-ray radiation emitted is characteristic for each atomic element, and the elements can therefore be detected.

2.7 Fracture

There are different ways of classifying fracture. Today, the most common way is to divide them into three types: ductile, brittle and fatigue fracture. In this section these fracture types will be presented in more detail.

2.7.1 Ductile fracture

Ductile fracture is defined as fracture occurring after significant plastic deformation. There are different variants of ductile fracture, depending on the loading conditions. The discussions in this section will be concerned with ductile fracture occurring after uniaxial loading. The process of a ductile fracture can be divided into several stages, visualized in figure 13. After necking, small micro voids form in the cross section. With continued straining, these micro voids coalesce into a crack. The crack continues to grow by coalescing until it reaches the outer part of the neck, commonly at an angle of 90° to the applied load. Then, it grows along specific crystallographic planes at an angle of approximately 45° to the tensile axis, where the shear stress is at its maximum. [4] This is called a “cup-and-cone” fracture. On a microscopic scale, a ductile fracture characteristically consists of “dimples”, with each dimple being one half of a microvoid that formed during the fracture process.

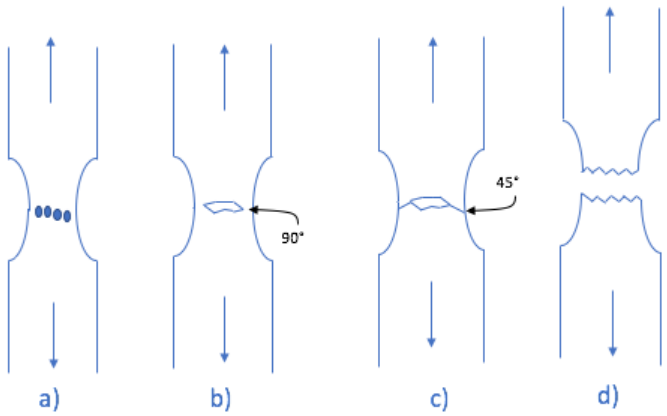

Figure 13: Illustration of a ductile fracture. Made by the author, inspired by[4].

2.7.2 Brittle fracture

Brittle fractures usually take place without significant plastic deformation. Brittle fractures can be both inter- and transgranular. An intergranular fracture is characterized by crack propagation along the grain boundaries, while a transgranular fracture is characterized by crack propagation through the grains. Microscopically, a typical hallmark for an intergranular fracture is facets with a “rock candy” surface appearance[54], while transgranular fractures are often seen to have a grainy or faceted appearance. [29]

2.7.3 Fatigue fracture

As mentioned in section 2.4, fatigue failure occurs when a material is subjected to cyclic stresses. The fluctuating stresses result in strong, local stress concentrations, which may result in crack initiation after some time. Fatigue failure usually initiate at the surface, and typical nucleation sites are surface irregularities such as notches, sharp corners or a metallurgical discontinuity. [29] In addition, the cyclic loading produce surface discontinuities that act as stress concentrators and potential crack initiation sites. Every crack does not necessarily result in fracture, but is rather dependant on the cyclic loading and stress level. [53]

The process of a fatigue failure can be divided into three stages[53]:

Stage 1: Crack initiation and growth along slip-bands
Stage 2: Crack growth on planes of high tensile stress
Stage 3: Ultimate fracture

During the first few thousand cycles of stress, slip lines are formed in grains with a preferred orientation to slip. As the cycling continues, slip bands are formed, which is a collection of

several slip lines. By electropolishing, the majority of the slip bands can be removed. The slip bands which cannot be removed, called persistent slip bands (PSB), has the form of ridges and grooves at the surface(*slip-band extrusions* and *slip-band intrusions),* which act as stress concentrators and initiation sites for cracks. [4, 55]The stage I crack propagates along the PSB´s at an angle of 45° to the applied stress, i.e. parallel to the direction of maximum shear stress. [53] The fracture surface of stage 1 growth is basically featureless. When the crack advances to stage II, a drastic increase in the crack propagation is seen. The rate of crack growth goes from a few nm per cycle to microns per cycle. [4]

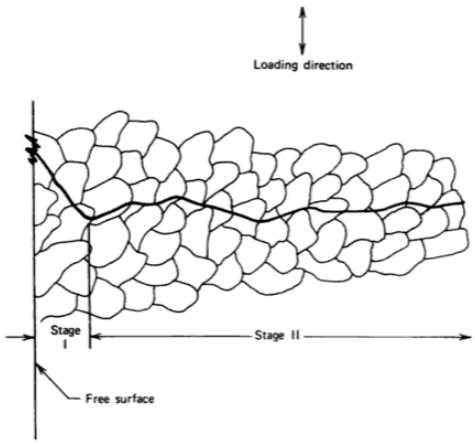

Figure 14: Schematic of stage 1 and stage 2 crack growth. From [55].

Another important difference is the changing growth direction of the crack. The crack goes from growing along specific crystallographic planes to growing approximately perpendicular to the applied stress, as depicted in figure 14. Here, the crack growth is transcrystalline, i.e. the crack grows across grain boundaries. Transcrystalline crack growth is most common, but intercrystalline growth is also possible, depending on material, load and environmental conditions. [55] The fracture surface of stage II growth consists of beach marks and striations, where every striation is produced by a single stress cycle. Beach marks are seen by visual inspection, while striations are visible by electron microscopy. [29] The presence of striations indicate that the fracture is caused by fatigue, but an absence does not rule it out. [4] When the crack has reached a critical size, the cross section of the material is too small to withstand the load, and fracture is inevitable. The region where final fracture occur can have a brittle or ductile characteristic. [29]

2.8 ANISOTROPY AND TEXTURE

When a metal undergoes severe deformation, like extrusion, or recrystallization and grain growth, crystallographic texture is commonly developed. [56] Texture is the trend of grains in a metal to orientate themselves in certain directions, which may give rise to anisotropic properties. Most metals are anisotropic and have a degree of texture. In contrast, a material with completely random texture will be isotropic, meaning that all properties are independent of direction. A consequence of anisotropy can be that the material deforms differently in different directions.

The exact nature of the texture developed in a material is a complex function of the thermal and mechanical treatments the material has gone through, as well as the material itself. Hence, every processing step from casting to any annealing following deformation (e.g extrusion, rolling and wire drawing) will influence the texture of the material.

Deformation textures is the result of mainly two factors, i.e. crystallographic and geometrical constraints(e.g. plane strain or uniaxial tension). The former refers to the type and number of slip systems of the material, which is 12 for aluminium.

To represent texture, pole figures are commonly used. For each grain, a set of crystallographic directions are chosen(for example the <100> directions) and projected onto the equatorial plane, as depicted in figure 15. The group of <100> directions plotted on the equatorial plane is called the (100) pole figure, figure 15 (b). For a polycrystal with texture, the poles will be evenly distributed over the entire pole figure, figure 15 (c). If the material has texture, the poles will be grouped together, as shown in figure 15 (d).

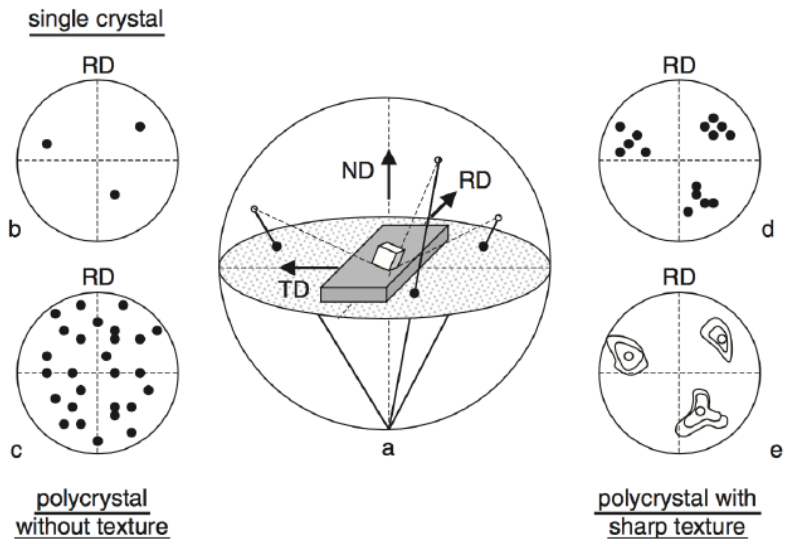

Figure 15: (a) Stereographic projection of the (100) pole figure. (b) (100) pole figure for a single crystal (c) (100) poles with random texture (d) (100) poles for polycrystal with texture (e) Contour plot of the (100) poles for situation described in (d). From [56]

3 Experimental

3.1 Materials

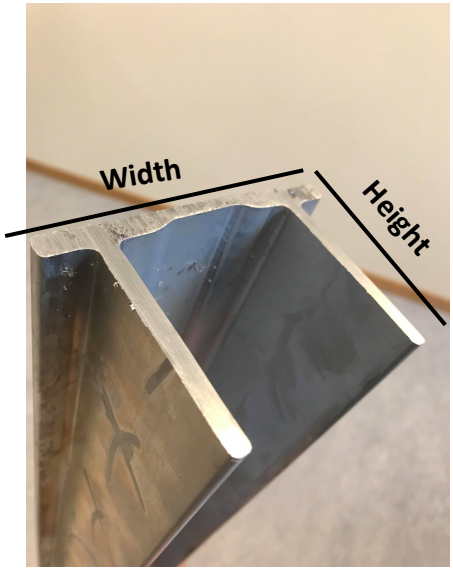

Figure 16: Picture of extruded profile, denoting width and height.

The material used for testing was provided by Benteler Aluminium Systems, Raufoss, in the form of a "U" shaped extruded profile with length 3 m, width 9.5 cm and height 6.5 cm, figure 16. The alloy used is a variant of the Al-Zn-Mg alloy 7046, defined by Benteler, with composition as given in table 3. The composition limits of AA7046 as tabulated by the Aluminium Association is given in table 4. The exit temperature of the extruded profile was ~530 °C, the extrusion speed was 6 m/min and the diameter of the extruded billet was 280 mm. The specimens used for fatigue and tensile- testing were machined at SINTEF Raufoss Manufacturing.

Table 3: Alloying content for variant of 7046 used in this thesis.

	Fe	Si	Cu	Mg	Cr	Mn	Zn	Zr	Ti	Ni	Al
7046	0.24	0.1	0.32	1.2	0.02	0.02	6.5	0.15	0.02	0.002	Remainder

Table 4: Alloying content limits given by the Aluminum Association. [57]

	Fe	Si	Cu	Mg	Cr	Mn	Zn	Zr	Ti	Ni	Al
AA7046	0.4	0.2	0.35	0.8-1.6	0.2	0.3	6.1-7.3	0.1-0.25	0.03	0	Remainder

3.2 HEAT TREATMENT PROCEDURE

Two different temper states were investigated in this work, T6 and T7, i.e. peak aged and overaged condition. The heat treatment procedure for achieving T6 is presented in figure 17, performed at SINTEF Raufoss Manufacturing. The extruded profile was first solution heat treated at 480 °C for 30 minutes followed by quenching in water to room temperature. Then, the extruded profile was stored at room temperature for 10 days before artificial ageing. Within these 10 days fatigue and tensile samples were machined from the extruded profile. Finally, the machined samples were artificially aged in a two-step process: first heated from 25-150°C with a constant heating rate for 6 hours and then held at 150°C for 6 hours.

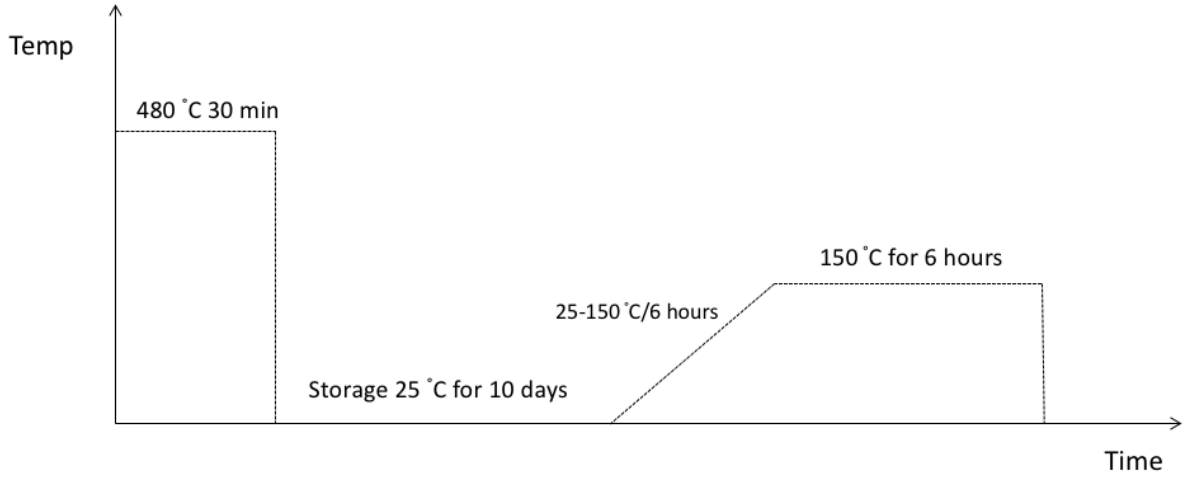

Figure 17: Heat treatment procedure to achieve T6 condition. Made by the author.

To achieve T7 condition the samples were given an additional heat treatment, presented in figure 18. The samples were heated from 30 °C to 90 °C in 25 minutes, and subsequently cooled down from 90 °C to 50 °C in 11 minutes. The temperature in the figure is the logged temperature of the sample. This procedure was performed by Benteler.

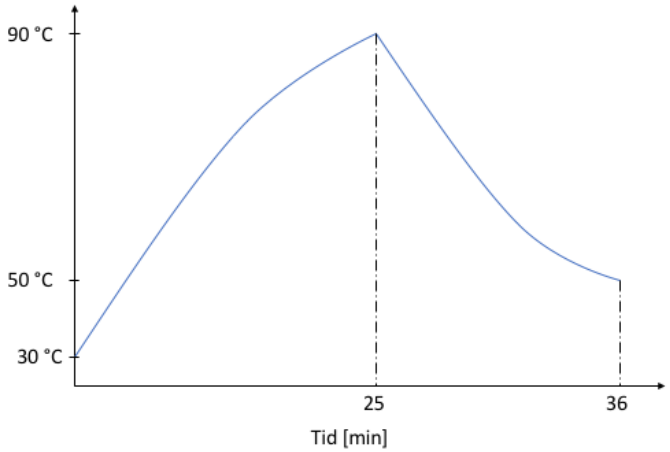

Figure 18: Additional heat treatment to achieve T7 condition. Made by the author.

3.3 LIGHT MICROSCOPY

Imaging in light microscope was conducted to characterize the microstructure of the material. Small pieces of dimensions 20x20 mm were cut out by Struers Labotom-5. Imaging was done on as-delivered material, which had gone through the heat treatment procedures as described in section 3.2. The specimens were cold mounted in Struers Epofix and grinded with increasing fineness to 4000P. When a uniform surface was obtained, the specimens were polished with 9, 3 and 1 µm grain sized diamond spray for 2-5 minutes in Struers Tegrapol 31. Between each polishing step the specimens were cleaned with water, soap and ethanol. The specimens were finally anodized in a 5% HBF_4 solution with an applied voltage of 20V.

A Zeiss Axio Vert A1 microscope was used for imaging, and the ZenCore software for analysis of the images. The images were taken in the ED-ND plane, see figure 19, with polarized light and a sub-parallel λ plate.

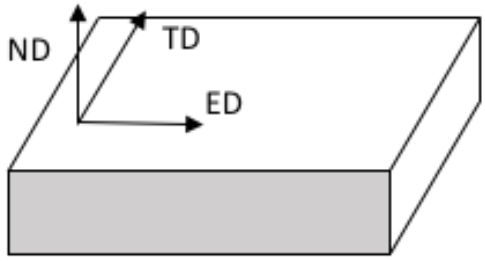

Figure 19: Gray area illustrates view plane for material characterization in light microscope, made by the author.

3.4 Surface roughness measurements

Prior to roughness measurements, all specimens were studied with the bare eye to look for any scratches or irregularities. Highly deviating specimen were taken aside and not tested in fatigue. Subsequently, six specimens were chosen and scanned with AliconaInfiniteFocusSI. The surface roughness was measured for both extruded and machined surfaces.

To operate the instrument, X, Y and Z coordinates are chosen for the surface to be scanned. The instrument then starts scanning the surface, creating a 3D re-creation of the surface specified by the coordinates chosen. A 5x lens was used, which has a vertical resolution of 410nm.

To quantify the surface roughness, line scans were performed. Scans were performed both in the direction of loading (i.e. in the extrusion direction) and in the direction perpendicular to loading. This was done to quantify the magnitude of the die line surface roughness. An illustration of this, where the red areas illustrate scans, is given in figure 20.

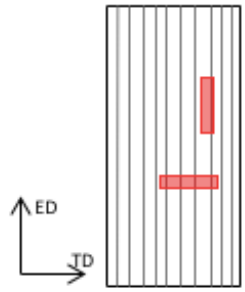

Figure 20: Figure illustrating concept of roughness measurements. Gray lines indicate die lines from the extrusion process. Made by the author.

3.5 TENSILE TESTING

To determine suitable loads for fatigue testing, tensile testing was performed for samples in both T6 and T7 condition. Six tensile specimens were prepared, three from each temper state, in order to increase the reliability of the results. Tensile testing was done using a Walter+Bai LFV 100 kN press with a crosshead speed of 3 $\frac{\text{mm}}{\text{min}}$. A 50 mm clip-on extensometer was used for measuring the engineering strain.

The specimens used was machined into the dimensions given in figure 21 by SINTEF Raufoss Manufacturing.

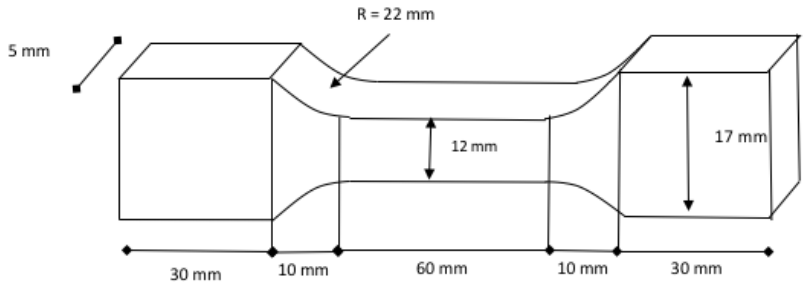

Figure 21: Dimensions of specimens used for tensile testing. Made by the author.

3.6 FATIGUE TESTING

As the testing machine had no built in function to perform fatigue testing on samples submerged in an aqueous solution, chambers made by Lindstad[58] were used. The chambers were designed to safely contain the aqueous solution, as well as being large enough for the entire specimen gauge section to be submerged. Lindstad made three chambers of varying dimensions, and based on his work, it was decided to use two of the three chambers available. The last chamber was not used as it did not allow for the entire specimen gauge section to be submerged in the aqueous solution.

The frequency used during testing was set to 5 Hz and the stress ratio (R) was set to -1, i.e. fully reversed cycling. All samples were tested in the direction parallel to the extrusion direction. The machine used for fatigue testing was MTS810 100kN. The dimensions of the samples used for fatigue testing is given in figure 22. The machining was performed by SINTEF Raufoss Manufacturing. All fatigue tests were performed at room temperature. Extruded and machined surface, respectively, is also marked in the figure.

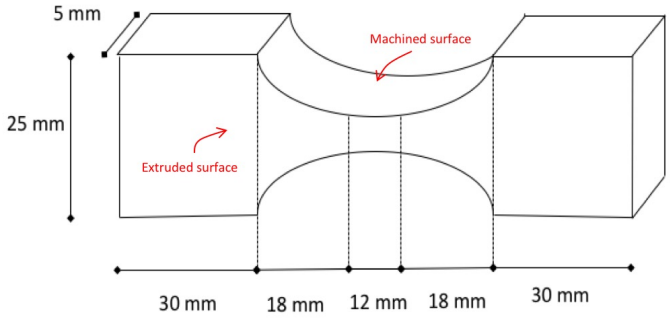

Figure 22: Dimensions of samples used for fatigue testing. Made by the author.

The fatigue testing in the current work consisted mainly of samples submerged in a 5 wt% NaCl solution and samples pre-corroded in the same solution and subsequently fatigue tested in air. The pH of the solution was measured to 6.9 with PHM210 Standard pH Meter.

3.6.1 Chamber design

The setup for corrosion fatigue testing was composed of two parts – a disc made of aluminum and a chamber made of plexiglass. First, the test specimens were cast to the discs using *Pattex Easy Silicone*. When the silicone had solidified, the disc and test specimen were mounted to the chamber using *Pattex Easy Silicone*. Dimensions of disc and chambers is given in figure 23-25, and an illustration of how the samples were mounted to the chamber is given in figure 26. An image showing a sample mounted to the chamber in the fatigue testing machine is given in figure 27. Note that a slightly thinner disc of 3 mm was used for

the smaller chamber. This was done to ensure that the entire specimen test area was submerged during testing.

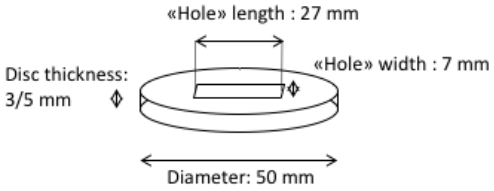

Figure 23: Dimensions of disc used for chamber setup. Made by the author.

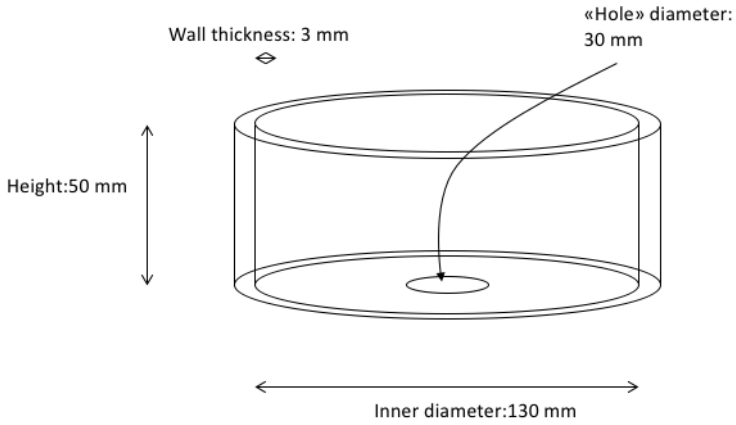

Figure 24: Dimensions of the largest chamber used for corrosion fatigue testing. Made by the author.

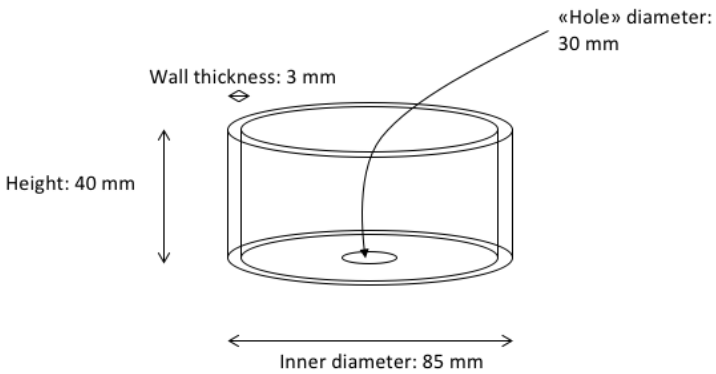

Figure 25: Dimensions of the smallest chamber used for corrosion fatigue testing. Made by the author.

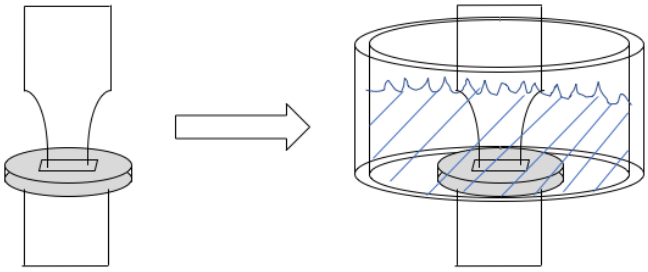

Figure 26: Sample mounted to disc (Left) and sample placed in chamber. (Right) The blue illustrates the salt solution. Made by the author.

Figure 27: Image of sample mounted to chamber in fatigue machine.

3.6.2 Cleansing of samples and chambers

After fatigue testing, the samples were immediately pulled apart by the same machine, rinsed in water and acetone, and sealed in unused plastic bags.

To remove remaining silicone after testing, a small piece of epoxy was used to remove most of it. When only small stains of silicone were remaining, the discs were rubbed with a brush in soap and water. It is important to remove all silicone from the previous trial as the silicone-silicone adhesion is poor. To clean the chambers, a brush was used with soap and water.

3.6.3 Pre-corrosion testing

For a more thorough understanding of how the NaCl solution effects the material, some samples were submerged in the aqueous 5 wt% NaCl solution for various times prior to fatigue testing in air. Following immersion, the samples were rinsed in running tap water for 5 minutes and sealed in unused plastic bags.

3.7 SEM

This section will go through the parts of this thesis work that were conducted in SEM or are related to SEM. The texture (EBSD) and particle (EDS) investigation was carried out in FESEM Zeiss Ultra 55, while the fractographic parts were conducted in FESEM Zeiss Ultra 55 and LVFESEM Zeiss Supra 55.

E

3.7.1 TEXTURE

The material texture was examined to determine the degree of mechanical anisotropy, using EBSD. First, a small pieces of dimensions 20x20 mm were cut out by Struers Labotom-5 and cold mounted in Struers Epofix, before it was grinded with increasing fineness to 4000P. When a uniform surface was obtained, the specimen was polished with 9, 3 and 1 µm grain sized diamond spray for 2-5 minutes in Struers Tegrapol 31. Between each polishing step the specimen was cleaned with water, soap and ethanol. Lastly, the piece was electropolished with Struers Lectropol-5 in an A2 electrolyte at –30 °C for 20s with an applied voltage of 20V. To obtain the EBSD patterns, the FE-SEM Zeiss Ultra 55 was used with the NORDIF EBSD system. The specimen was tilted 70°, the working distance was ~24 mm, the acceleration voltage was 20 kV and the apperture 300µm. The texture data was collected and indexed with the EDAX OIM Data Collection software, and finally analyzed with the EDAX OIM Analysis program. A summary of the settings used for EBSD analysis is given in table 5.

Setting	Texture investigation
Operation Mode	EBSD
Acceleration Voltage	20 kV
Working Distance	~24 mm
Aperture Diameter	300 μm
Tilting angle	70 °

Table 5: SEM settings for texture investigations.

3.7.2 PRIMARY PARTICLE INVESTIGATION

To investigate the primary particle distribution of the alloy, a small sample of dimensions 20x20 mm was cut out by Struers Labotom 5. The sample was subsequently grinded with increasing fineness to 4000P. When a uniform surface was obtained, the specimen was polished with 9, 3 and 1 µm grain sized diamond spray for 2-5 minutes in Struers Tegrapol 31. Between each polishing step the specimen was cleaned with water, soap and ethanol. For chemical analysis of the particles, EDS spectra were obtained and analyzed with the Quantax Espirit software. SEM parameters for the primary particle investigation is given in table 6. The particle distribution in both the extrusion and longitudinal plane was examined, corresponding to the gray-colored parts of figure 28.

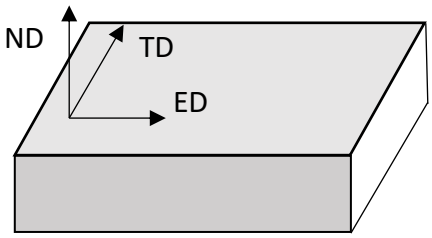

Figure 28: Gray area illustrates view planes for material characterization in light microscope. Made by the author.

Setting	Particle analysis
Operation Mode	SE
Acceleration Voltage	20 kV
Working distance	~14 mm
Aperture Diameter	300 μm
Tilt angle	0 °

Table 6: SEM settings for particle investigation.

To get an indication of particle size and distribution, the image processing software ImageJ was utilized. The images were uploaded to ImageJ and tweaked to give a valid representation of the particle size and distribution. The area of the particles in ImageJ is calculated by counting pixels. For a better representation of the particle size it is common to use the Equivalent Sphere Diameter (ESD), which is the diameter of a sphere of equivalent

volume. [59] The Equivalent Sphere Diameter (ESD) can be calculated by the following equation:

$$ESD = \sqrt{\frac{4A}{\pi}} \quad (11)$$

Where A is the particle area.[60]

3.7.3 Cleaning procedure of corroded samples

To remove corrosion products accumulated during submersion in the 5% NaCl solution, samples were cleaned in 20 $\frac{\mathrm{g}}{\mathrm{L}}$ CrO_3 and 50 $\frac{\mathrm{mL}}{\mathrm{L}}$ H_3PO_4 prior to SEM analysis. The samples were held in the solution for ten minutes at 85-90 °C, according to ASTM G1 – 90. The samples were then rinsed in distilled water and submerged in concentrated HNO_3 for 30 seconds. Finally, the samples were rinsed in distilled water and dried in air.

3.7.4 Evaluation of salt solution

To evaluate the effect of the salt solution, the as-extruded surfaces of the samples were studied. The purpose of this was to investigate the samples for potential corrosion attacks, and how the corrosion attacks changed with increased exposure time. Due to the stochastic nature of pitting corrosion, pit size and depth will vary over the sample surface. A complete characterization of the samples tested in corrosion fatigue would take excessive time or require implementation of advanced statistical models. A small section close to the suspected crack initiation site was therefore chosen for further study, as shown in figure 29. The small axis cross notes the extrusion and transverse direction, respectively.

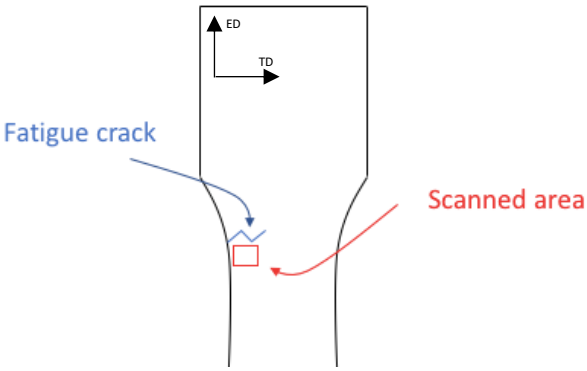

Figure 29: Illustration of where on the samples the corrosion attacks where examined. Made by the author.

3.7.5 FRACTORGRAPHY

For fractorgraphy of fatigue samples, SEM was used. To avoid destroying the fracture surface the machine was stopped when a crack had initiated. All samples were pulled apart immediately after crack initiation using the same machine and flushed with acetone. The samples were cut into suitable sizes to fit into the SEM specimen chamber. The operation mode used was secondary electrons (SE) with an acceleration voltage of 10kV, aperture diameter of 30 μm and a working distance of 10-40 mm. To strengthen the fractographic investigations, samples of the same alloy tested in air were also examined. A summary of the SEM settings is given in table 7.

Table 7: SEM settings for fractography.

Setting	Fractography
Operation mode	SE
Acceleration voltage	10 kV
Working Distance	10-40 mm
Aperture diameter	30 μm
Tilting angle	0 °

4 Results

4.1 Light microscopy

The light optical micrographs of the 7046 in the T6 and T7 temper state is presented in figure 30. The presence of dispersoids pinning the grain boundaries preserves the fibrous microstructure in the core of the microstructure. At the surface, where the strain accumulation is large, a recrystallized layer of approximately ~20 μm can be seen in figure 31. The fibrous microstructure is most prominent in the center of the sample, where we clearly see how the grains are elongated in the extrusion direction. Closer to the surface the fibrous grains are thinner and less visible from the micrograph. The additional heat treatment to achieve T7 condition (peak temperature of 90 °C) is not high enough for additional grain growth. The axes are valid for both figures.

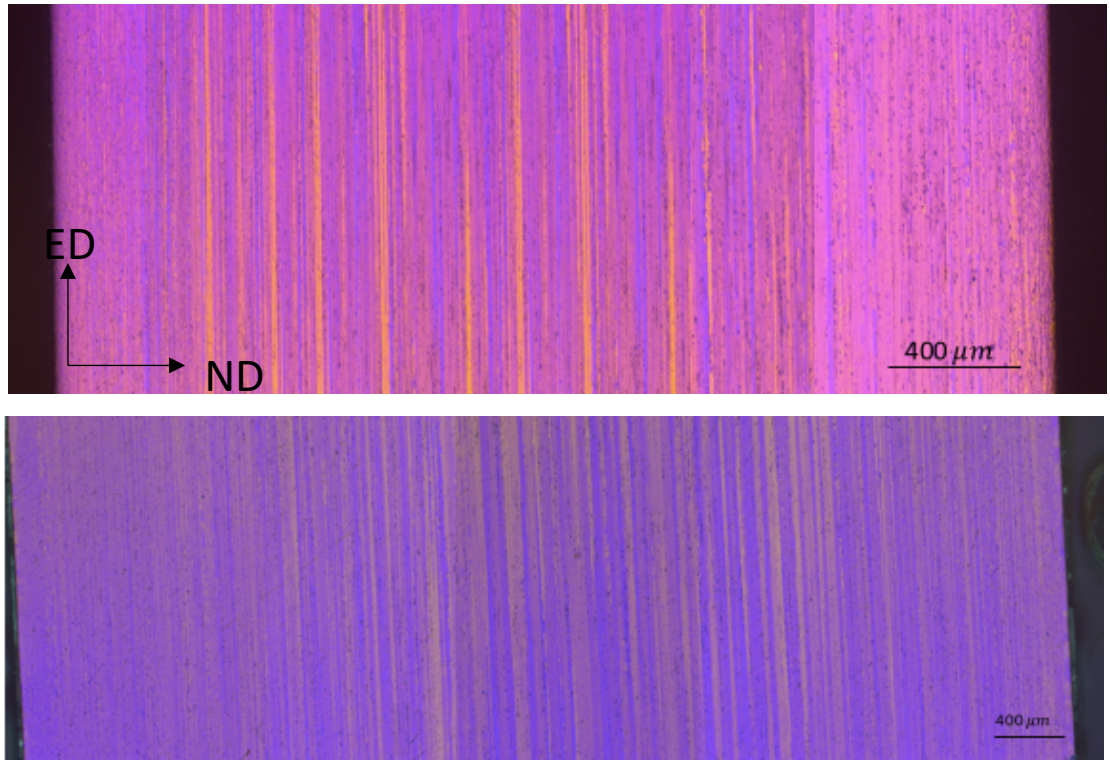

Figure 30: Microstructure of T6 samples (top) and T7 samples (bottom). 5x magnification.

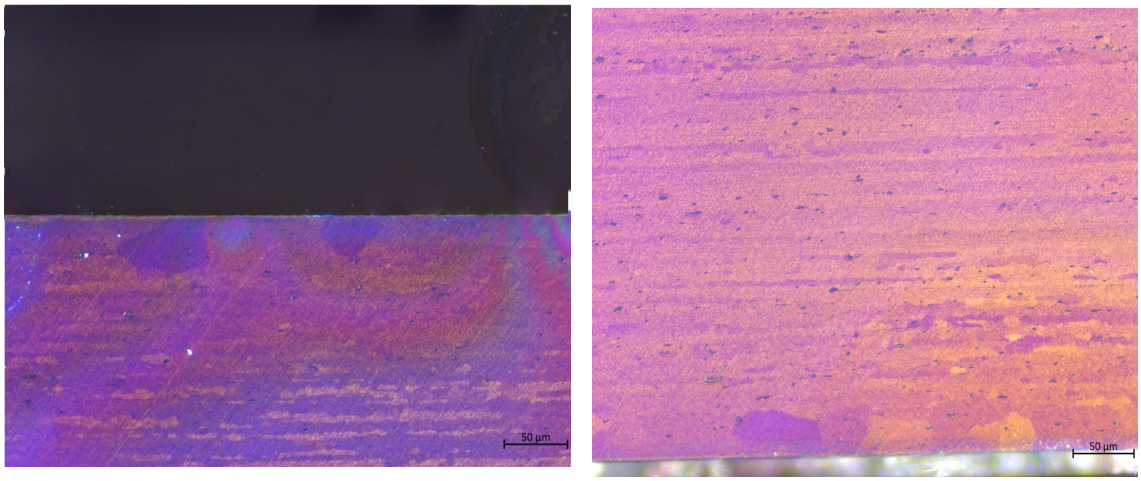

Figure 31: Thin, recrystallized layer on both sides of cross section. The scale bar is 50 µm. magnification is 10x.

4.2 PARTICLE STRUCTURE

The particle structure of the material is shown in figure 32 and 33. The particle distribution for both the extrusion and longitudinal plane are presented. The particles can be seen as the white spots. The particles seem to be slightly aligned along the extrusion direction, although no clear pattern is observed. The particle distribution is inhomogeneous, consisting of areas with both higher and lower particle density. The particles in this material are a mixture of small and larger sized particles. For the particle characterization by imageJ, the particle distribution images presented below were tweaked to increase the contrast between the particles and the matrix, making the characterization easier. The tweaked images uploaded to imageJ have been attached in appendix C.

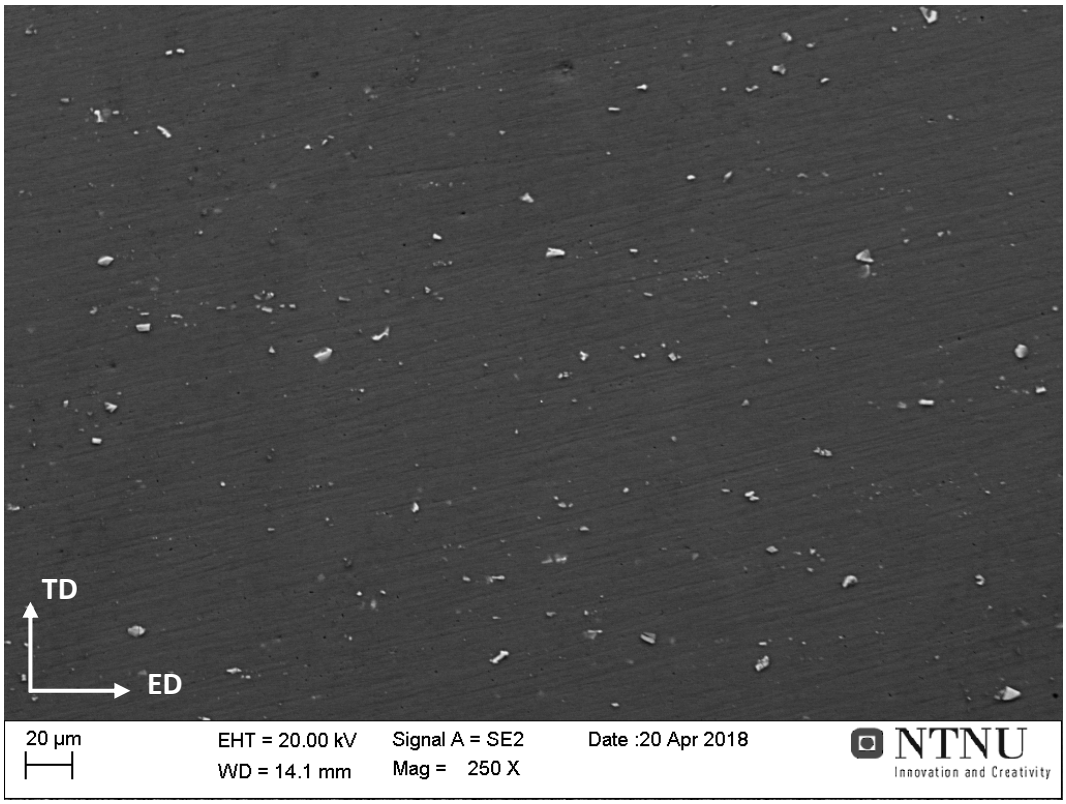

Figure 32: SEM image of the particle distribution in the extrusion plane. 250x magnification.

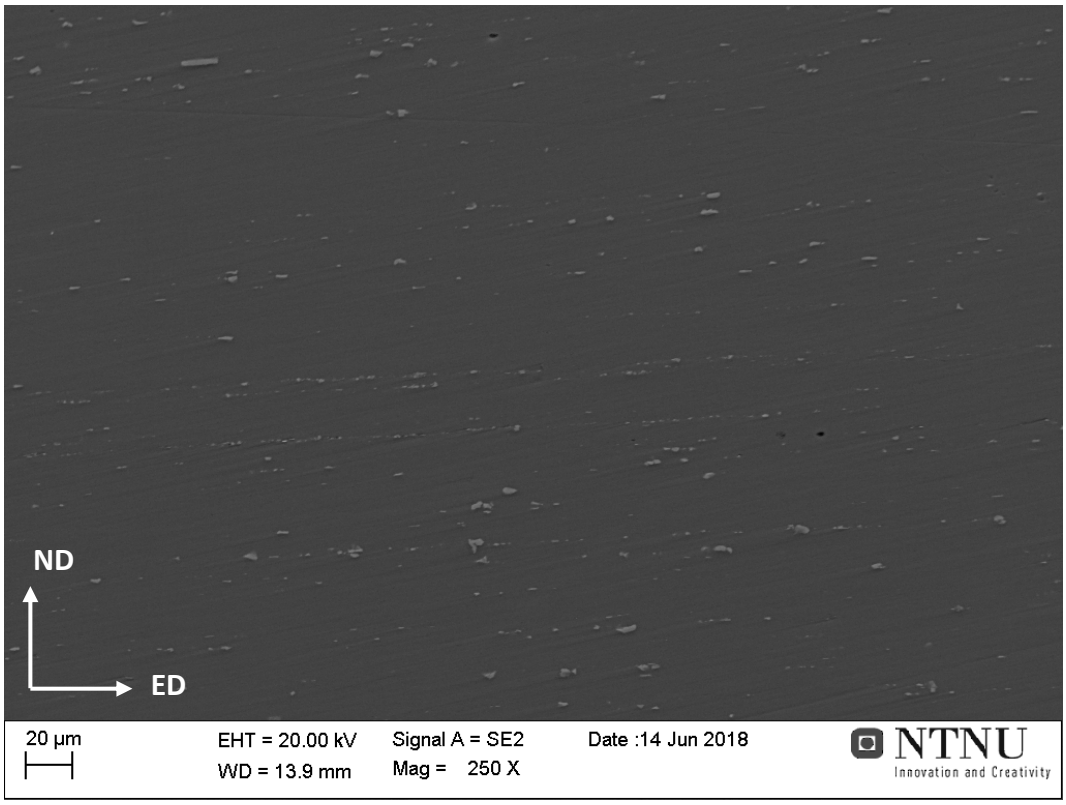

Figure 33: SEM image of the particle distribution in the longitudinal plane. 250x magnification.

By examining figure 32 and 33, the particle density for the longitudinal plane seems to be higher than for the extrusion plane. In addition, there is an increased tendency of particle clustering for the particles in the longitudinal plane. This was further examined by the image analysis software ImageJ, and the result of this examination is displayed in table 8. The analysis revealed a slightly higher particle density for the longitudinal plane. The average particle size is approximately the same.

Table 8: Result from imageJ analysis.

	Extrusion plane	Longitudinal plane
$\frac{\text{Number of particles}}{\text{area}}$ $[\frac{1}{mm^2}]$	2287	2831
ESD [μm]	1.29 ± 0.83	1.3 ± 0.72

To further assess the particles, EDS was used. These results should not be taken too literate, as the analyzed volume is likely to exceed the particle, taking in signals from the matrix as well. However, by comparing the relative compositional difference between particles and matrix, some distinct features can be found regarding the chemical composition of the particles. Particles present in the material is primary intermetallic particles, precipitated strengthening particles and dispersoids, and a chemical analysis would help illuminate the type of particle present. The primary intermetallic particles are commonly iron-based[20], precipitated strengthening particles are Al, Zn, Mg and Cu based[61] while the dispersoids have been reported as being Zr- and Sc-containing. [62]

In table 9 the chemical composition of particles and matrix is compared. Alloying elements that were found in concentrations of less than 1 at% for particles and matrix are not presented. The particle number corresponds to the point number from the EDS scans, and complete compositional results from the EDS scans can be found in appendix B.

Table 9: Chemical composition of particles and matrix.

Alloying element [%at]	Particle 209	Particle 211	Particle 212	Particle 213	Particle 214	Matrix
Fe	14.47	10.58	16.68	16.11	16.45	0
Si	4.1	3.86	6.19	4.33	4.46	0.3
Cu	2.11	1.04	0.2	2.2	2.16	0.17
Mg	1.6	1.8	0.74	1.43	1.38	1.93
Zn	1.88	2.38	0.54	1.86	1.7	2.09

Comparing the point analysis of particles and matrix, the largest compositional difference is found for Fe, where the particles generally are much richer in Fe than the matrix. The same observation can be made for Si, with the particles having a higher Si content than the matrix. For Cu, the compositional differences between particles and matrix were in general smaller, and for particle 212 the difference is insignificant. For Mg and Zn, the concentration differences between matrix and particles were small, suggesting that Mg and Zn were not part of the particles.

Although the results are quite ambiguous, the particles clearly contain Fe and Si. Most of the particles also seem to contain Cu(209, 211, 213 and 214), and they may be $Al_xFe_ySi_zCu_w$ based. Particle 212, with insignificant amounts of Cu, is seemingly $Al_xFe_ySi_z$ based. Based on these results, where the particles evidently contain large amounts of iron, the observed particles are likely primary particles that were not dissolved following casting and homogenization of the extrusion billets. In addition, strengthening precipitates and dispersoids are likely too small for detection in SEM.

By comparing the relative concentration of alloying elements in the particles, a more precise description of the particle stoichiometry can be given. As mentioned in section 2.2.1, no literature was found on the exact chemical composition of primary particles in AA7046. For other 7xxx alloys however, $Al_{23}CuFe_4$, Al_7Cu_2Fe, Al_2CuMg, Fe_3SiAl_{12}, Al_3Fe and AlFeSi have been found. Looking at table 9, the chemical composition of particle 212 corresponds very

well to Fe_3SiAl_{12}. As the other particles seem to contain some Cu as well, no clear identification could be made based on published literature.

4.3 TEXTURE

The texture of the material was investigated to get an indication of the degree of mechanical anisotropy. The specimen investigated was in T6 condition, but as there is no evolution in the grain structure following additional heat treatment to T7 condition, see section 4.1, the presented pole figure is representative for this temper state as well. The scanned area used to generate the pole figure have been added in appendix D. A detailed investigation on the effects of texture and texture evolution was not intended in this study.

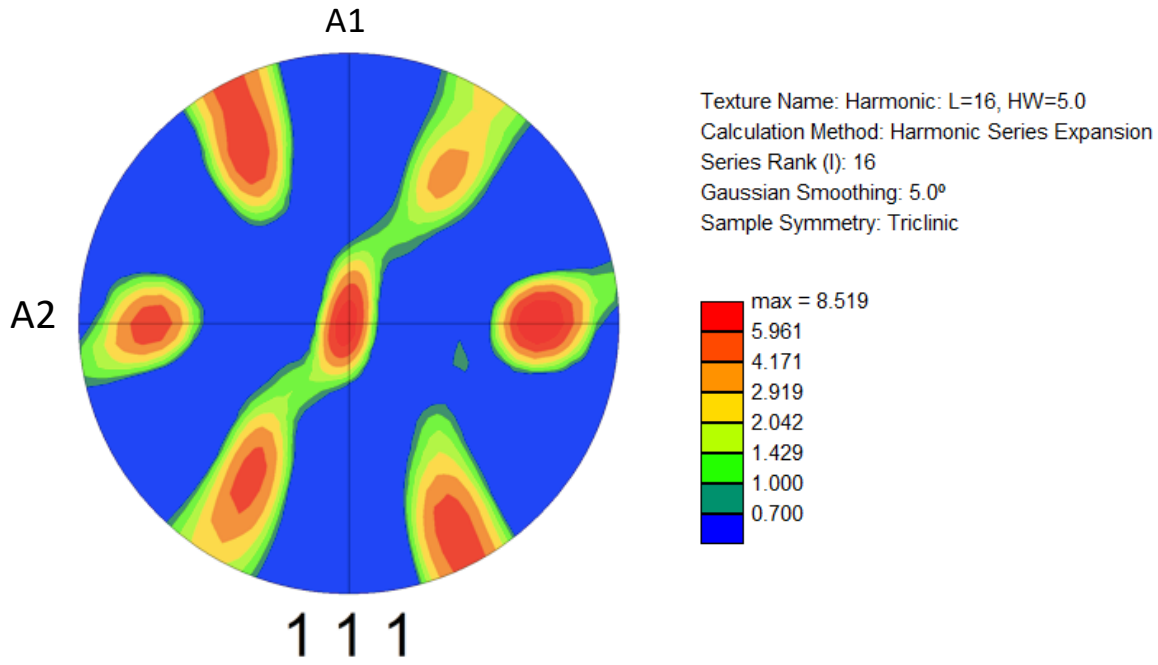

Figure 34: Pole figure of the material with corresponding intensity scale.

Figure 34 presents the pole figure of the material with corresponding maximum intensities. The {111}< $\bar{1}\bar{1}2$> texture component is the most pronounced, although the maximum points are slightly drawn out compared to the ideal orientation. The maximum intensity of 8.5 is not considered high and the material have a weak texture.

4.4 SURFACE ROUGHNESS

Surface roughness parameters obtained prior to fatigue testing is presented in this section. These parameters are taken as the average of 1000 separate line measurements, corresponding to the shaded red area in figure 35. The surface roughness was investigated for both the extruded and machined sides of the fatigue samples. Roughness measurements were conducted for a total of six samples. As the die line surface roughness may vary between profile walls, two samples from each wall were investigated. In figure 36, the three profile walls that samples were machined from has been illustrated. The values presented in table 10 is average values with corresponding standard deviations. The low standard deviation for the extruded sides indicate that the die line surface roughness was independent of profile wall.

Figure 35: Image from the software used to measure the surface roughness, where the red shaded area illustrates the area scanned.

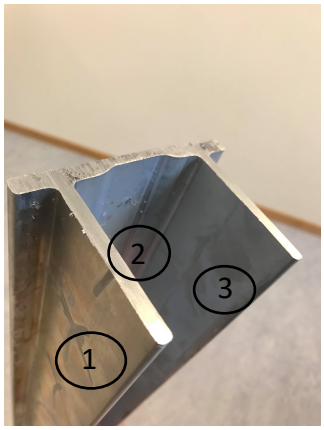

Figure 36: Image of the extruded profile where the profile walls have been marked

Table 10: Surface roughness measurements.

Scan location	R_a (nm)	R_t (µm)	R_z (µm)
Extruded surfaces – Scan parallel to ED	0.35 ± 0.02	2.44± 0.2	2.11± 0.4
Extruded surfaces – Scan perpendicular ED	0.64 ± 0.04	6.45 ± 1.1	4.63 ± 0.23
Machined surfaces	0.18 ± 0.08	1.37 ± 0.7	1.02± 0.6

A clear difference between surface roughness parameters obtained for scans of the machined sides and the extruded surfaces is found. This is expected as some surface scoring is unavoidable in the extrusion process. To illustrate the extent of the die line surface roughness, differences in surface roughness between scans parallel and perpendicularly to the extrusion direction can be observed. The roughness values for scans performed perpendicularly to ED is approximately ~2 times higher than for scans performed parallel to ED, depending on roughness parameter. This clear difference can likely be attributed to the die lines.

4.5 TENSILE TESTING

The results from the tensile tests are given in this section. The data presented are average values, with accompanying standard deviations. The true strain at fracture is used as a ductility measurement.

Table 11: Results from tensile testing

	$\sigma_{0.2}$ [MPa]	σ_{UTS} [MPa]	True strain at fracture
T6	465 ± 4	490 ± 3	0.10
T7	436 ± 2	479 ± 1	0.13

As we identify from table 11, the T6 peak aged condition possess a slightly higher yield strength and ultimate tensile strength than the overaged T7 sample, which is in accordance with theory. The amount of work hardening (i.e. the difference between σ_{UTS} and $\sigma_{0.2}$) is approximately the same for both temper states. The T7 aged specimens have a slightly higher true strain at fracture, indicating a slightly higher ductility.

4.6 Fatigue testing

In this section, the fatigue results obtained in the current work will be presented. The main emphasis of this work is corrosion fatigue testing in a 5 wt% NaCl solution of T6 tempered samples. In addition, some fatigue tests have been conducted on T7 tempered samples in the same solution as well as fatigue tests of pre-corroded samples. Earlier reported work by SINTEF on uncorroded samples of the same alloy tested in air is compared to the fatigue results obtained in this master´s thesis. It must be mentioned that the testing frequency was different between this work and the work of by SINTEF. In this master´s work the frequency of testing was set to 5 Hz, while SINTEF performed testing at 10 Hz. For fatigue testing in a non-corrosive environment, such a small change in the testing frequency is not thought to significantly influence the results. To substantiate this argument, a few un-corroded samples were tested in air at 5 Hz and compared to the work of SINTEF. The results from this has been attached in appendix A. Apart from the testing frequency, all other relevant parameters were identical. The samples were taken from the same extruded profile, went through the same heat treatment and had identical dimensions. The machine used for fatigue testing was also the same.

4.6.1 Comparison of 5 wt% NaCl and air

A comparison of fatigue results obtained for samples in 5 wt% NaCl solution and samples tested in air is presented in figure 37. The plots are presented as fatigue life as a function of stress amplitude. The dashed lines represent the best fit regression line. The results show a considerably lower fatigue lifetime for the samples tested in 5 wt% NaCl compared to air. With a lowered stress amplitude, the difference in lifetime between 5 wt% NaCl and air increased. The stress amplitude corresponding to a lifetime of 10^5 cycles is presented in table 12.

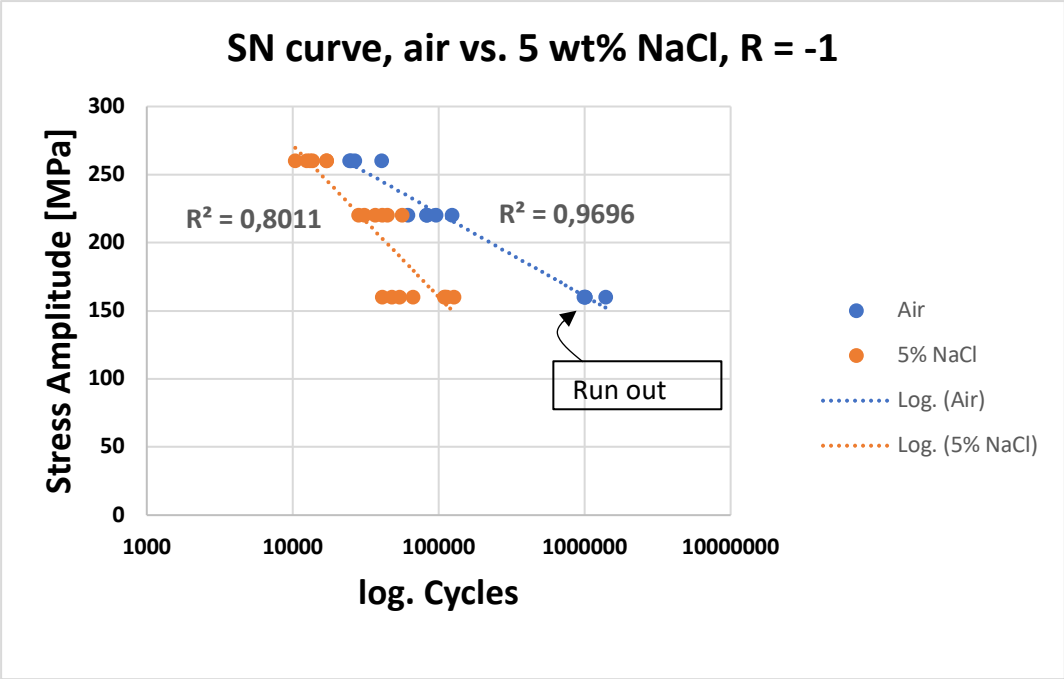

Figure 37: SN curve for samples tested in 5 wt% NaCl and air.

Table 12: Fatigue strength at 10^5 cycles

Air	5 wt% NaCl	Percent change
222 MPa	160 MPa	-32.4%

The regression line was found to be steeper for the samples tested in 5% NaCl than the samples tested in air, i.e. the lifetime changed less with reduced stress amplitudes for the samples tested in 5% NaCl. With regard to scatter, the samples tested in air showed the best behavior with an R^2 value of 0.9696, where $R^2 = 1$ implies an optimal fit.

4.6.2 Pre corroded samples

The intention of this section is to give a better understanding of how the salt solution effects the samples. Therefore, a comparison of samples tested at a stress amplitude of 220 MPa under various conditions is carried out, presented in figure 38. Un-corroded samples tested in air, samples pre-corroded for various times and subsequently tested in air as well as samples exposed to a combination of fatigue and 5 wt% NaCl (i.e. tested in the chamber) were investigated. The samples that were exposed to a combination of fatigue and 5 wt% NaCl had a lifetime ranging from ~2.8-5.6*10^4 cycles, corresponding to an exposure time of ~1.5 – 3 hours. The samples pre-corroded for 5 hours had a longer lifetime, suggesting that the combined effect of fatigue and corrosion is detrimental to fatigue life. Interestingly, no consistent difference was found in lifetime between samples exposed to the salt solution for 5 hours and samples fatigue tested in air. For longer exposure times, 7, 21 and 26 days respectively, clear decreases in fatigue lifetime are observed. For these exposure times, a clear link was found between exposure time and fatigue lifetime, where the samples exposed to 26 days performed worst and the samples exposed for 7 days best.

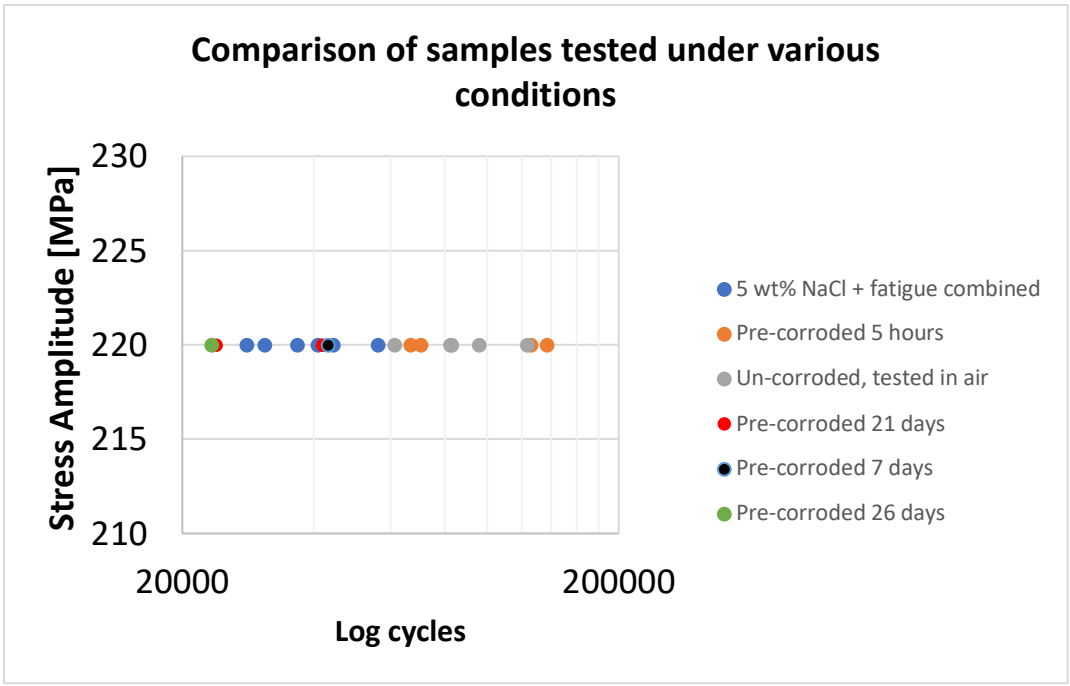

Figure 38: Comparison of samples tested at 220 MPa under different conditions.

4.6.3 Effect of temper state

This section is concerned with a comparison of T6 and T7 tempered samples, tested in 5 wt% NaCl at a stress amplitude of 160 MPa. The tests revealed no significant difference in lifetime between T6 and T7 tempered samples, as seen by figure 39. It must however be stressed that the sample is small, definitely too small to draw any conclusions, and tests should also be conducted at other stress amplitudes. The best way of representing corrosion fatigue susceptibility is to compare the lifetime in air with the lifetime in the salt solution. The results from the fatigue testing in air performed by SINTEF revealed that the temper states performed very similarly in air, as can be seen from figure 40.

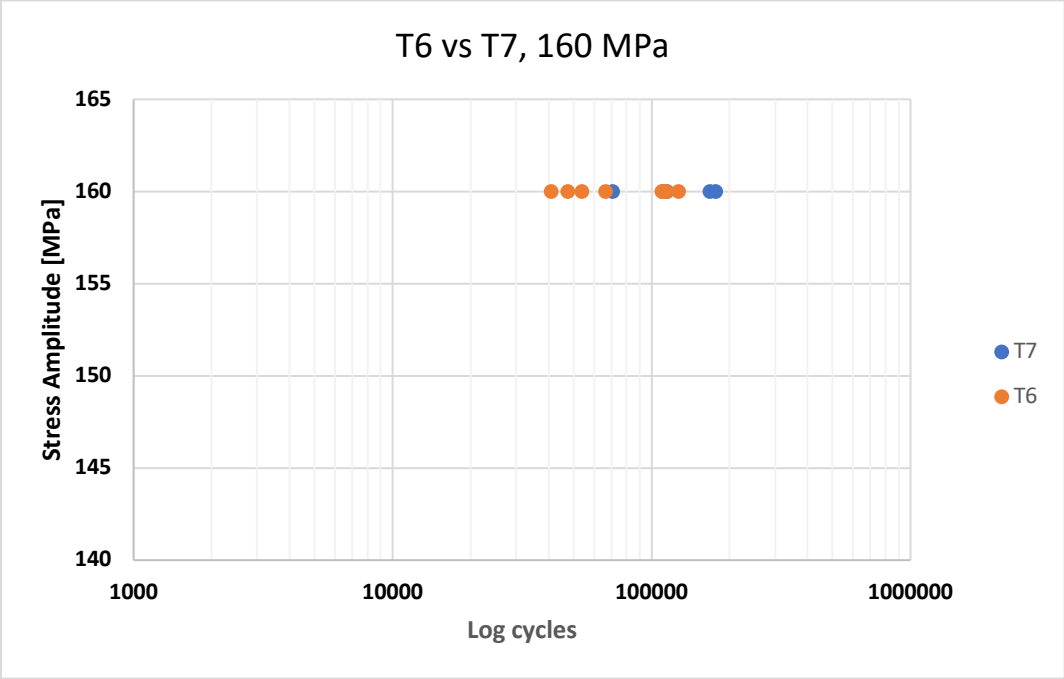

Figure 39: Comparison of corrosion fatigue behavior for T6 and T7 tempered samples.

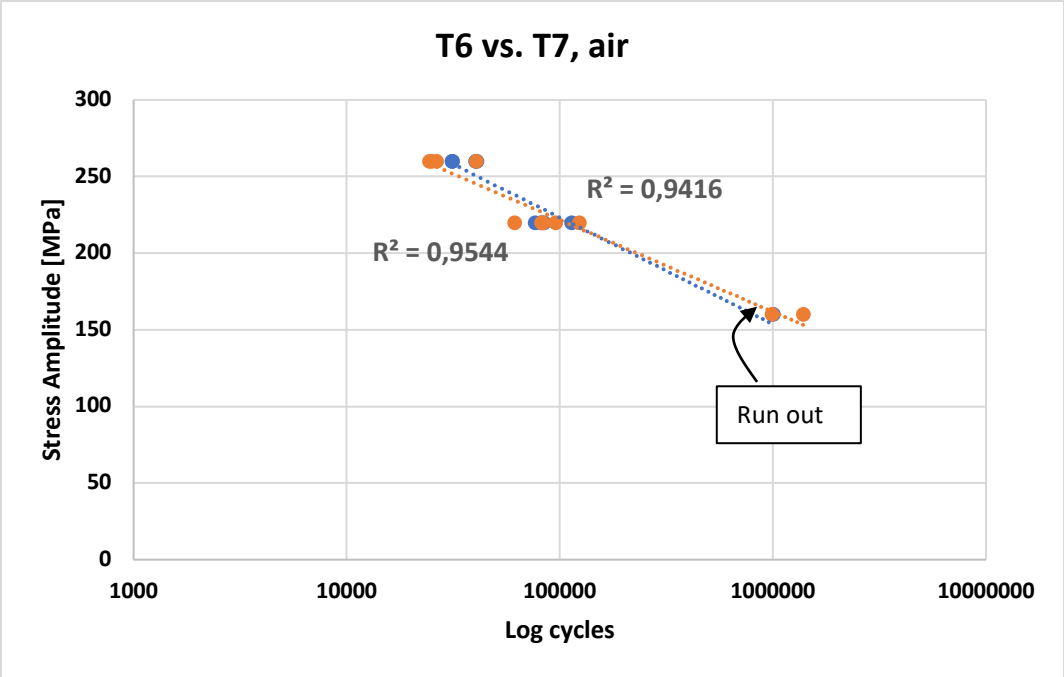

Figure 40: SN curve for T6 and T7 tempered samples tested in air.

4.6.4 Comparison to AA6082

The work in this master´s thesis is a continuation of work done by Lindstad[58] on AA6082. In his work, Lindstad investigated the effect of different surface finishes on corrosion fatigue life. Only machined samples, i.e. similar samples to those evaluated in this thesis, were compared. Lindstad used an R value of 0.1 in his work, while the present work was done with an R value of -1. To account for this difference in mean stress, a Goodman diagram was designed, following the method described in section 2.4.4. The result is presented in figure 41.

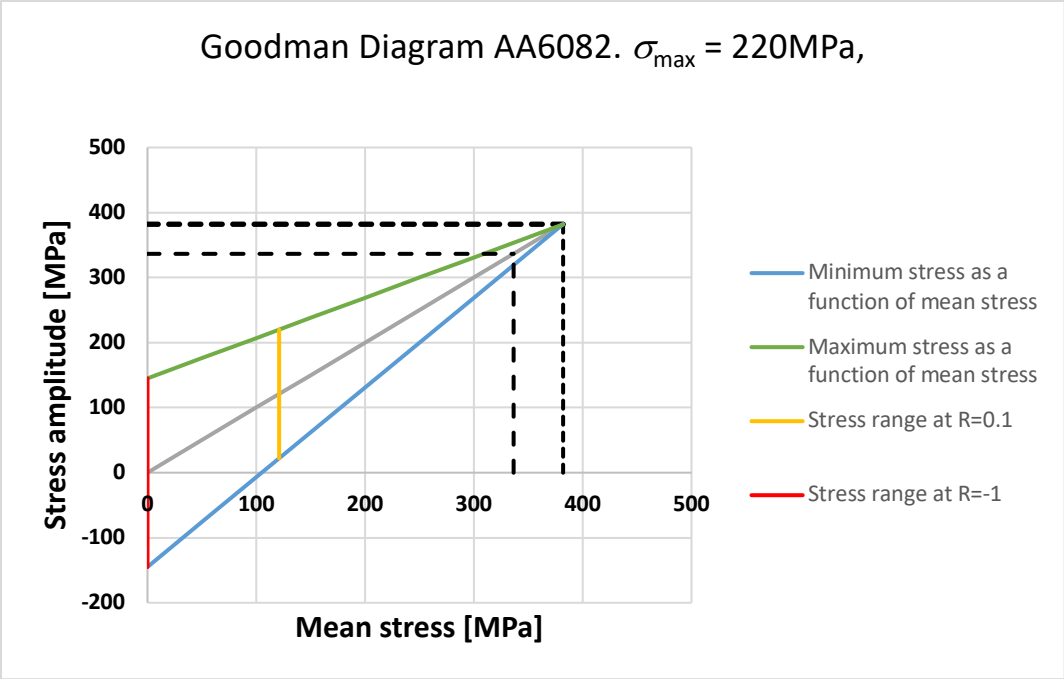

Figure 41: Goodman Diagram constructed to compare corrosion fatigue behavior of AA7046 and AA6082.

As the Goodman Diagram depicts, a reduction in mean stress results in an increased stress range. The stress amplitude corresponding to R = -1, derived by the Goodman Diagram, is σ_a= 145 MPa. The fatigue data obtained by Lindstad for AA6082 and the results obtained in this thesis for AA7046 has been summarized in table 13, together with the approximative results.

Table 13: Summary of results from AA6082 and AA7046 corrosion fatigue testing.

R = 0.1 **σ_{max} = 220 MPa** **σ_{min} = 22 MPa** *6082 Lindstad*	**R = -1** **σ_{max} = 145 MPa** **σ_{min} = -145 MPa** *6082 Lindstad – Goodman approximation*	**R = -1** **σ_{max} = 160 MPa** **σ_{min} = -160 MPa** *7046 – experimental results*	**R = -1** **σ_{max} = 145 MPa** **σ_{min} = -145 MPa** *7046 - linear approximation*
$1.44*10^5$cycles $\pm$ $3*10^4$ cycles		$8.3*10^4$ cycles $\pm$ $3.4*10^4$ cycles	$1.36*10^5$ cycles

4.7 Evaluation of salt solution

To evaluate the effect of the salt solution, the as-extruded surface of samples exposed to the salt solution under various conditions were investigated in SEM. This was primarily to investigate the extent of pitting, which has been proposed as one of the main crack initiation mechanisms in corrosion fatigue.

4.7.1 Samples fatigue tested in salt solution

This section is concerned with a comparison of samples fatigue tested in the 5 wt% NaCl solution. A regular, uncorroded specimen fatigue tested in air is added for comparison. For the sample tested in air, figure 42, no characteristic feature can be observed, apart from the clearly recognizable die lines introduced during extrusion. At the highest stress amplitude of 260 MPa, figure 43, the selected sample was exposed to the salt solution for ~1 hour. Some pits can be observed on the surface. In figure 44 a sample tested at a stress amplitude of 220 MPa is presented, corresponding to an exposure time of ~3 hours. We notice that more and larger pits can be observed on the extruded surface, and white particles is observed inside some pits. There are also signs of attacks along the grain boundaries, revealing the surface grains. As the stress amplitude is further reduced to 160 MPa, figure 45, corresponding to an exposure time of ~6 hours, the pit density and pit size is further increased. An unloaded sample exposed to the salt solution for ~6 hours can be seen in figure 46. Regarding pit density, no clear difference was found between the loaded and unloaded sample. However, a large crack can be found for the sample tested in the salt solution, which is not found for the unloaded sample. An overview of the maximum pit diameter as a function of exposure time is presented in table 14.

Table 14: Maximum pit diameter as a function of exposure time.

Exposure time (hours)	Maximum pit diameter (µm)
~1 hour	0.4
~3 hours	1.1
~6 hours	4.3

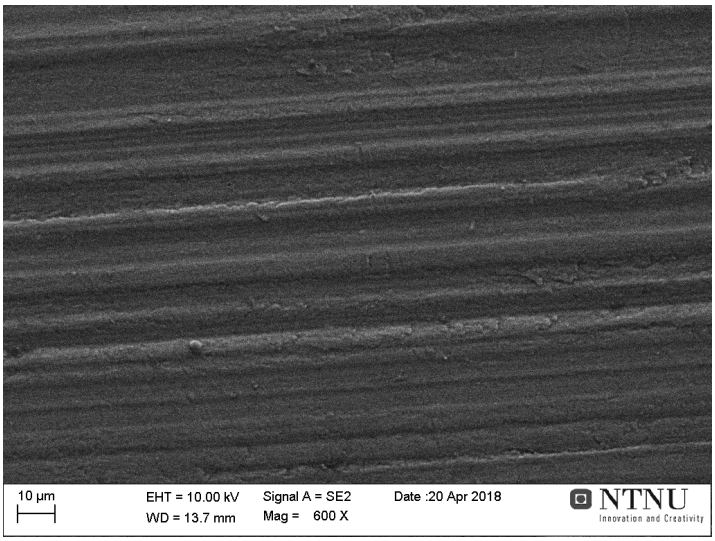

*Figure 42: Air, 160 MPa, 1.38*10^6 cycles. 600x magnification.*

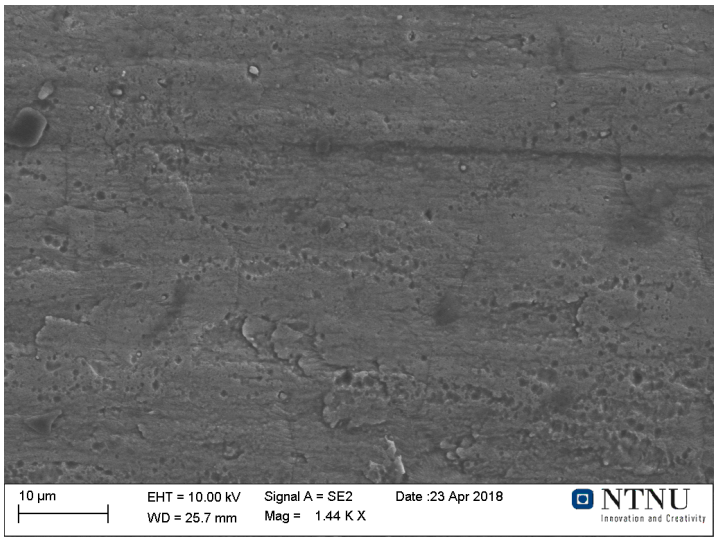

*Figure 43: 5 wt% NaCl, 260 MPa, 1.7*10^4 cycles. 1440x magnification.*

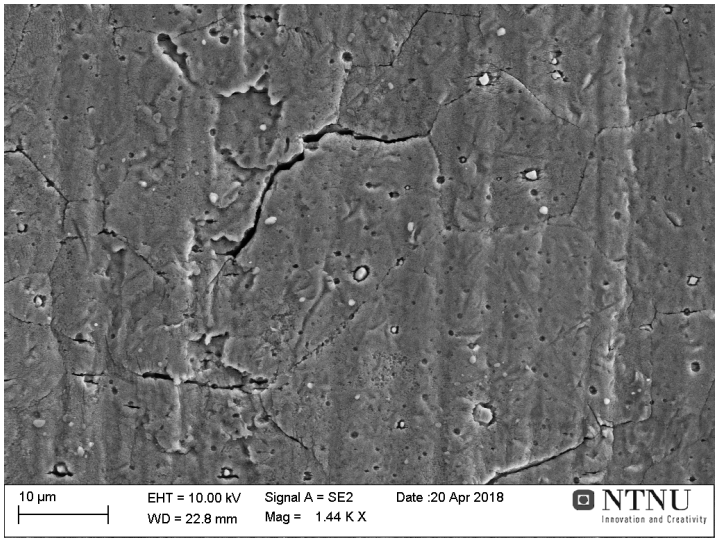

*Figure 44: 5 wt% NaCl, 220 MPa, 5.6*10^4 cycles. 1440x magnification.*

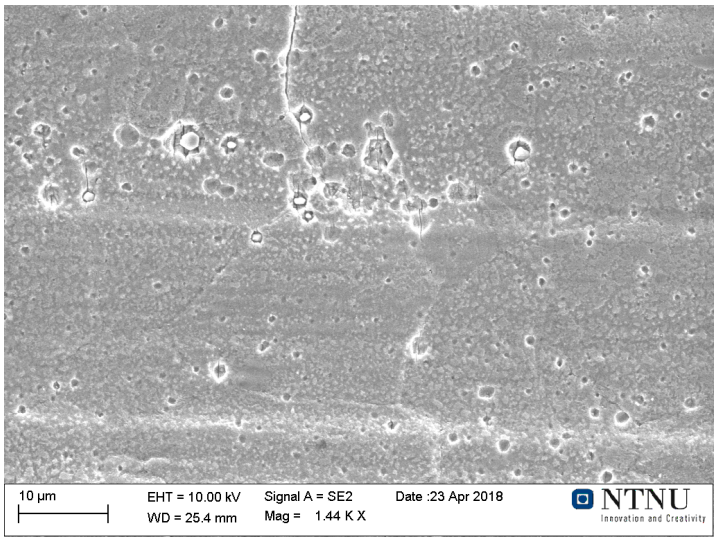

*Figure 45: 5 wt% NaCl, 160 MPa, 1.09*10^5 cycles. 1440x magnification.*

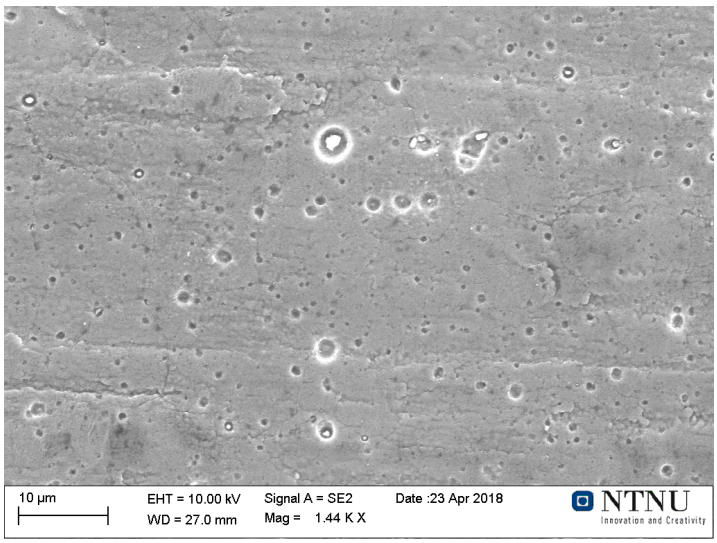

Figure 46: 5 wt% NaCl, no load. 1440x magnification.

For the samples presented above there also seems to be some preferential attacks along the grain boundaries. To further investigate this, the specimen presented in figure 44 was anodized in as-extruded condition and investigated in light microscope, see figure 47. The view plane is the ED-TD plane. Here, the surface recrystallized grains mentioned in section 4.1 are clearly recognizable, as well as the die lines. The abovementioned attacks along the grain boundaries is also visible. Inside the white circles we see how black “lines” can be seen separating the grains, suggesting a grain boundary attack.

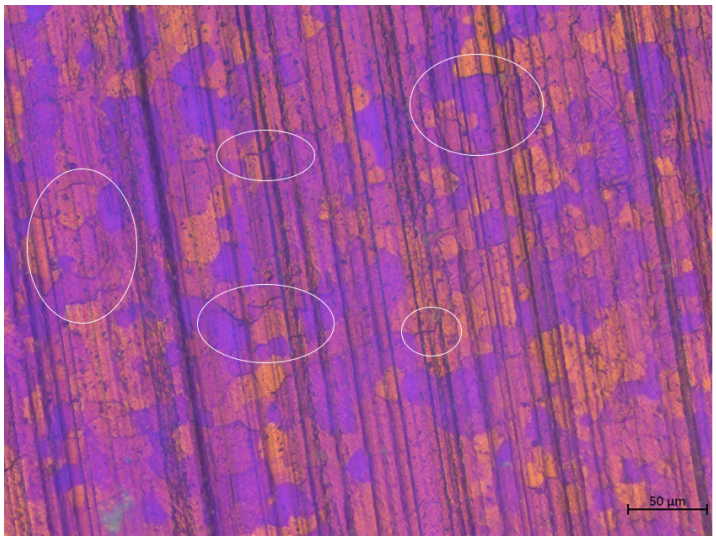

Figure 47: LOM image illustrating grain boundary attacks, encircled in white. 10x magnification. The scale bar is 50 µm.

4.7.2 PRE-CORRODED SAMPLES

All pre-corroded samples were tested at a stress amplitude of 220 MPa. For the sample exposed to the salt solution for 5 hours, figure 48, only small pits are observable on the sample surface. For 7 days exposure, figure 49, the pits have clearly increased in size (notice the magnification difference). For 26 days exposure, figure 50, the corrosion attacks are more severe, and the characteristic die lines are no longer visible. The small “notches” observed on the surfaces in figure 49 and 50 are likely corrosion products not removed during submersion in the CrO_3 + H_3PO_4 solution.

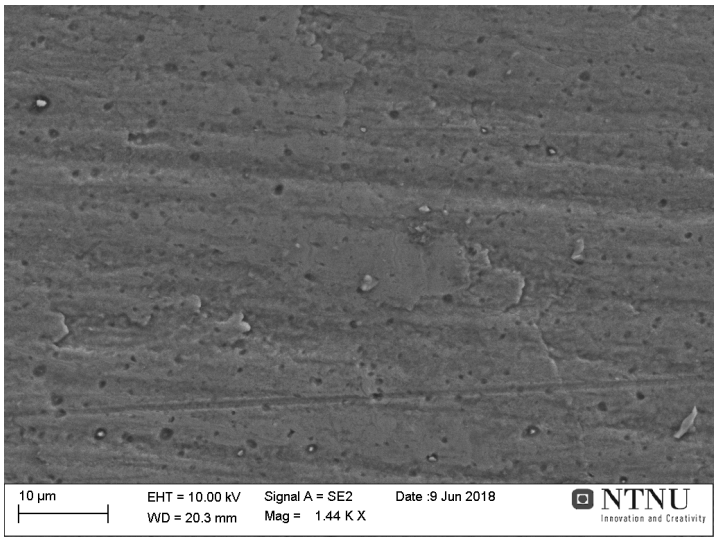

*Figure 48: 7*104 cycles, 5 hours exposure. 1440x magnification.*

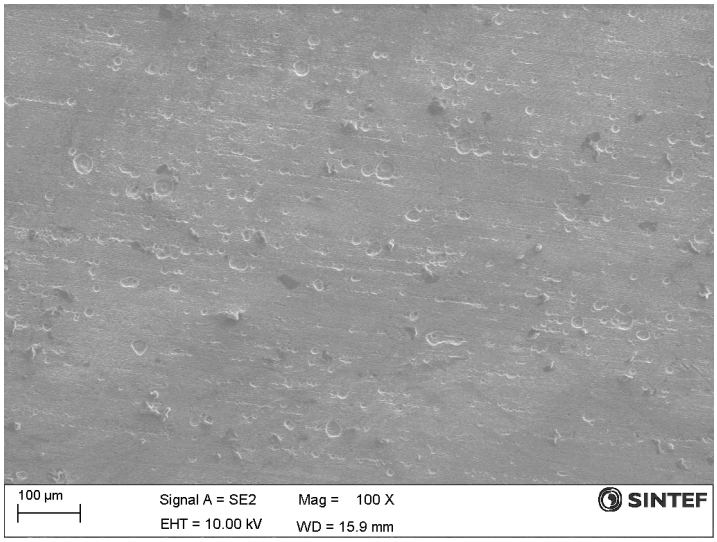

*Figure 49: 4.3*104 cycles, 7 days exposure. 100x magnification.*

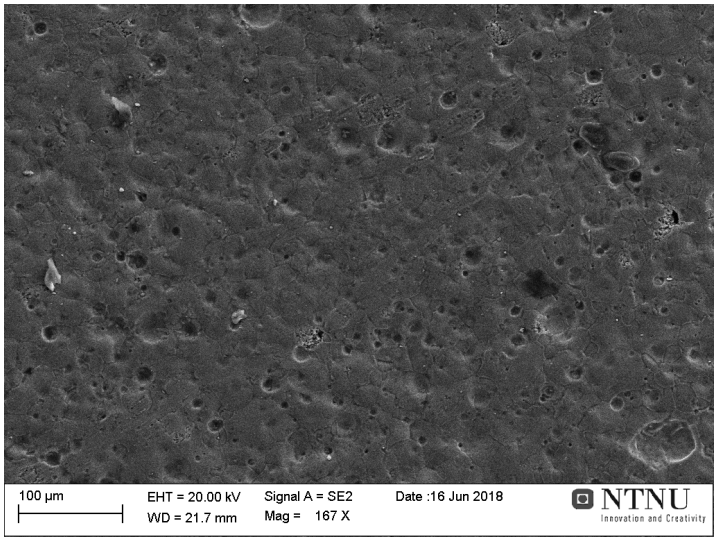

*Figure 50: 2.3*104 cycles, 26 days exposure. 167x magnification.*

4.7.3 Effect of temper state

In this section a sample in T6 and T7 condition is compared, figure 51 and 52 respectively, tested at the same stress amplitude of 160 MPa. The maximum pit diameter for the two temper states are approximately the same, but the number of pits seem to be slightly higher for the T6 tempered sample. A microcrack is also visible for the T6 tempered sample.

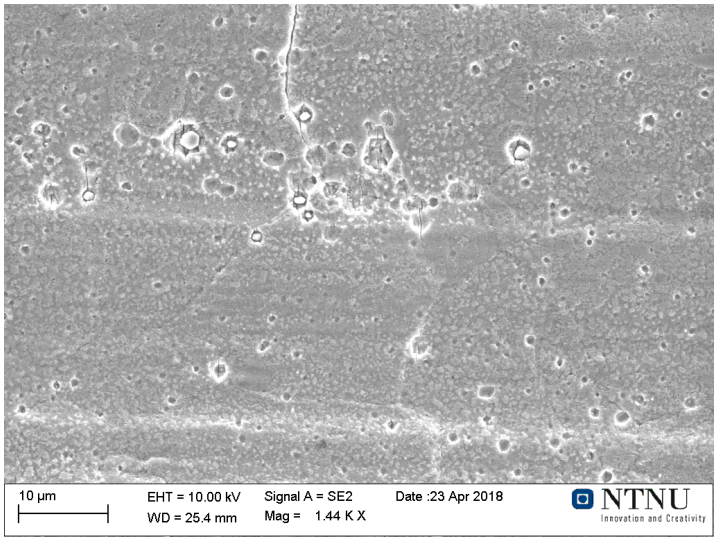

Figure 51: 5 wt% NaCl, 160 MPa. T6. 1440x magnification.

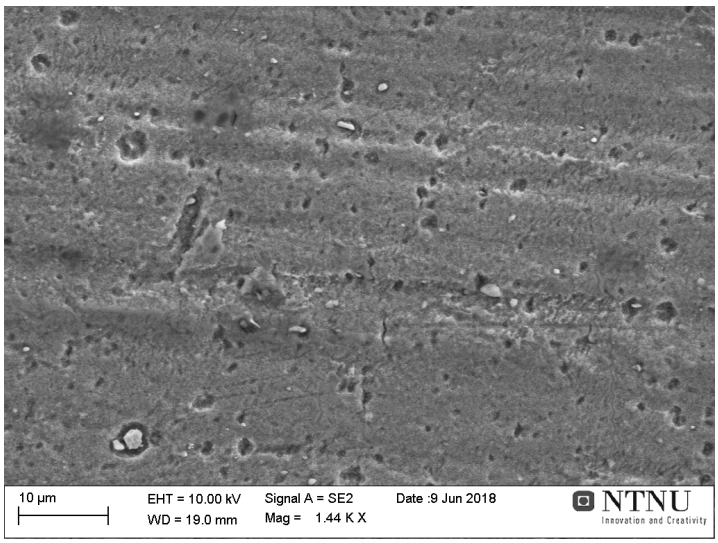

Figure 52: 5 wt% NaCl, 160 MPa. T7. 1440x magnification.

4.7.4 PIT DENSITY DIFFERENCES BETWEEN EXTRUDED AND MACHINED SIDES

An interesting observation that were clearly visible for the pre-corroded samples exposed at longer times was a difference in pit size and density between the extruded and machined surfaces of the fatigue samples. In figure 53 and 54, a sample exposed to the salt solution for 3 weeks before fatigue testing is presented. As we see from the figure, pit size and density is evidently higher for the machined surface. The same trend is clear for a sample exposed to the salt solution for 26 days, figure 55 and 56, where the machined surface clearly contain more and larger pits than the extruded surface.

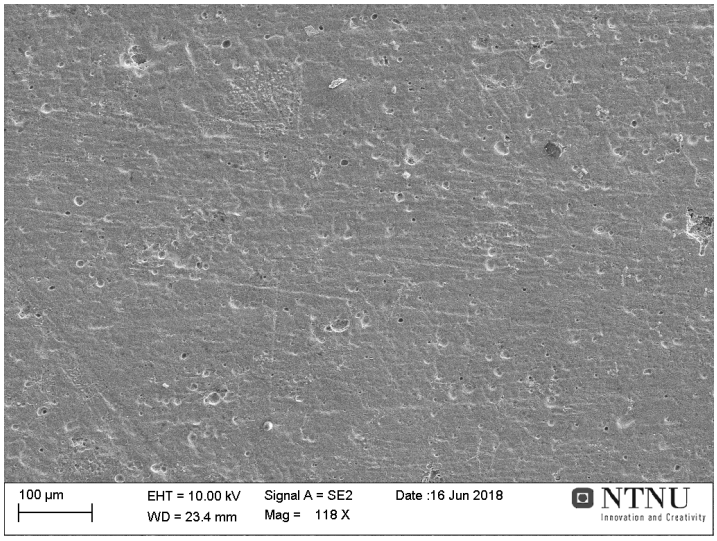

Figure 53: Extruded surface, 21 days exposure. 118x magnification.

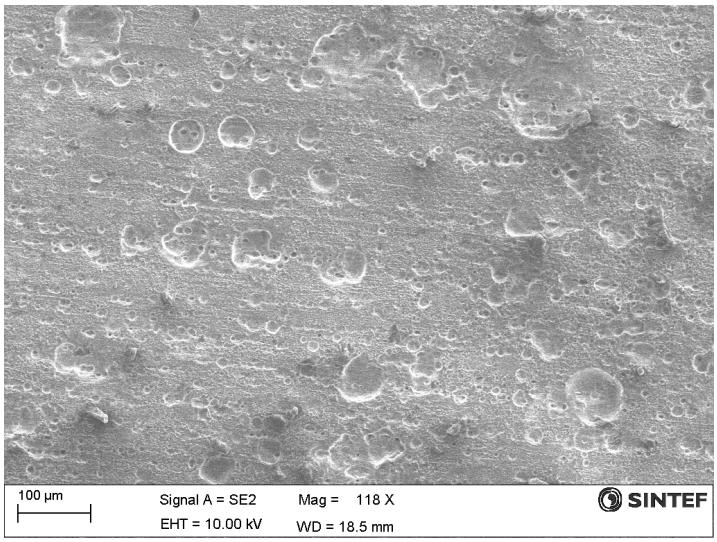

Figure 54: Machined surface, 21 days exposure. 118x magnification.

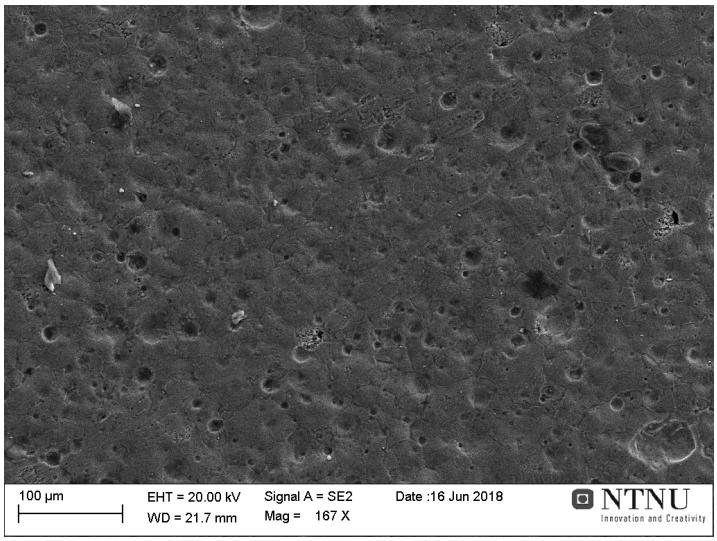

Figure 55: Extruded surface, 26 days exposure. 167x magnification.

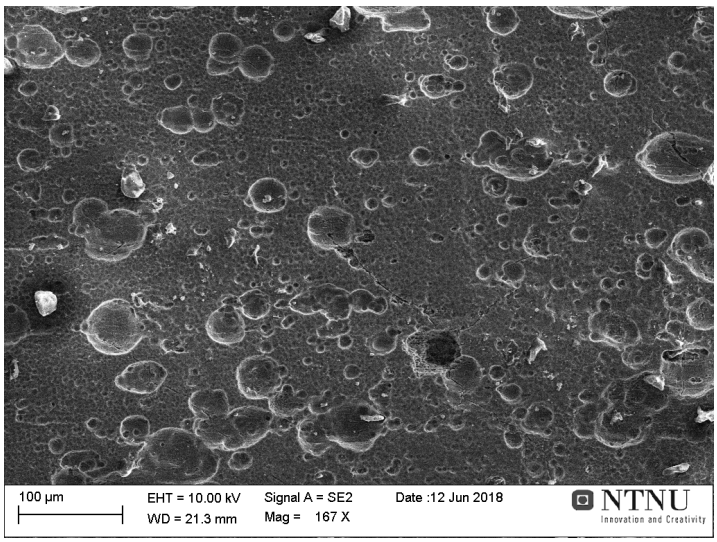

Figure 56: Machined surface, 26 days exposure. 167x magnification.

4.8 EDS OF CORROSION PITS

In addition to the EDS analysis presented in section 4.2, particles located inside corrosion pits were analyzed. The results are presented the same way as in section 4.2, and only the alloying elements found to differ significantly for particles and matrix are presented. Complete compositional results from the EDS scans can be found in appendix B. Table 15 presents a chart where the chemical composition of particles and matrix are compared.

Table 15: Result from EDS analysis of corrosion pits.

Alloying element [%at]	Particle 55	Particle 57	Matrix
Fe	5.38	4.21	0
Si	3.51	3.12	0.3
Cu	0.66	0.55	0.17
Mg	2.01	2.15	1.93
Zn	1.67	1.7	2.08

Comparing the point analysis of particles and matrix, the largest compositional difference is found for Fe, where the particles are significantly richer in Fe than the matrix. The same observation can be made for Si, with the particles having a higher Si content than the matrix. Unlike most of the particles presented in section 4.2, Cu does not seem to be part of the particle composition in these particles. For Mg and Zn, the compositional differences between particles and matrix are insignificant, suggesting that these elements were not part of the particle composition.

Particle 55 and 57 are likely $Al_xFe_ySi_z$ based. Compared to the particles presented in section 4.2, the ratio of Fe/Si is much smaller for these particles. A possible reason, assuming some

noise from the matrix, is that signals from the matrix have diluted the particle signal, which makes sense as some Si is found in the matrix but no Fe. The contribution from the matrix is however not enough to explain such a large composition difference, and it is therefore unlikely that the particles correspond to Fe_3SiAl_{12} as suggested in the literature.

4.9 Fractography

To achieve a better and more detailed insight into the failure mechanisms surrounding the fatigue samples, fractography was performed. Fractography was conducted with basis in the fatigue results, and the fractographic results will be presented in a similar way. First, fractographs of samples fatigue tested in the salt solution will be presented and compared to samples fatigue tested in air, to better understand how the salt solution affects the fatigue tested samples. Samples tested in the salt solution at all stress amplitudes were investigated, primarily to see if any difference in crack initiation mechanism with increased exposure time in the salt solution could be found. Samples in T7 condition tested in the salt solution will also be presented, as well as pre-corroded samples.

4.9.1 Samples tested in 5 wt% NaCl

The fatigue fractured surface

The fatigue fractured surface of a sample tested in the salt solution at a stress amplitude of 160 MPa is presented in figure 57 and a sample tested at the same stress amplitude in air is presented in figure 58. These two figures are representable for all investigated samples tested in the salt solution and in air, in the sense that crack initiation and crack propagation

always was found in the corner area between the machined and extruded surfaces. The numbers 1-3 denote characteristics of fatigue failures, where 1 denote crack initiation site, 2 denote area of crack propagation while 3 denote area of final fracture. The final fracture, as commonly observed in fatigue, created a 45° angle with the loading direction. The white line in figure 57 illustrates the end of the fatigue fracture zone. For the samples tested in salt water, the size of this zone was found to increase with increased fatigue lifetime.

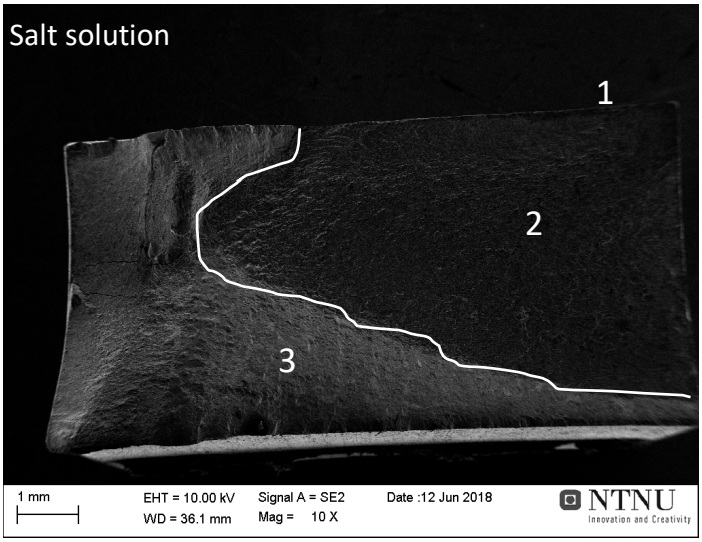

Figure 57: Sample fatigue tested at 160 MPa, representative for the samples tested in salt solution.

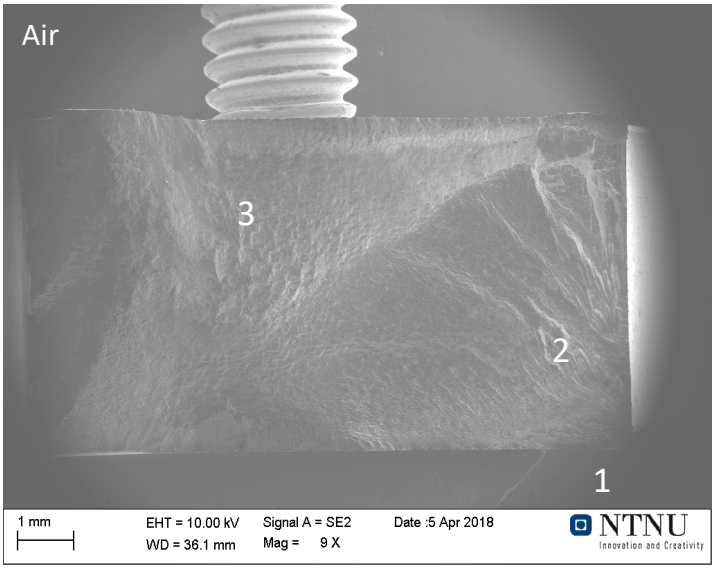

Figure 58: Sample fatigue tested at 160 MPa, representative for the samples tested in air.

Crack initiation

With regards to the crack initiation site, and its origin, differences between samples tested in the salt solution and in air were clearer. To determine the crack initiation site the surface in the area where the fatigue crack had propagated were examined. For the samples tested in the salt solution there were several corrosion caused features that were observed, which all could be responsible for crack initiation. Therefore, several cases will be presented, and the likeliness of each mechanism will be discussed in section 5. The first example, given in figure 59 and further magnified in figure 60, is thought to be a result of a localized corrosion attack. The white "notch" seen at the surface to the left of the red square is thought to be a corrosion product that was not fully removed during submersion in the CrO_3, H_3PO_4 solution. To underline the possibility of crack initiation at the localized corrosion attack, individual grains can be seen in figure 60, which are thought to be visible due to grain boundary corrosion. Signs of grain boundary corrosion were also found when investigating sample surfaces in SEM, as noted in section 4.7. Another suspected mechanism is presented in figure 61, where the extruded surface close to the fracture surface is presented. A high density of corrosion pits can be seen, and an example of this has been enclosed by the red circle. In addition, several microcracks are also readily observed on the surface. The microcracks are thought to originate from preferential attacks of active surface slip bands, caused by rupture of the oxide film during cyclic loading. When the fracture surface was investigated, figure 62, a large crack was found at the surface, as well as slip bands in the crack vicinity. Another proposed origin for crack initiation is crack initiation at corrosion pits, due to stress concentrations at the pit base. A magnification of such a corrosion pit is given in figure 63.

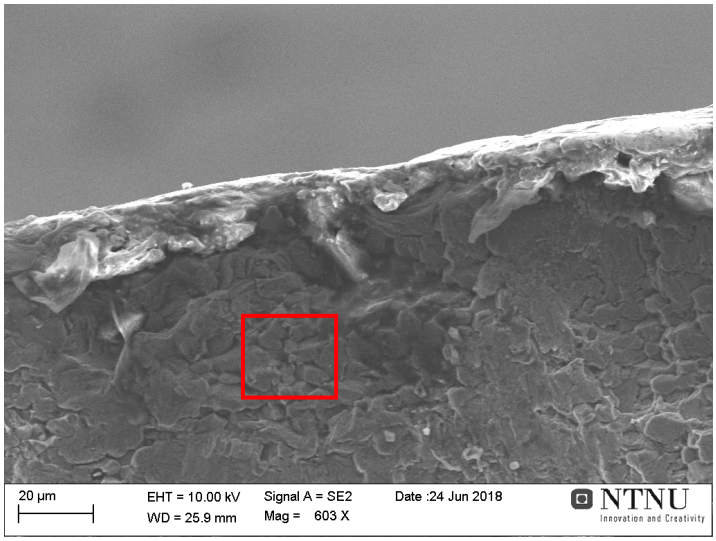

Figure 59: Magnification of potential crack initiation site. Found for sample tested at 220 MPa.

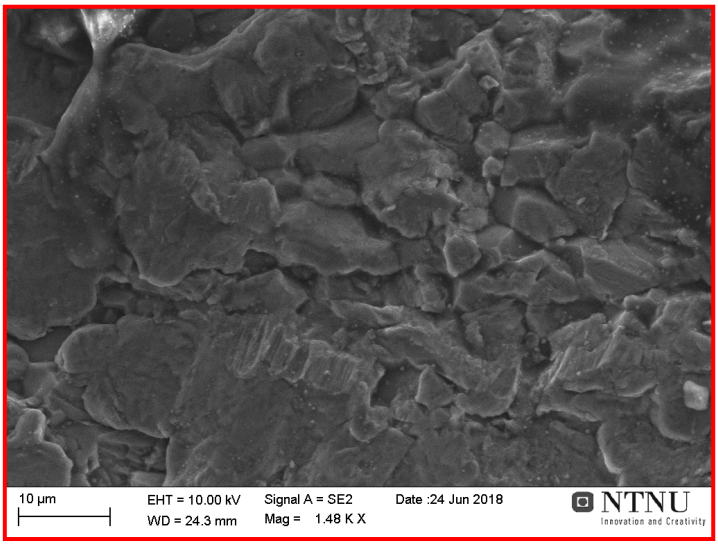

Figure 60: Magnification of the crack initiation site presented in figure 57.

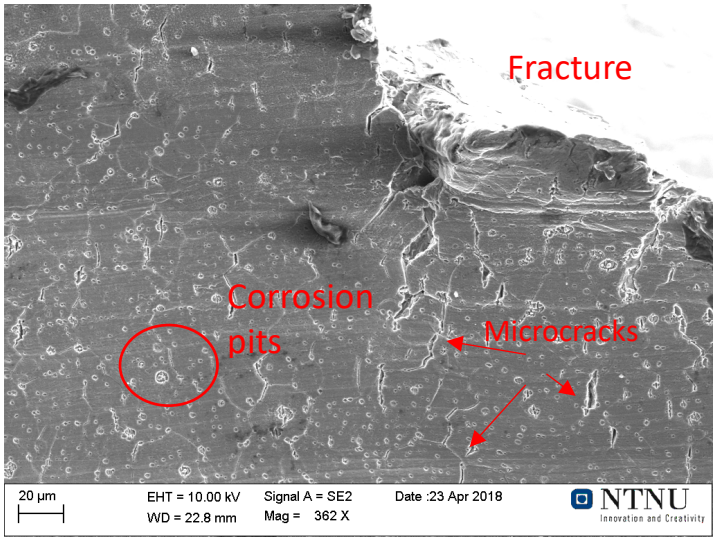

Figure 61: Extruded surface of sample tested at 160 MPa.

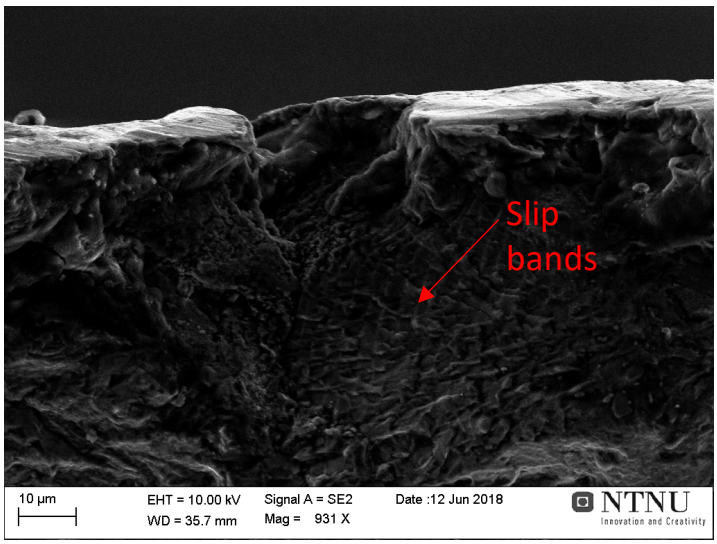

Figure 62: Fracture surface of sample presented in figure 61.

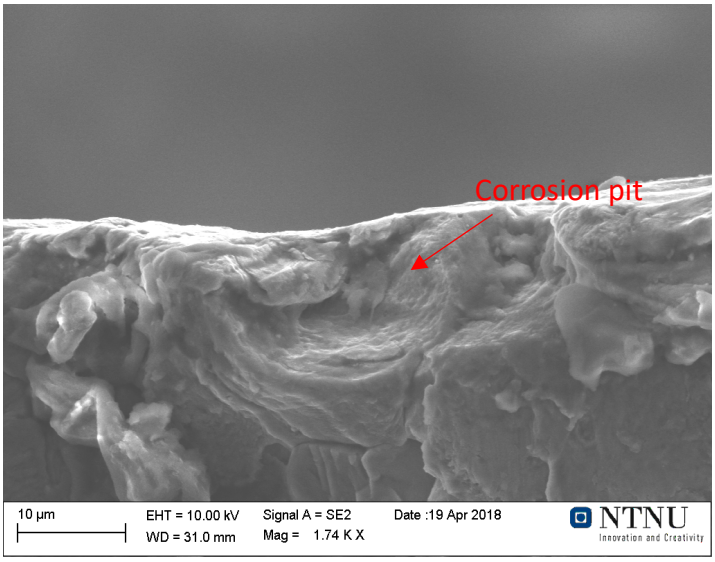

Figure 63: Corrosion pit at the fracture surface for sample tested at 160 MPa.

Crack initiation in air

For the un-corroded samples tested in air, cracks were thought to initiate at the sharp corners between the extruded and machined surfaces. A picture illustrating the corner sharpness is presented in figure 64 A). A lower magnification image of the fracture surface, showing how river lines emanate from the corner is given in figure 64 B). A further magnification taken in SEM showing the corner sharpness is given in figure 65. It is worth noting that the samples received no further treatment after machining, i.e. no rounding of corners or similar treatments which could have forced crack initiation to occur elsewhere.

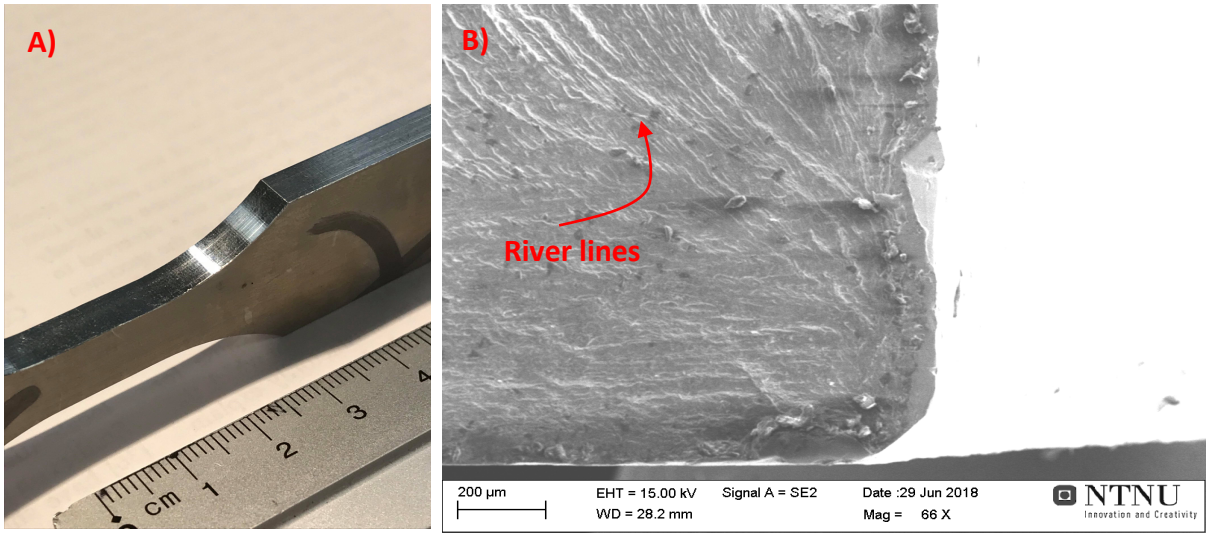

Figure 64: (A) shows an image of the fatigue specimens, illustrating the sharpness of the corner separating the machined and extruded sides. (B) is a magnification of the fracture surface, where river lines are seen emanating from the corner.

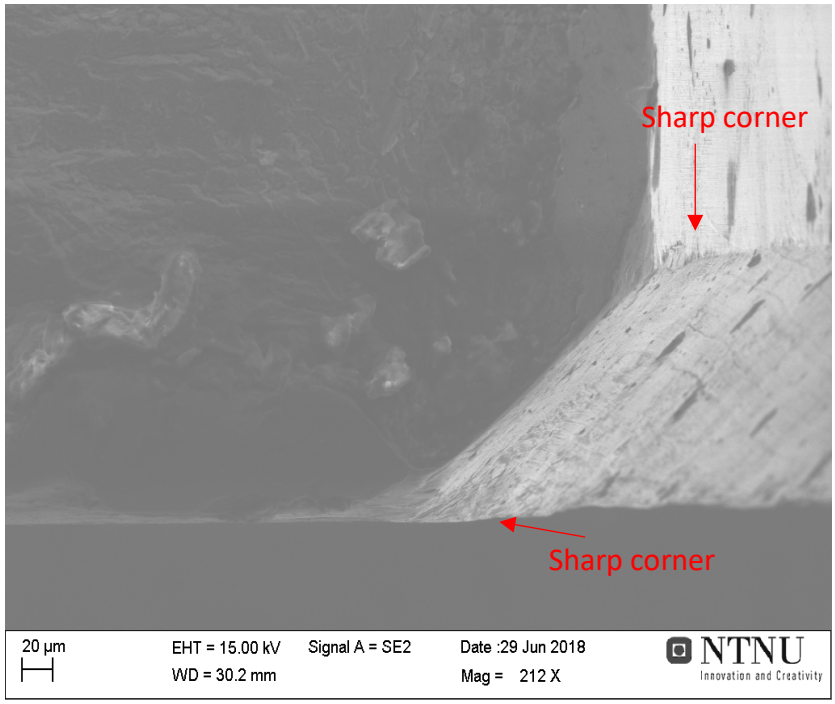

Figure 65: Illustration of the sharp corners separating the machined and extruded surfaces.

Crack propagation

In the crack propagation stage, evidence of the embrittling medium were evident. For the samples in air, the striations are smooth with rumples due to plastic blunting by shear at the crack tip, as seen in figure 67. In figure 66 a sample from the salt solution is presented, and the striations have a roughened appearance due to embrittlement. For the salt solution, secondary cracks could also be observed among the striations. The mode of crack growth for both salt solution and air were found to be transgranular, presented in figure 68. In the presented SEM image from the salt solution, pores can also be observed. For the presented sample tested in air, striations are visible in the vicinity of the crack. A better representation of the transgranular crack propagation is given in figure 69, where the anodized as-extruded surface of a sample tested in salt solution and in air is presented, respectively. The large crack seen in both figures is the propagating fatigue crack, and it can be seen how the crack propagates across the grain boundaries. For the sample tested in the salt solution, figure 69 A), microcracks are also observed, and it is probable that this sample failed by preferential attacks of surface slip bands, as described above. The black "lines" seen among the grains are die lines.

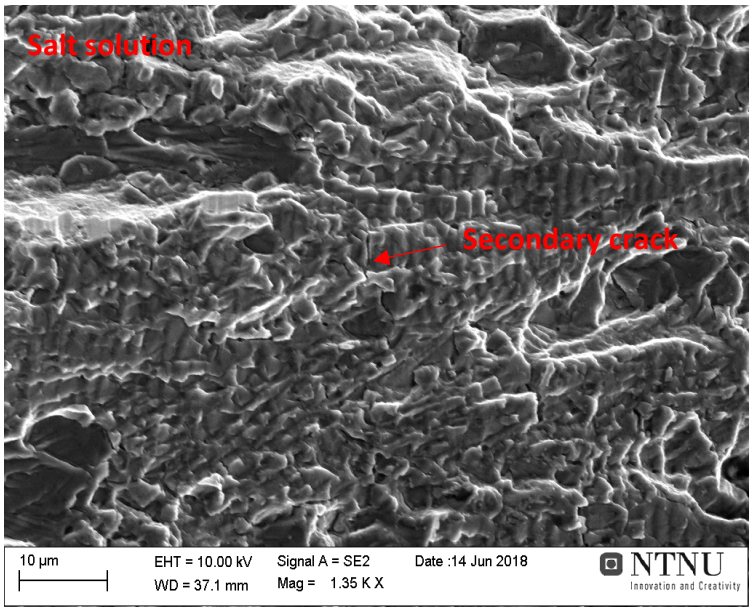

Figure 66: Striation morphology for samples tested in salt water.

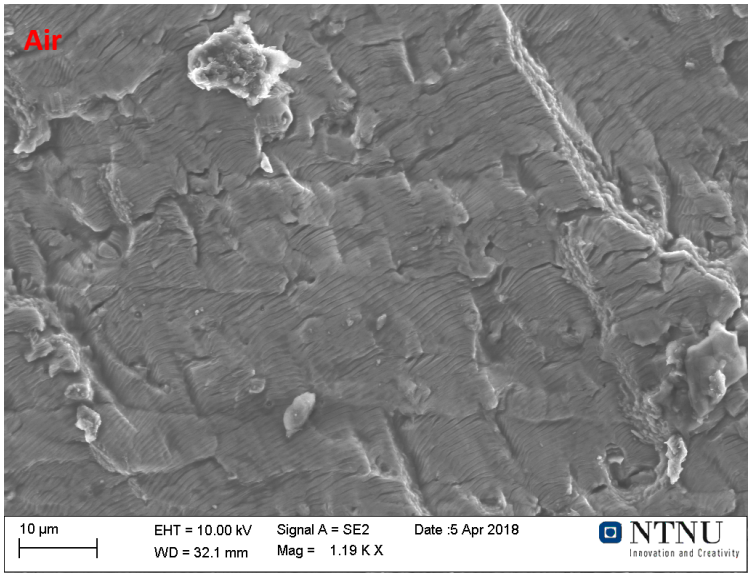

Figure 67: Striation morphology for samples tested in air.

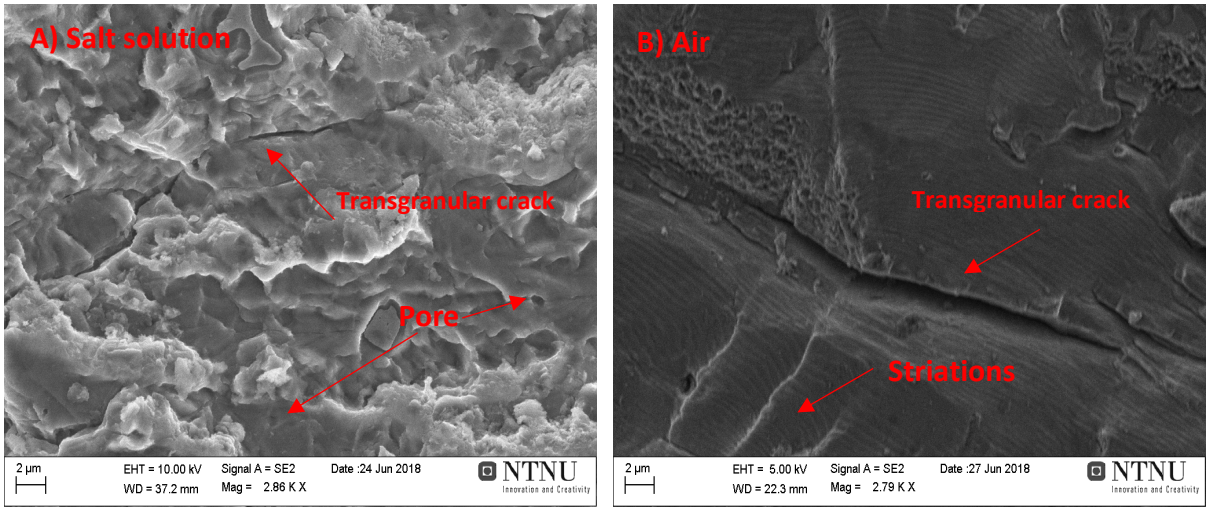

Figure 68: (A) stage II crack growth for samples tested in salt solution. (B) Stage II crack propagation for samples tested in air

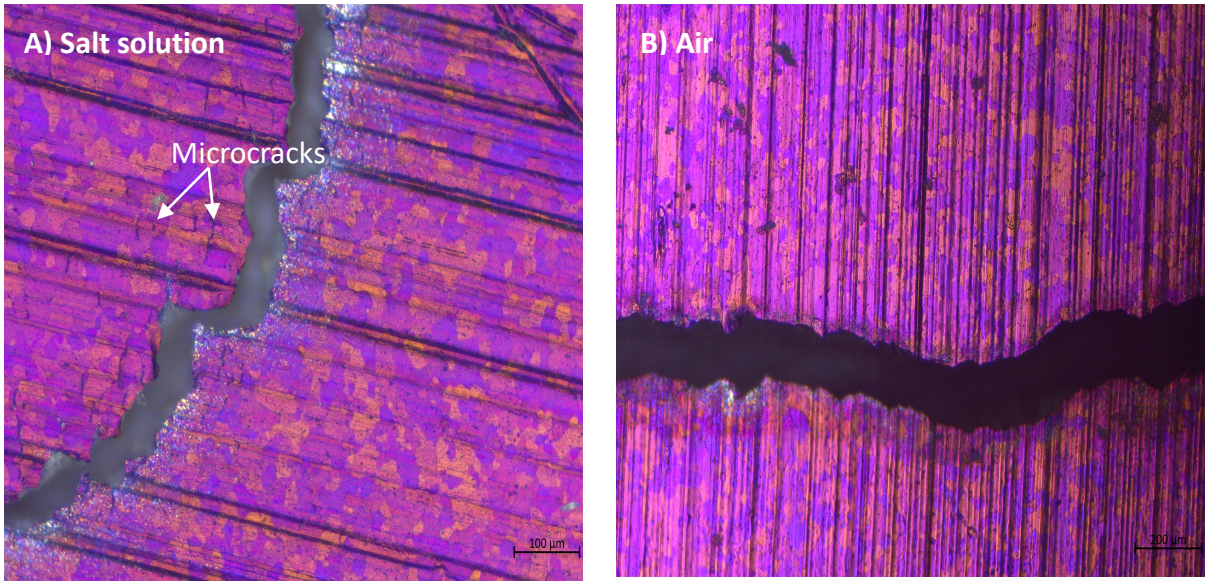

Figure 69: LOM micrographs illustrating the transgranular crack propagation found for samples in salt water and in air.

Final fracture appearance

The final fracture appearance of samples tested in the salt solution and in air were carefully examined to see if any differences could be found, as an embrittling medium may have given rise to a more brittle fracture mechanism for the samples exposed to the salt solution. The sample that was exposed to the salt solution for the longest time was chosen for comparison. As figure 70 shows, no apparent difference can be found, and both samples tested in the salt solution and samples tested in air had a mixed mode fracture mechanism with both dimples and micro shear.

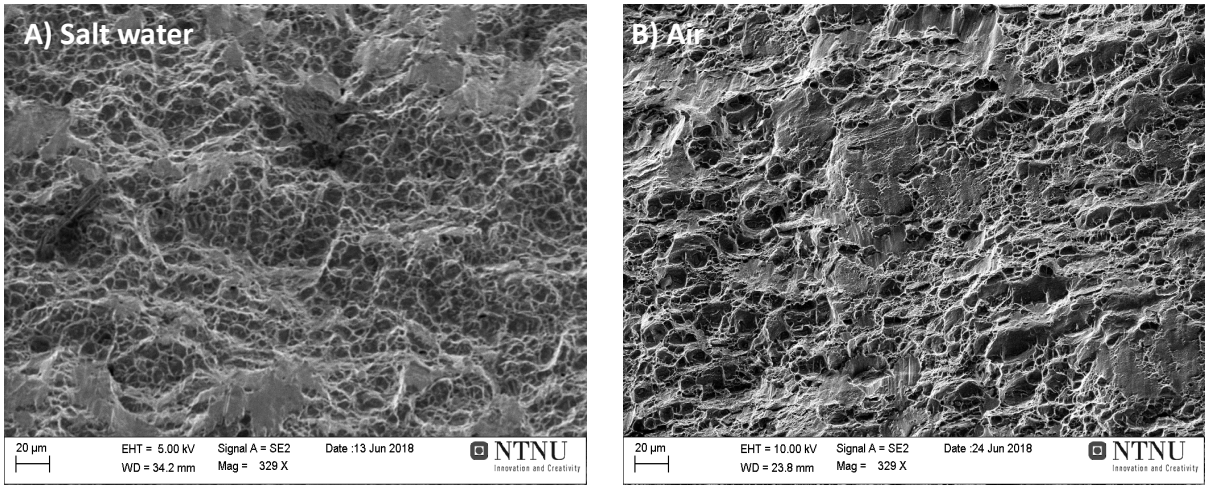

Figure 70: Final fracture appearance for samples tested in salt water (A) and in air (B).

Localized corrosion attacks

On several of the samples tested in the 5 wt% NaCl solution, localized corrosion sites were found on the fracture surface, as presented in figure 71. This may be due to salt water entering the crack tip or alternatively due to the samples being left in the salt water and not

immediately removed after the machine used for fatigue testing had stopped. This corrosion form is likely crystallographic etching, which refers to the selective dissolution of crystallographic planes. [63]

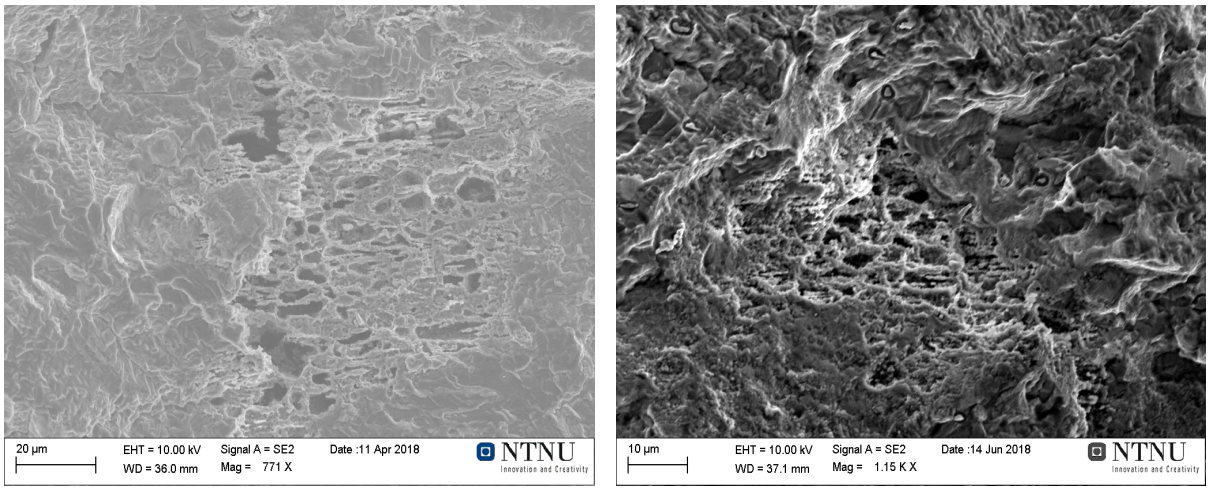

Figure 71: Localized corrosion sites found on the fracture surface found for some of the samples tested in the salt solution.

4.9.2 T7 AGED SAMPLES

For the T7 aged samples, no difference in the crack initiation mechanism was found compared to the T6 aged samples. Below, an example of the proposed mechanism of oxide film rupture and selective attack of surface slip bands is presented. In figure 72, a microcrack is observed on the extruded surface, while figure 73 shows the suspected crack initiation site on the fracture surface, where slip bands also are observed.

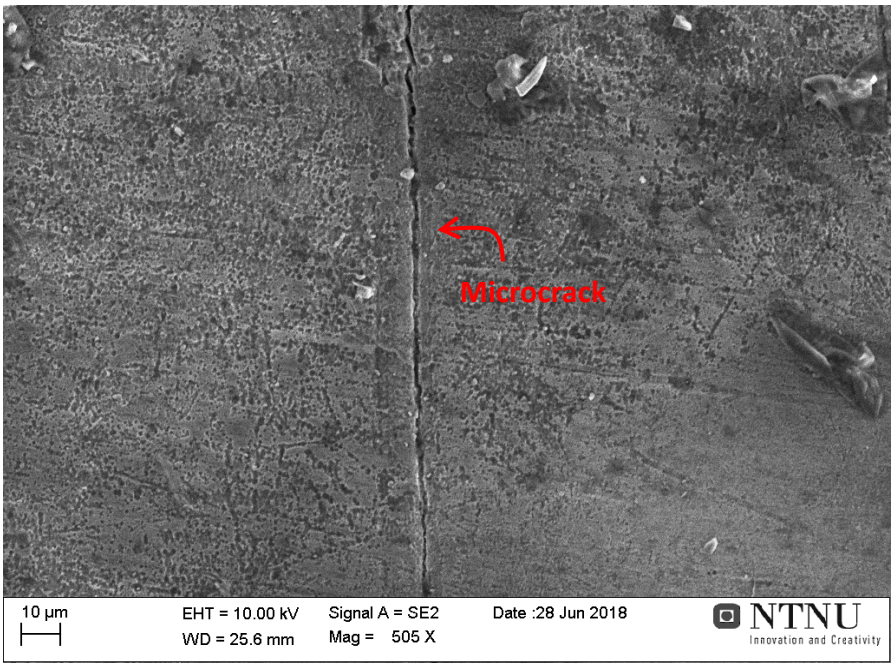

Figure 72: Illustration of large microcrack found for T7 tempered sample.

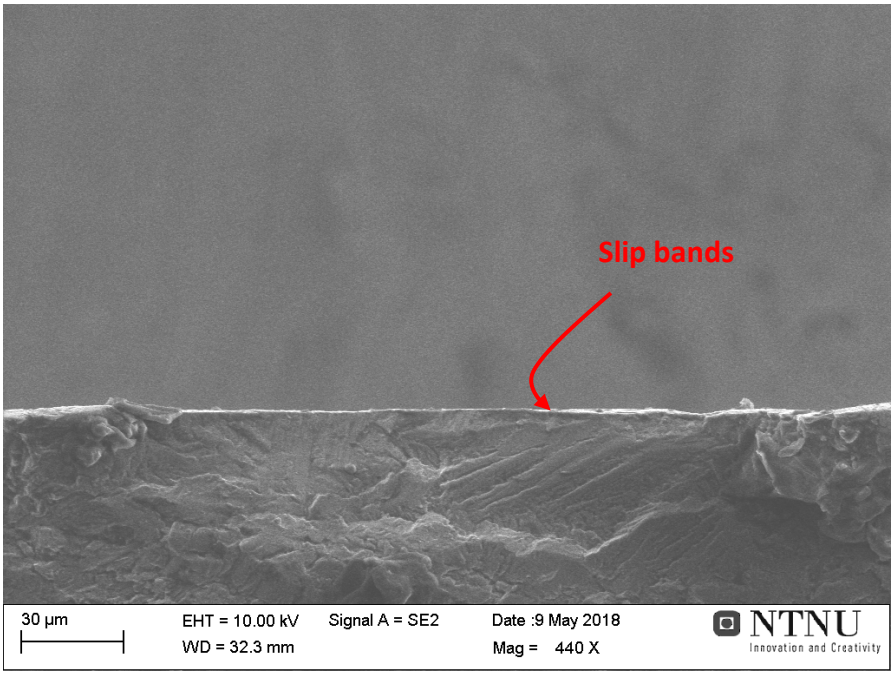

Figure 73: Magnification of crack initiation site for T7 tempered sample.

4.9.3 PRE-CORRODED SAMPLES

In this section, fractographs of samples pre-corroded for various times will be presented. An overview of the fracture surface, which is representative for the samples pre-corroded for more than 5 hours (i.e. 7 days, 21 days and 26 days) and samples pre-corroded for 5 hours, is presented in figure 74 and 75, respectively. The fractographs presented to represent long time exposure is from a sample that was exposed for 21 days. A clear difference can be seen, where multiple “valleys” can be found on both sides of the cross section, thought to be crack initiation sites. The area of valleys have been marked red in figure 74. Due to the significantly larger fatigue crack area found on the left side, this is likely the area of critical fatigue crack initiation. For the sample pre-corroded for 5 hours, figure 75, the “valley” feature is not found.

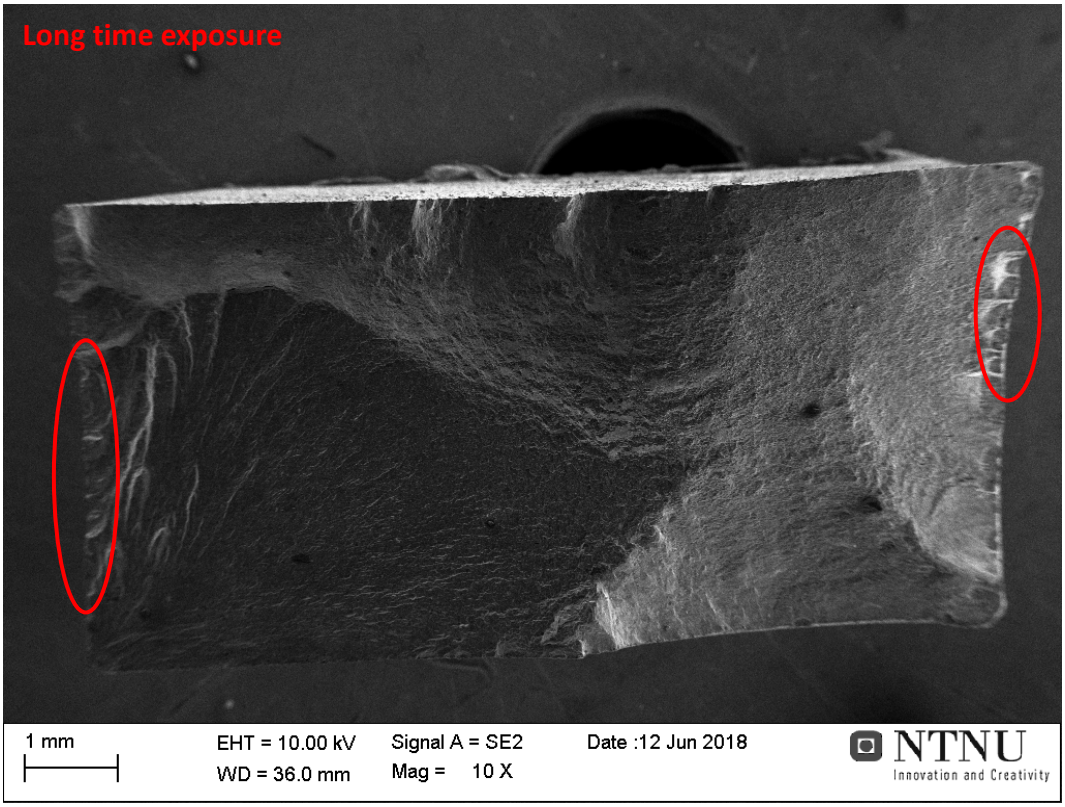

Figure 74: Overview of fracture surface for samples pre-corroded in salt water for long times (more than 5 hours).

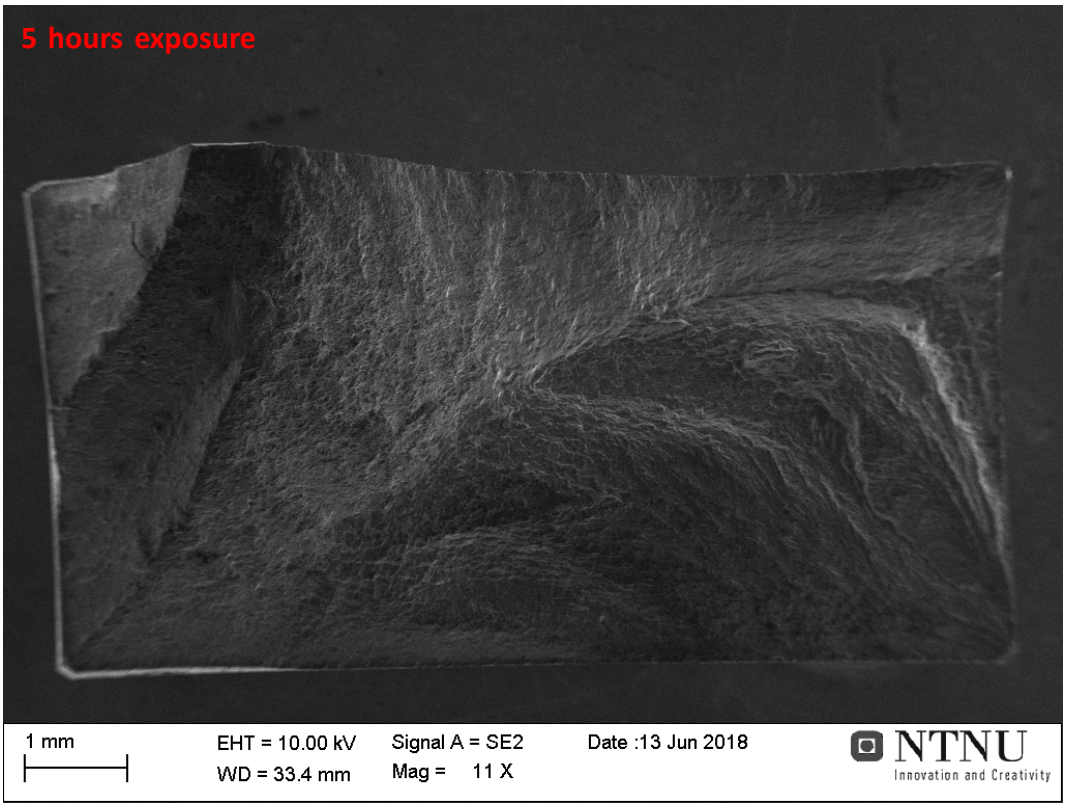

Figure 75: Overview of fracture surface for samples pre-corroded in salt water for 5 hours.

A higher magnification micrograph of the “valley”-like morphology is presented in figure 76. Here, it can clearly be seen that the “valley”-like morphology is in fact corrosion pits. The pit is approximately 20 μm deep and 50 μm wide. Corrosion pits are thought to be the crack initiation site for these samples, with the corrosion pits acting as stress concentrators. From the pit presented, river lines are found emanating from the initiation site. Note that the large corrosion pits acting as crack nucleus are found on the machined sides. This corresponds with the findings in section 4.7.4, where the pit population and size were much larger for the machined sides than the extruded sides. For the samples exposed for 5 hours, the crack initiation mechanism is thought to be similar to the un-corroded samples tested in air, i.e. fatigue crack initiation at the corner. This is supported by the presence of river lines found close to the corner, figure 77.

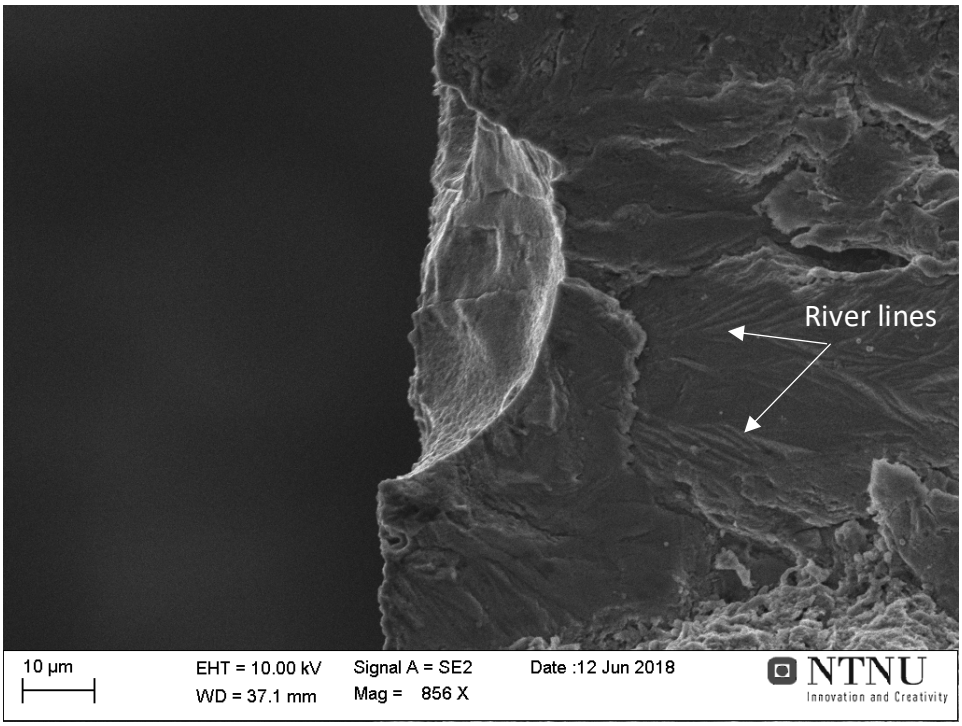

Figure 76: Crack initiation mechanism for samples pre-corroded for long times.

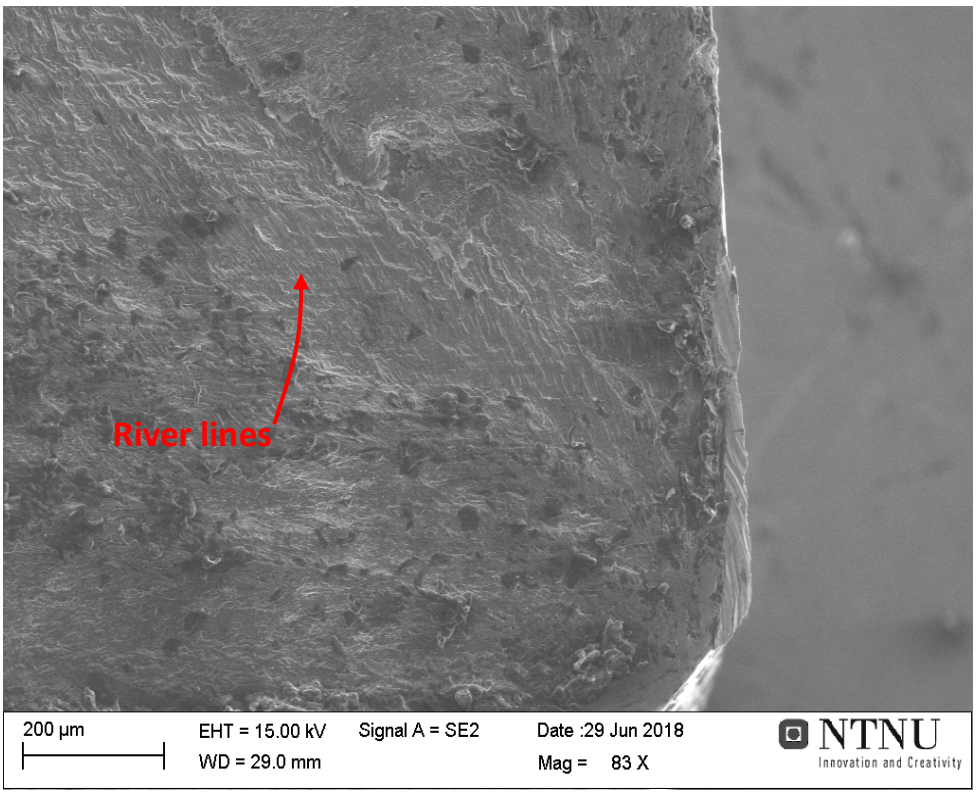

Figure 77: Crack initiation at corner for samples pre-corroded for 5 hours.

Temperature and humidity

The temperature and humidity of the room used for fatigue testing was monitored regularly to check its stability during testing. These measurements were done with *USB Temperature and Humidity Data Logger*, where the temperature and humidity is logged with a specified time interval. The average temperature and humidity from the measurements are presented in table 16, with corresponding standard deviations. As can be seen by the standard deviations, the temperature and humidity were stable during testing, and is therefore not thought to have affected the results significantly.

Table 16: Temperature and humidity measurements.

Temperature [°C]	Humidity [%RH]
24.5 ± 0.54	20.34 ± 4.16

5. Discussion

In this chapter the experimental results will be discussed with basis in established theory and research. First, a discussion will be carried out with focus on the die line influence on the corrosion fatigue behavior of this alloy. Then, microstructural effects which may have influenced the fatigue life will be presented and discussed. Finally, the results from the fatigue testing will be discussed in more detail.

The aim of this work was to characterize the corrosion fatigue properties of a 7046 alloy provided by Benteler, and compare it to fatigue results in laboratory air obtained by SINTEF. To establish the corrosion fatigue properties, fatigue tests were performed on samples submerged in a 5 wt% NaCl solution and pre-corroded samples tested in laboratory air.

5.1 The effect of surface roughness

As fatigue cracks usually initiate at the surface, the surface state is of high importance when it comes to fatigue life. For fatigue testing in air, it is well known that smooth surfaces generally perform better than rough surfaces. How this relation applies to corrosion fatigue is however less explored. Work by Leon and Aghion[64] on an AlSi10Mg alloy and Lindstad[65] on a 6082 alloy suggests that the reduction in lifetime between smooth and rough surfaces are larger in air than in a corrosive solution. In other words, it is tempting to say that the role of surface roughness, which is a very important parameter in “regular” fatigue, is less important during corrosion fatigue testing. Instead, the interaction between the stress and the corrosive environment is likely to govern the fatigue life. For the profile investigated in this work, the dominating surface roughness effect originates from the die lines. These die lines may vary in severity across the extruded surface, as well as along

different walls for a multi-walled extrudate, as investigated in section 4.4. In this work, no differences in surface roughness was found between the different walls.

To understand the extent of the die line surface roughness, scans were performed both parallel and perpendicular to the extrusion direction. These scans revealed relatively higher surface roughness values for scans performed perpendicularly to ED compared to scans performed parallel to ED, which is to be expected. The investigation of the material texture presented in section 4.3 revealed that the material had a weak texture, and it is therefore reasonable to believe that any differences in lifetime between samples taken parallel and perpendicular to the extrusion direction mainly is caused by the die line surface roughness. Nanninga[31], who tested the effect of the die line surface roughness for a weak textured 6082 alloy, found a significant reduction in lifetime when samples were tested perpendicular to the extrusion direction, as cracks were found to nucleate at the die lines. Nanninga also performed fatigue testing in a 5 wt% NaCl on the same alloy, and found no difference in lifetime between samples taken parallel and perpendicular to the extrusion direction, i.e. the effect of the die line surface roughness was negligible when testing in salt solution. In relation to the work performed in this thesis, the surface roughness values found were smaller than those obtained by Nanninga, and the sampling direction is therefore not thought to be an influencing factor for the corrosion fatigue results obtained in this work. It is however possible that differences would be found if samples were tested to complete failure, where differences in crack propagation rate due to differences in grain orientation relative to the applied load may impact the results.

5.2 Microstructural effects on corrosion fatigue

As briefly mentioned in theory section 2.5.3, Pedersen[66] have proposed that small differences in electrochemical potential between recrystallized and unrecrystallized grains may cause galvanic corrosion and consequently easier crack initiation. The material studied in this thesis had a mixed microstructure consisting of a fibrous core and a recrystallized layer of ~20 μm at the surface, i.e. Pedersen´s theory is applicable. In this work however, no measurements were done on the electrochemical potential difference between the recrystallized and fibrous grains. It should also be noted that not much is found on this potential crack initiation mechanism in other literature.

The main type of corrosion mechanism for both T6 and T7 tested samples was pitting corrosion. For the pre-corroded samples, corrosion pits were in addition suspected to be the crack initiation site. Based on the work of Ye et al. [35], it is reasonable to believe that coarse precipitates are dominant for this alloy in both temper states, as pitting corrosion have been found to be favored for alloys with coarse precipitates. In addition, the size and distribution of the intermetallic particles play a crucial role in corrosion fatigue of this alloy, as corrosion pits were found to nucleate around them. When the size and distribution of the intermetallic particles were examined, a slightly higher particle density was found for the longitudinal plane.

Interestingly, the pit size and population were also found to be clearly higher for the machined surfaces compared to the extruded surfaces. For the fatigue testing samples, the longitudinal plane is exposed to the solution at the machined sides and the extrusion plane is exposed to the solution at the extruded surfaces. It may therefore be tempting to believe that the measured higher particle density in the longitudinal plane is a contributing factor to the higher pitting susceptibility for the machined sides.

That the particle density really is higher for the longitudinal plane is however questionable. The observed difference in particle density is likely caused by particles in the extrusion plane being too small for detection at the given magnitude (250X), as a result of the large deformations in the extrusion process which shatters and fragmentates particles in the surface region, effectively reducing their size. The longitudinal plane, which is part of the "bulk" during extrusion, is not exposed to this. Due to this, the particle density may in reality be higher for the extrusion plane relative to the longitudinal plane, while the mean particle size realistically is smaller for the extrusion plane than what was measured. Another factor that may have influenced the increased pitting susceptibility of the machined sides is particle clustering. As can be seen by the figure 32 and 33, the longitudinal plane showed a tendency of particle clustering. Work done by Liao, Olive et al. [67] and Ilevbare et al. [68] have shown that particle clustering in AA2024-T3 and AA7075-T6 alloys leads to large stable pits.

5.3 Samples fatigue tested in 5 wt% NaCl

This part of the discussion will focus on the samples that were fatigue tested in 5 wt% NaCl. First, the potential crack initiation mechanisms will be discussed in more detail. Then, differences in the crack propagation stage will be discussed based on the fractographic results. Finally, the effect of temper state (i.e. T6 vs T7) will be discussed.

5.3.1 Crack initiation mechanisms

From the results it is apparent that the combination of corrosion and fatigue have a detrimental effect on fatigue life. This was apparent at all tested stress amplitudes. Compared to samples tested in air, a reduction in fatigue strength of 32.4% was found at 10^5 cycles. What concerns pre-corrosion, no difference in lifetime was found until long exposure times.

Therefore, a discussion will be carried out on the potential crack initiation mechanisms. As no lifetime difference was found between 5 hours pre-corrosion and regular, uncorroded samples tested in air, the corrosion attacks resulting from un-loaded submersion in the salt solution for 5 hours are evidently too small to influence the fatigue life of the material. When the sample surface of a specimen held unloaded in the salt solution for 6 hours were investigated in section 4.7.1 (thought to be representative for 5 hours submersion as well), the type of corrosion attack was clearly pitting. Interestingly, no clear difference in pit size and density was found between a loaded and unloaded sample exposed to the salt solution for the same time, suggesting that pitting is not especially accelerated during fatigue loading.

The maximum pit size for samples fatigue tested in the salt solution for the longest times were found to be ~4.3 µm, as presented in section 4.7.1. In the literature, where crack initiation has been attributed corrosion pits, Genel[20] reported of a reduced lifetime with a pit diameter of 6-12 µm, i.e. larger pits than those reported here. Another important aspect is the pit depth. Several authors, Sankaran et al. [69], DuQuesnay et al. [70] and Genel [20] have proposed that pit depth is the most important parameter when it comes to crack initiation at corrosion pits. In this work it was attempted to measure the pit depth by light microscopy and a micrometer screw, but it did not yield reliable results. However, the pit shown in figure 63 is only about 2-3 µm deep, observed for one of the samples that were fatigue tested for the longest times in the salt solution. This is not much compared to the work of Genel[20], where the pits with a diameter of 6-12 µm had a depth of 15-20 µm.

In addition, the pit geometry was hemispherical, which can be seen by figure 63 and 76. Duquette and Uhlig [71] proposes that the stress concentration at hemispherical pits is not large, which is another indication that crack initiation at corrosion pits were not a dominating site for crack initiation for samples tested in salt water. Another type of localized corrosion attack found was grain boundary corrosion, which was also proposed as a crack initiation mechanism. The extent of grain boundary attacks was however small compared to pitting corrosion, as is evident from the free surface examinations in section 4.7, and it is consequently unlikely that this mechanism was the dominant crack initiation mechanism.

The final proposed mechanism of crack initiation is preferential attack of surface slip bands due to rupture of the oxide film. This is thought to be the dominating crack initiation mechanism for several reasons. Firstly, it is likely that a mechanism clearly influenced by the combination of stress and corrosion dominates, as the effect of pre-corrosion was found to be much smaller than the synergic effect of corrosion and fatigue. With regards to pitting- and grain boundary corrosion, it was not possible to see any distinct difference on the extent of corrosion attacks between pre-corroded samples and samples tested in salt water. Secondly, of the examined samples, the majority of fatigue cracks seemed to originate from this mechanism.

Lin and Yang[34] have suggested that the crack initiation mechanism is a function of the applied stress, and that the dominating crack initiation mechanism at high stress amplitudes is due to oxide film rupture while it at lower stress amplitudes (with an increased exposure time to the salt solution) is caused by pitting. In this work, it was not possible to identify such a trend. A possible explanation for this relates to the exposure time. In the work of Lin and Yang[34], the fatigue lifetime approached 10^6 cycles, corresponding to ~14 hours exposure(the testing frequency was 20 Hz). In this work, the samples tested at the lowest stress amplitude of 160 MPa endured on average $8.3*10^4$ cycles, corresponding to an exposure time of ~4.5 hours. As no tests were conducted in salt water for up to 14 hours, it is not possible to draw any conclusions on this matter.

As fatigue cracking seemed to be dominated by a result of oxide film rupture, variables such as strain rate and re-passivation rate are important. In general, it is to be expected that a high strain rate combined with a low re-passivation rate will be the most detrimental for fatigue life. In the present study, even though the strain rate is unknown, it is thought to be constant at a constant stress amplitude and frequency. As already mentioned, it was not possible to identify any difference in crack initiation mechanism dependent on stress amplitude (or strain rate). The re-passivation rate will be dependent on alloy composition and solution chemistry. In this work, all tested samples came from the same extruded

profile, and the alloy composition is therefore not thought to be different for the various samples. The same solution, i.e. a 5 wt% NaCl solution was used for all tests. The solution was however made in several batches, meaning that some variation in the NaCl concentration is inevitable. These variations are however small, and it is unlikely that they have influenced the results.

For the regular samples tested in air (performed by SINTEF), it is proposed that fatigue cracks initiated at the corner separating the extruded and machined surfaces. The samples received no further treatment following machining, i.e. no rounding of corners or similar which could have forced crack initiation to occur elsewhere.

5.3.2 Crack propagation differences between 5 wt% NaCl and air

For Al alloys, It is well known that hydrogen can influence the fatigue properties in a corrosive environment, especially in the fatigue crack propagation stage, where the hydrogen is produced by the reaction of water vapor with the freshly formed fracture surface. [34] Evidence of such a mechanism was also found in this work, where a clear difference was found with regards to the striation morphology. While the striations of the air tested samples were featureless, the samples tested in salt water had a roughened appearance, suggesting an embrittlement mechanism. Although not studied in this work, hydrogen embrittlement has also been proposed to account for an increased fatigue crack growth rate in a corrosive environment. Therefore, a faster fatigue crack growth rate may also contribute to a more reduced lifetime in a corrosive environment compared to air. For this study however, the difference in lifetime is mainly caused by a faster crack initiation in the corrosive medium, as fatigue tests were stopped shortly after crack initiation to preserve the fracture surface. Interestingly, no difference was found in the final fracture appearance for samples tested in salt water and air, suggesting that the embrittlement is less prominent

in the final stages of fatigue. Something similar was observed by Zuo-Yan Ye et al. [35], who reported of brittle striations close to the crack initiation site and ductile striations further away. A possible explanation for this is that the mass transfer rate is only large enough to influence the area close to the crack tip, and not the area further away.

5.3.3 Effect of temper state

No difference in lifetime was found between T6 and T7 tempered samples tested in the salt solution. The same observation was made when T6 and T7 tempered samples were tested in air, which was presented in figure 40. As the main crack mechanism is thought to be caused by preferential attacks of surface slip bands, the slip character will be a factor. For T6 aged samples, there will be an increased tendency of slip localization compared to T7 aged samples [72], which however did not seem to influence the time needed for crack initiation. Duquette and Chen[44] reported of a more rapid pit growth rate at longer aging times for an Al-Li-Zr alloy while Ye et al. [35] reported of increased pitting susceptibility with coarse matrix precipitates. The T7 aged specimens will have coarser precipitates than the T6 aged samples due to the increased heat treatment. In this work, no distinct difference in pit size and density could be found between the peak aged and overaged samples, suggesting that the effect of the two aforementioned observations were negligible.

A possible reason for the similar corrosion fatigue behavior of T6 and T7 aged samples is based on the degree of overaging. In this work, the heat treatment performed to achieve overaging condition consisted of heating from 30 °C to 90 °C in 25 minutes, and subsequent cooling from 90 °C to 50 °C in 11 minutes on T6 aged samples. In the work of Lin and Yang[34], where more severe pitting was found for T7 aged samples compared to T6 aged samples, the samples were heat-treated at 160 °C for 30 hours from T6 temper in order to achieve T7 condition. With such a large difference in heat treatment, it is likely that the T7 aged specimens in the work of Lin and Yang[34] contained relatively coarser matrix

precipitates compared to T6 condition than the difference in coarseness between T7 and T6 condition in this work. To investigate this, TEM would be needed. This theory is supported by comparing the mechanical properties in this work and in the work of Lin and Yang. In this work, the T6 aged samples had a ~6.4% higher yield strength and ~3% higher ultimate tensile strength, whereas the T6 aged specimens in the work of Lin and Yang [34] had a ~7.3% higher yield strength and a 10% higher ultimate tensile strength, i.e. the degree of overaging in the work of Lin and Yang is clearly higher. Based on this, it is possible that a longer overaging treatment would yield more significant differences in pit size and density. If such a heat treatment is enough to make the pits in the T7 temper a dominating crack initiation site is however inconclusive.

5.4 Pre corroded samples

As presented in section 4.7.4, differences in pit size and density between the machined and extruded surfaces were apparent. Differences in intermetallic particle size and density, as well as clustering, may have contributed to a difference in pit size and density between the extruded and machined surfaces. However, it is doubtful that these mechanisms are enough to cause such a large difference as was observed. The main reason for the increased pitting susceptibility of the machined sides is thought to be a result of a thicker oxide film for the extruded surfaces. The extruded surfaces have gone through high temperature operations as extrusion and solution heat treatment (480 °C) that likely have led to an increase in the oxide film thickness. The machining of the samples removes the thermal oxide for the machined sides, and no further high temperature operations are performed after solution heat treatment.

A similar observation of a thicker oxide film for the extruded surfaces have been reported by Kumari et al.[73], where a 9 nm thick γ-Al_2O_3/spinel $AlMg_2O_4$ surface film was observed on the extruded surfaces of an AA6005 alloy. Kumari et al. studied the susceptibility to IGC and found that the IGC susceptibility was much lower for the extruded surfaces. The IGC

attacks started around primary intermetallic particles, just as the pitting attacks in this thesis.

The observation of a larger pit size for the machined surfaces was also visible from the fractographic examinations presented in section 4.9. Here, a large pit of diameter 50 μm and depth 20 μm could be observed on the machined surface, for a sample pre-corroded in the 5 wt% NaCl solution for 21 days. Compared to the pit size of the samples fatigue tested in the 5 wt% NaCl solution, with a maximum diameter of ~4.3 μm and a depth of 2-3 μm, this is a significant difference. The pit shape was clearly hemispherical, as seen by figure 76, but unlike the samples fatigue tested in the 5 wt% NaCl solution, it is thought that the pit size is sufficiently large to act as a crack nucleation site. The potential of the corrosion pits for acting as crack initiation sites is also related to the stress amplitude, and with a higher stress amplitude, the driving force for crack initiation is increased. Therefore, the reduction in lifetime could be larger for higher stress amplitudes.

For the samples pre-corroded for 5 hours, the pits are too small to function as a crack initiation site. With an absence of the combined effect of corrosion and fatigue and possible surface film rupture, the samples likely failed in the same manner as the un-corroded samples tested in air, i.e. due to stress concentration at the sharp corner separating the machined and extruded surfaces.

5.5 Comparison to 6082

The average lifetime found by Lindstad at a maximum stress (σ_{max}) of 220 MPa with an R value of 0.1 was $1.44*10^5$ cycles. The stress amplitude corresponding to R = -1, derived by the Goodman relation, is σ_a = 145 MPa. In this work, no fatigue tests were performed with a stress amplitude of σ_a = 145 MPa. Therefore, the linear approximation obtained (R^2 = 0.8) through the fatigue results was used to get an indication of the lifetime at σ_a = 145 MPa. This investigation revealed a predicted lifetime of $1.36*10^5$ cycles. How useful these results are, relying heavily on approximations in order to make a comparison, is debatable. However, with knowledge of the models used for approximating the results, an interpretation can be made. The work of Dowling[42] states that the Goodman relation is conservative, i.e. the experimental results are likely to outperform those predicted by the Goodman relation. Therefore, the predicted lifetime at a stress amplitude $\boldsymbol{\sigma_a}$ = 145 MPa, predicted by the Goodman relation, is likely lower than the actual lifetime. Based on these findings, it is tempting to suggest that 6082 performed better in the 5 wt% NaCl solution than 7046, even though the 7046 alloy is expected to perform better in regular fatigue. This is likely related to the better general corrosion resistance of 6082 compared to 7046. A better way of comparing the corrosion fatigue properties is to compare the reduction in lifetime compared to air. Work done by Corsetti and Duquette on a 7075 alloy [74] suggests that the reduction in fatigue life remains approximately constant for all mean stresses, i.e. the reduction in lifetime for R=-1 and R=0.1 is similar. In the work of Lindstad[65], the fatigue testing in air and in the 5 wt% NaCl solution was performed at different R values, and Lindstad used another approximative method (Smith- Watson-Topper) to compare the results from air and 5 wt% NaCl. Introducing another approximative method would be too ambiguous, and a comparison of lifetime in 5 wt% NaCl/air for 7046 and 6082 is therefore not presented.

5.6 Practical implications of current work

Given the large reduction in lifetime found for the 7046 alloy when tested in 5 wt% NaCl, it is clear that some measures should be taken if the alloy is to be used in automotive parts exposed to a corrosive environment. Certainly, automotive parts are not submerged in salt water as was tested in this thesis, but the results do still provide information on the applicability of the alloy. Although not directly related to corrosion, an obvious measure would be to reduce vibrations and stress fluctuations, but this is likely already accounted for when components are designed. Measures on improving the corrosion resistance should therefore be taken. By avoiding stagnant regions, the pitting susceptibility will be reduced, as fluid flow will increase the probability of removing the aggressive environment inside the pits. Other suggestions that will increase the corrosion protection is to apply surface coatings or to use inhibitors, which are probably more effective due to the proposed mechanism of oxide film rupture.

5.7 Final remarks

During laboratory work, error sources are inevitable. In this section, possible error sources will be discussed.

In an industrial context, it is important to be able to predict the fatigue life with a small probability of failure. Fatigue is a statistical quantity, and a high scatter is often observed in fatigue testing, implying that more samples should be tested at each stress amplitude than what was done in this work.

For the samples tested in the 5 wt% NaCl solution, it is possible that the chamber may have influenced the results. This is however unlikely, as samples fatigue tested in the chamber in air (without salt water) revealed no difference in lifetime compared to the work of SINTEF.

The grips used to fasten the samples is made of steel (see figure 27 for reference). Therefore, it is possible that the galvanic effect due to contact between the grips and the samples may have influenced the results.

Lastly, all fatigue samples were manually inserted into the testing machine, and some misalignment causing an uneven stress distribution is therefore possible.

6 CONCLUSION

The corrosion fatigue properties of an extruded 7046 alloy have been investigated. The alloy was tested in fully reversed cycling, i.e. R=-1, at a frequency of 5 Hz. All samples were tested in the direction parallel to the extrusion direction. The work consisted mainly of T6 tempered samples fatigue tested in a 5 wt% NaCl solution or samples pre-corroded in the same solution for various times and subsequently tested in laboratory air. In addition, T7 tempered samples were tested in the 5 wt% NaCl solution to investigate if any differences in fatigue life could be found compared to the T6 temper. To obtain an indication of the extent of corrosion attacks, the extruded surfaces of un-corroded samples tested in air, samples fatigue tested in the salt solution and samples pre-corroded and subsequently tested in air were investigated in SEM. For the pre-corroded samples, the machined surfaces were also examined. Fractographic examinations were done on all the aforementioned sample types to better understand how the corrosive medium affects the samples.

- A significant reduction in lifetime was found at all stress amplitudes for the samples fatigue tested in the 5 wt% NaCl solution compared to laboratory air, with a reduction in fatigue strength of 32.4% at 10^5 cycles. When the fracture surfaces were examined, clear indications on the corrosive medium was found. Given the large loss of strength, it is advised that measures are taken to improve the corrosion resistance of the alloy, for example by the use of coatings/inhibitors.
- For pre-corroded samples, no difference in lifetime was found for a pre-corrosion time of 5 hours, indicating that the synergic effect of corrosion and fatigue is far more detrimental to fatigue life. When samples were pre-corroded for longer times (1 week, 3 weeks and 26 days), clear reductions in lifetime were found.
- No difference in lifetime was found between T6 and T7 tempered samples tested in 5 wt% NaCl, suggesting that the initiation mechanism was the same for both temper states.

- The governing fatigue crack initiation mechanism for the samples fatigue tested in 5 wt% NaCl is thought to be a result of oxide film rupture and selective attacks on surface slip bands.
- For the samples pre-corroded for longer times (more than 5 hours), the proposed fatigue crack initiation mechanism is due to corrosion pits. The corrosion pits were found to be significantly larger for the machined surfaces, which is proposed to mainly be caused by a thinner oxide film on the machined surfaces.

Recommendations for further work include:

- Investigate protective measures (for example coatings) that can increase the lifetime of this alloy in corrosion fatigue.
- More extensive pre-corrosion testing in an attempt to determine critical pit size.
- TEM analysis of precipitates to determine their size and distribution, with emphasis on differences between T6 and T7 temper.
- Investigate the effect of more extensive over aging treatments.
- Measure oxide film thickness for extruded and machined surfaces.

7 REFERENCES

1. Miller, W.S., Zhuang, L, Bottema , A. J, De Smet, A., *Recent development in aluminium alloys for the automotive industry.* Materials Science and Engineering A, 2000: p. 37-49.
2. Clymer, F., *Henry's wonderful Model T 1908-1927*. 1955, Bonanza Books, New York.
3. Dwigth, J., *Aluminium design and construction.* Routledge, 1999.
4. Dieter, G.E., *Mechanical Metallurgy*

. 1988: McGraw-Hill Book Company.

5. Hydro. *Aluminium, environment and society*. 2012; Available from: http://www.hydro.com/globalassets/1-english/about-aluminium/files/aluminium_environment-and-society.pdf.
6. Davies, J.R., *Aluminum and Aluminum alloys.* ASM International, 1993.
7. Solberg, J.K., *Teknologiske Metaller og Legeringer*. 2014, NTNU.
8. ESAB. *Understanding the Aluminum Alloy Designation System*. 2017; Available from: http://www.esabna.com/us/en/education/blog/understanding-the-aluminum-alloy-designation-system.cfm.
9. Veium, K.F., *Effect of Cathodic Polarization on the Susceptibility to Hydrogen Embrittlement in 5xxx, 6xxx and 7xxx Series Aluminium Alloys*, in *DMSE*. 2015, NTNU.
10. Mondolfo, L.F., *Aluminium alloys: Structure and Properties*. 1976: Butterworth & Co, Ltd.
11. Doherty, R.D., Vasudevan, A. K., *Aluminium Alloys - Contemporary Research and Applications*. Vol. 31. 1989: Academic Press, Inc.
12. Robson, J.D., Prangnell, P. B., *Dispersoid precipitation and process modelling in zirconium containing commercial aluminium alloys.* Acta Materialia, 2001. **49**: p. 599-613.
13. Polmear, I., *Light Alloys*. 4 edition ed. 2006.
14. Reiso, O., *Extrusion of AlMgSi Alloys.* Materials Forum, 2004. **28**
15. Saha, P.K., *Aluminium Extrusion Technology*. 2000: ASM International.
16. Berg L K, G.J., Hansen V, Li X Z, *GP-Zones in Al-Zn-Mg alloys and their role in artificial aging.* Acta Materialia, 2001. **49**.
17. Davis, J.R., *Corrosion of Aluminum and Aluminum Alloys*. 1999, ASM International.
18. Nisancioglu, *"Pitting Corrosion." In: Corrosion and Corrosion Protection (compendium).* 2016, NTNU.
19. Frankel, G., *Pitting corrosion of metals - A review of the critical factors.* Journal of the electrochemical society, 1998.
20. Genel, K., *The effect of pitting on the bending fatigue performance of high-strength aluminum alloy.* Scripta Materialia, 2007. **57**.
21. Park, J., Paik, CH., Huang, YH., *Influence of Fe-rich intermetallic inclusions on pit initiation on aluminum alloys in Aerated NaCl.* Journal of Electrochemical Society, 1999. **146**.
22. Pao, P.S., Gill, S J., Feng, C R. , *On fatigue crack initiation from corrosion pits in 7075-T7351 Aluminium Alloy.* Scripta Materialia, 2000. **43**.

23. Hughes, E.A., Birbilis, N., Mol, J., *Recent Trends in Processing and Degradation of Aluminium Alloys*. High Strength Al-Alloys: Microstructure, Corrosion and Principles of Protection. 2011.
24. Langsrud, Y., *Korngrensepartikler*. 2017, Benteler.
25. Valor A, C.F., Alfonso L, Rivas D, Hallen J M, *Stochastic modelling of pitting corrosion: A new model for initiation and growth of multiple corrosion pits.* Corrosion Science, 2006. **49**.
26. P.E.J Flewitt, W.R.K., *Grain Boundaries - Their Microstructure and Chemistry.* John Wiley & Sons, 2001.
27. Nisancioglu, K., *Corrosion Caused by Grain Boundary Separation*. 2015, Corrosion and Corrosion Protection: Norwegian University of Science and Technology.
28. Vargel C, J.M., Schmidt M P, *Corrosion of Aluminium*. 2004, Elsevier.
29. Callister, W.D., Rethwisch, D.G, *Materials Science and Engineering*. 8 ed. SI Version. 2011: John Wiley & Sons.
30. Almar-Næss, A., *Utmatting og utmattingsprøving*. Metalliske materialer. 1981: Tapir Forlag. 179-200.
31. Nanninga, N.E., *High Cycle Fatigue of AA6082 and AA6063 Aluminium Extrusions*. 2008, Michigan Technological University.
32. Suresh, S., *Fatigue of materials*. 1991, Cambridge Solid State Science Series.
33. Srivatsan, T.S., Sudarshan, T. S., *Mechanisms of fatigue crack initiation in metals: role of aqueous environments.* Journal of Materials Science, 1988. **23**.
34. LIn Chih-Kuang, Y.S.-T., *Corrosion Fatigue Behaviour of 7050 Aluminium Alloys in Different Tempers.* Engineering Fracture Mechanics, 1998. **59**(6).
35. Zuo-Yan Ye, L.D.-X., Xiao-Hua Zhang, *Corrosion Fatigue Behaviour of 7A85 Aluminum Alloy Thic Plate in NaCl Solution.* Acta Materialia, 2015. **28**: p. 1047-1054.
36. Simnad, M.T.C., Evans, U.R., *Iron Steel Inst.* Vol. 156. 1947.
37. Anderson, T.L., *Fracture Mechanics - Fundamentals and Applications*. 2005, Taylor & Francis group.
38. Bardal, E., *Korrosjon og korrosjonsvern*. Vol. 2. 1994: Tapir.
39. Parkins, R.N., *«Corrosion Fatigue», proceedings of the first USSR-UK Seminar on Corrosion Fatigue of Metals.* The Metals Society, 1984.
40. Stoltz, R.E., Pelloux, R.M., *Metal Transactions.* 1972. **3A**.
41. Locke, J.S., *Comparison of Age-Hardenable Al Alloy Corrosion Fatigue Crack Growth Susceptibility and the Effect of Testing Environment.* Corrosion vol 72.
42. Dowling, N.E., *Mechanical Behavior of Materials*. Vol. Fourth edition. Pearson.
43. Courtney, T., *Mechanical Behaviour of Materials*. 2000, McGraw-Hill Higher Education.
44. Chen, G.S., Duquette, D. J.,, *Corrosion fatigue of a precipitation-hardened Al-Li-Zr alloy in a 0.5 M Sodium Chloride Solution.* Metallurgical Transactions, 1992.
45. Nanninga, N.E., White, C., Mills, O., Lukowski, J., *Effect of specimen orientation and extrusion welds on the fatigue life of an AA6063 alloy.* International Journal of Fatigue, 2009.
46. Feidenhans'l, A.N., *Comparison of Optical Methods for Surface Roughness Characterization.* Meas. Sci. Technol., 2015.
47. Ås, S., Skallerud, B., Tveiten, B., *Surface roughness characterization for fatigue life predictions using finite element analysis.* International Journal of Fatigue, 2008. **30**.

48. Ardi D. T., L.Y.G., Chan K.H.K, Blunt L., Bache M. R. , *Surface topography and the impact on fatigue performance.* Metrol. Prop., 2015. **3**.
49. Ås, S.K., *Fatigue life prediction of an aluminum alloy automotive component using finite element analysis of surface topography*, in *Department of Structural Engineering*. 2006, NTNU.
50. Wagner, L., *Mechanical surface treatments on titanium, aluminum and magnesium alloys.* Materials Science and Engineering A, 1999.
51. Pedersen, *The Effect of Grain Structure on Fatigue Life of Age Hardening Al Alloys*, in *4th E.C.F Conference*.
52. Pedersen K., J.O., Moe, Roven, *Fatigue fracture and microstructure relationship of an aluminium automobile component.* Fracture behaviour and design of materials and structures.
53. Hjelen, J., *Scanning elektron-mikroskopi*. 1989, Metallurgisk institutt, NTH.
54. https://www.fose1.plymouth.ac.uk/fatiguefracture/tutorials/FailureAnalysis/Fractography/Fractography_Resource4.htm. *Characteristics of fast fracture in metals*. 2017.
55. Stephens, R., Fatemi, A., Stephens, RR., Fuchs, H.O, *Metal Fatigue in Engineering*. Vol. 2. 2001: John Wiley & Sons.
56. Verlinden, B., *Thermo-Mechanical Processing of Metallic Materials*. Pergamon Materials Series. 2007, Elsevier.
57. *Chemical Composition Limits*. 2015, Aluminum Association.
58. Lindstad, G.T., *Corrosion Fatigue of Extruded AA6082 Aluminium Alloy*, in *IMA*. 2017, NTNU.
59. Jennings, B.R., Parslow, K., *Particle Size Measurement: The Equivalent Spherical Diameter.* Proceedings of the Royal Society of London, 1988. **419**: p. 137-149.
60. Ferreira, T., *ImageJ User Guide II.* 2012.
61. Starink, M.J., Wang, S.C., *A Model for the Yield Strength of Overaged Al-Zn-Mg-Cu Alloys.* Acta Materialia, 2003. **51**: p. 5131-5150.
62. Eivani, A.R., Ahmed, H., Zhou, J., Duszcyk, J. , *Correlation between Electrical Resistivity, Particle Dissolution, Precipitation of Dispersoids, and Recrystallization Behavior*
of AA7020 Aluminum Alloy. 2009.
63. Zhang, X., Zhou, X., Hashimoto, T., Liu, B., *Localized corrosion in AA2024-T351 aluminium alloy: Transition from intergranular corrosion to crystallographic pitting.* Materials Characterization, 2017. **130**.
64. Avi, L., Aghion, E., *Effect of surface roughness on corrosion fatigue performance of AlSi10Mg alloy produced by Selective Laser Melting (SLM).* Materials Characterization, 2017. **13**: p. 188-194.
65. Lindstad, G., *Corrosion Fatigue of Extruded AA6082 Aluminium Alloy*. 2017, NTNU.
66. Pedersen K, L.O., Helgeland O., *The effect of grain structure on fatigue life of age hardening aluminum alloys.* Fracture and the role of microstructure, 1982. **2**: p. 495-502.
67. Liao, C.M., Olive, J. M., *In-situ monitoring of pitting corrosion in aluminum alloy 2024.* Corrosion, 1999. **54**.

68. Ilevbare, G.O., Schneider, O., *In-situ confocal laser scanning microscopy of AA 2024-T3 corrosion metrology - localized corrosion of particles.* Journal of the Electrochemical Society, 2004. **151**.
69. Sankaran, K.K., Perez, R., Jata, K.V., *Effect of pitting corrosion on the fatigue behaviour of aluminium alloy 7075-T6: modelling and experimental studies.* Mater. Sci. Eng., 2001.
70. DuQuesnay, D.L., Underhill, P.R., Britt, H.J., *Fatigue crack growth from corrosion damage in 7075-T6511 aluminium alloy under aircraft loading.* International Journal of Fatigue, 2003.
71. Duquette, D.J., Uhlig, H. H., *Trans. ASM.* 1969. **62**.
72. Professor Roven, H.J., *Personal communication*. 2018.
73. Kumari, S., Wenner, S., Walmsley, J., Lunder, O., Nisancioglu, K., *Initiation and Propagation of Intergranular Corrosion on AA6005 Aluminium Alloy With Low Copper Content*, in *ASST 2018*. 2018.
74. Corsetti, L.V., Duquette, D J., *The Effect of Mean Stress and Environment on Corrosion Fatigue Behavior of 7075-T6 Aluminum.* Metallurgical Transactions, 1974. **5**.

APPENDIX A: FATIGUE RESULTS

All fatigue tests were done with the MTS810 100kN machine. Table 17-21 shows all the results from the fatigue testing, including the samples tested in air by SINTEF. Some samples were also mounted to the chamber and tested in air, to confirm that the chamber did not play any role in the reduced lifetime observed in the salt solution.

Chamber, 5 wt% NaCl

Table 17: Fatigue results for samples tested in 5 wt% NaCl.

Sample number	Temper state	Frequency [Hz]	R	Stress amplitude [MPa]	N_f (cycles)
1	T6	5	-1	160	53666
2	T6	5	-1	160	40847
3	T6	5	-1	160	113903
4	T6	5	-1	160	109905
5	T6	5	-1	160	109385
6	T6	5	-1	160	66541
7	T6	5	-1	160	127133
8	T6	5	-1	160	47518
9	T6	5	-1	220	36687
10	T6	5	-1	220	30883
11	T6	5	-1	220	28123
12	T6	5	-1	220	44350
13	T6	5	-1	220	40834
14	T6	5	-1	220	56088
15	T6	5	-1	260	12362
16	T6	5	-1	260	10404
17	T6	5	-1	260	13029
18	T6	5	-1	260	17069
19	T6	5	-1	260	16921
20	T6	5	-1	260	13563
21	T7	5	-1	160	70472
22	T7	5	-1	160	176831
23	T7	5	-1	160	114653
24	T7	5	-1	160	167592
25	T7	5	-1	160	117342

Chamber air

Table 18: Fatigue results for samples tested in the chamber in air.

Sample number	Temper state	Frequency [Hz]	R	Stress amplitude [MPa]	N_f (cycles)
1	T6	5	-1	220	70469
2	T6	5	-1	220	66793
3	T6	5	-1	220	65865

Pre-corroded samples

Table 19: Fatigue results for pre-corroded samples.

Sample number	Temper state	Frequency [Hz]	R	Stress amplitude [MPa]	N_f (cycles)	Pre-corrosion time
1	T6	5	-1	220	70469	5 hours
2	T6	5	-1	220	66793	5 hours
3	T6	5	-1	220	136752	5 hours
4	T6	5	-1	220	125732	5 hours
5	T6	5	-1	220	43119	1 week
6	T6	5	-1	220	43674	1 week
7	T6	5	-1	220	23878	3 weeks
8	T6	5	-1	220	42788	3 weeks
9	T6	5	-1	220	41731	3 weeks
10	T6	5	-1	220	23319	26 days

Fatigue testing performed by SINTEF

T6 condition

Table 20: Fatigue results obtained by SINTEF for T6 tempered samples.

Sample number	Temper state	Frequency	R	Stress amplitude [MPa]	N_f (cycles)
1	T6	10	-1	160	Run out
2	T6	10	-1	160	Run out
3	T6	10	-1	160	986554
4	T6	10	-1	160	1388178
5	T6	10	-1	220	123378
6	T6	10	-1	220	82897
7	T6	10	-1	220	61225
8	T6	10	-1	220	95637
9	T6	10	-1	220	82168
10	T6	10	-1	260	26381
11	T6	10	-1	260	24948
12	T6	10	-1	260	24496
13	T6	10	-1	260	40623

T7 condition

Table 21: Fatigue results obtained by SINTEF on T7 tempered samples.

Sample number	Temper state	Frequency	R	Stress amplitude [MPa]	N_f (cycles)
1	T7	10	-1	160	Run out
2	T7	10	-1	220	113849
3	T7	10	-1	220	81378
4	T7	10	-1	220	76397
5	T7	10	-1	220	84047
6	T7	10	-1	260	31201
7	T7	10	-1	260	31268
8	T7	10	-1	260	40908
9	T7	10	-1	260	40333

APPENDIX B: EDS RESULTS

Figure 78-81 displays the scanned particles and areas in the 7046 extruded sample. Table 22 presents the results of the scans in normalized at %.

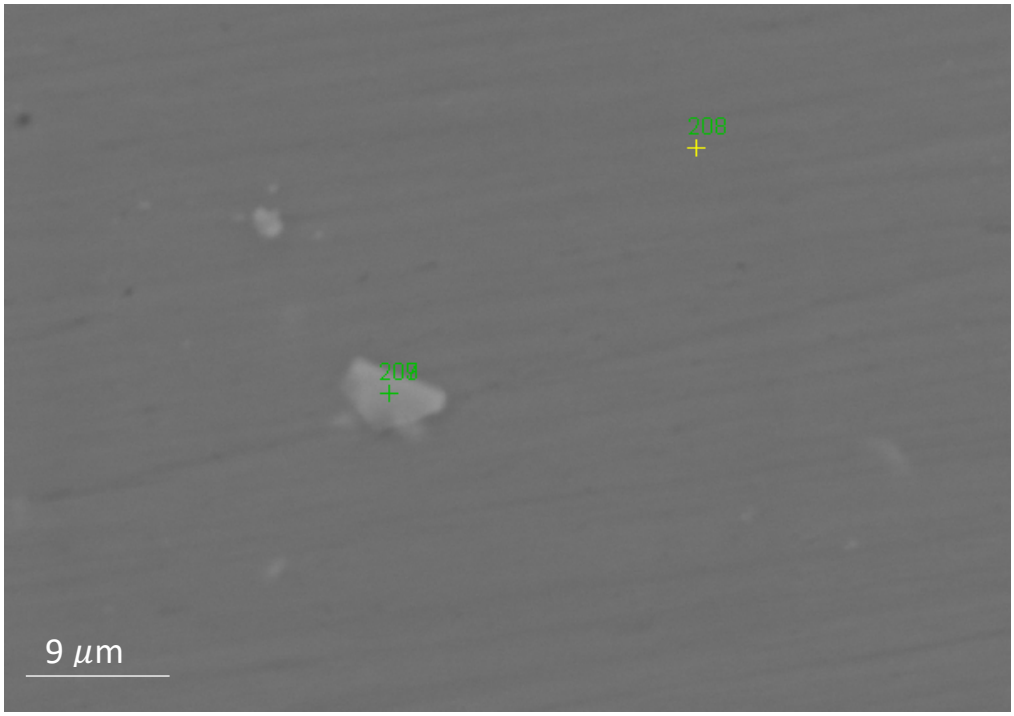

Figure 78: Scanned area of 7046 alloy.

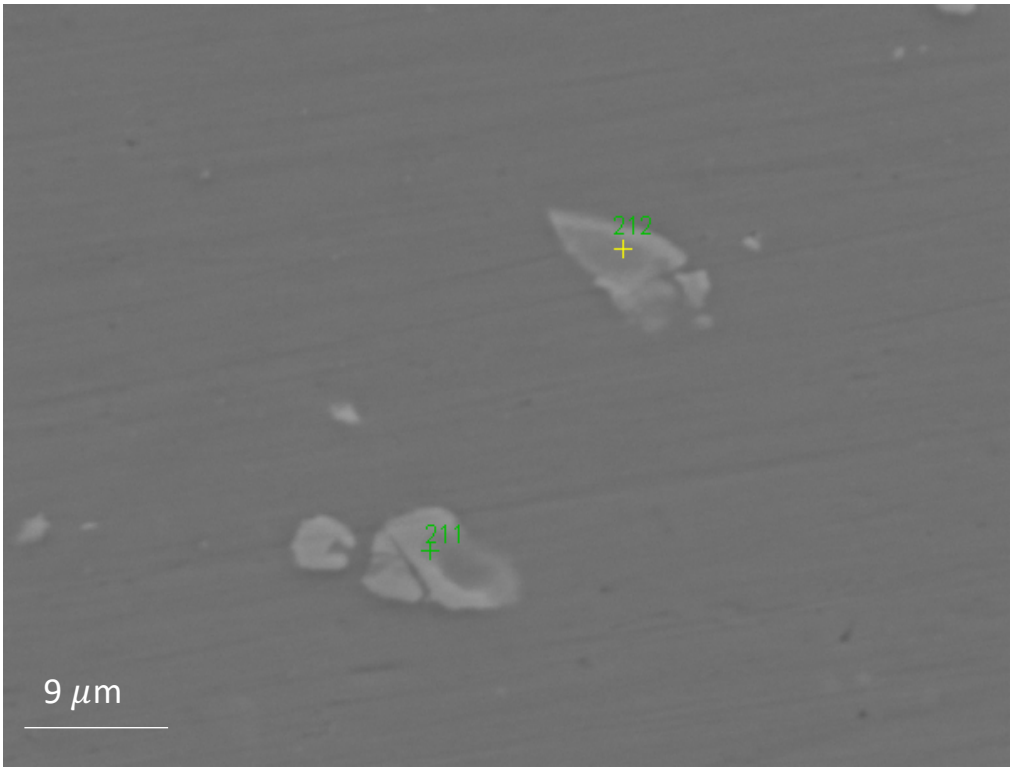

Figure 79: Scanned area of 7046 alloy.

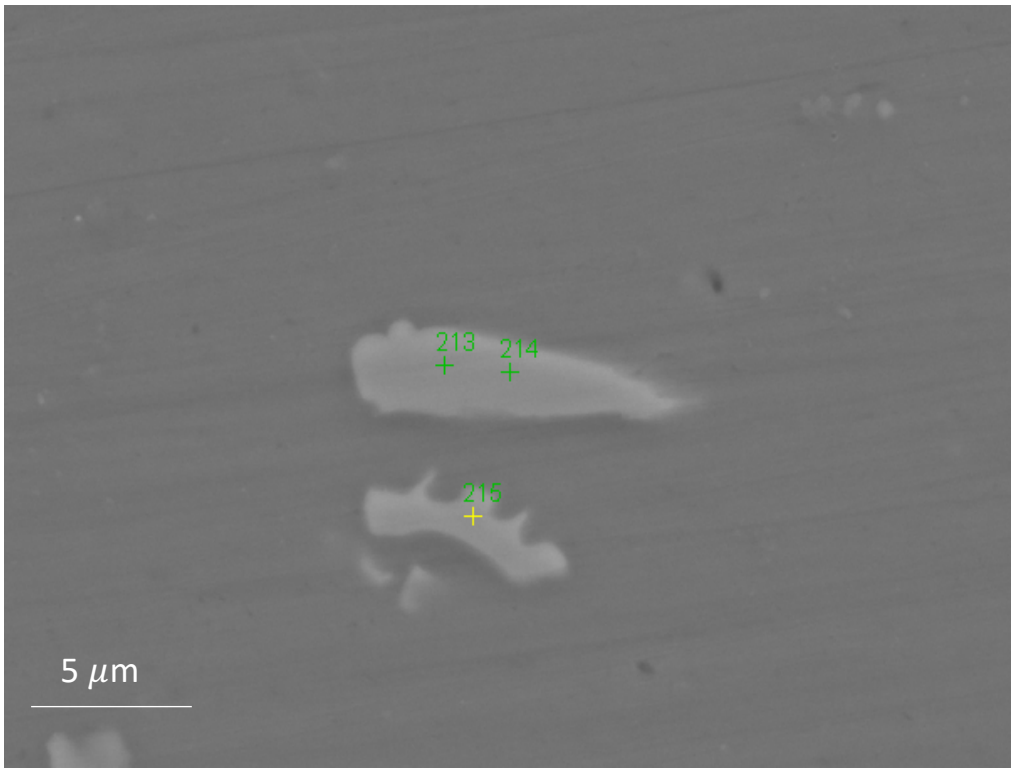

Figure 80: Scanned area of 7046 alloy.

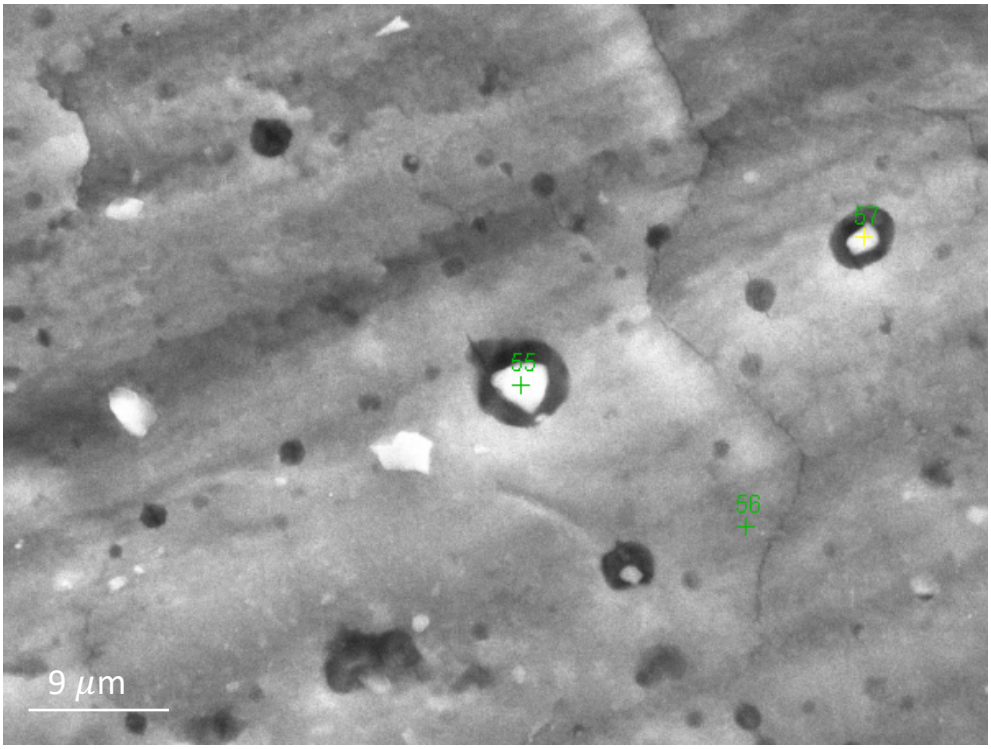

Figure 81: Scanned area of 7046 alloy.

Table 22: Results from EDS scans.

Element [%at]	208	209	211	212	213	214	55	57
Al	95	74.8	79.61	74.79	73.05	72.89	86.07	87.64
Fe	0	14.47	10.58	16.68	16.11	16.45	5.38	4.21
Si	0.31	4.1	3.86	6.19	4.33	4.46	3.51	3.12
Mn	0	0.42	0.33	0.3	0.45	0.44	0.25	0.19
Ni	0.41	0.29	0.1	0.55	0.23	0.19	0	0
Cu	0	2.11	1.04	0.1	2.2	2.16	0.66	0.56
Zn	2.09	1.88	2.38	0.54	1.86	1.7	1.67	1.7
Zr	0.23	0.32	0.29	0.12	0.31	0.31	0.4	0.41
Ti	0	0	0.01	0	0	0.01	0	0.01
Cr	0	0.02	0.01	0	0.02	0	0.04	0.02
Mg	1.93	1.6	1.8	0.74	1.43	1.38	2.01	2.15

APPENDIX C: IMAGE J RESULTS

The images uploaded to image J for particle analysis is presented below.

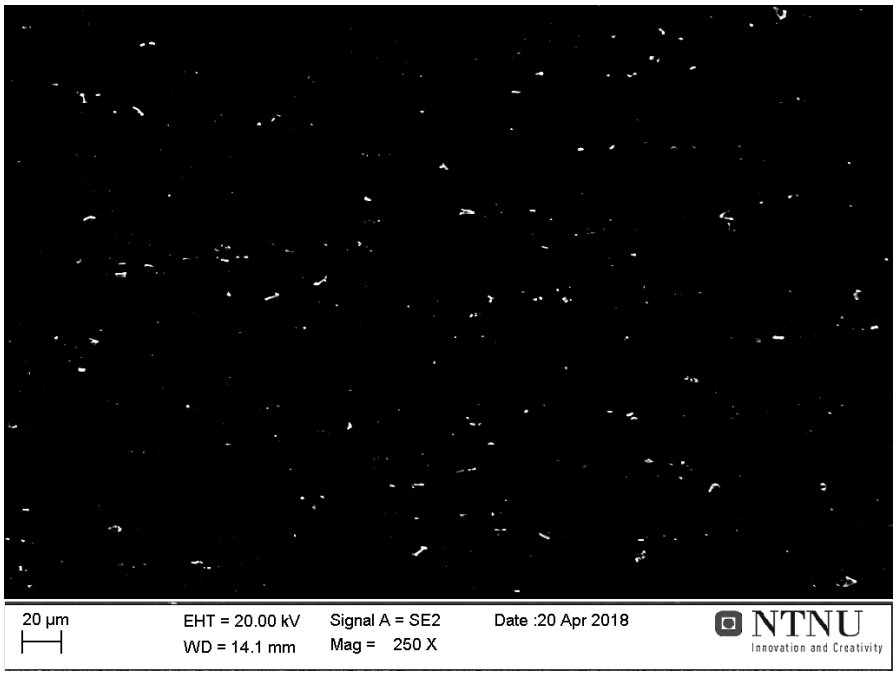

Figure 82: Particle distribution in extrusion plane.

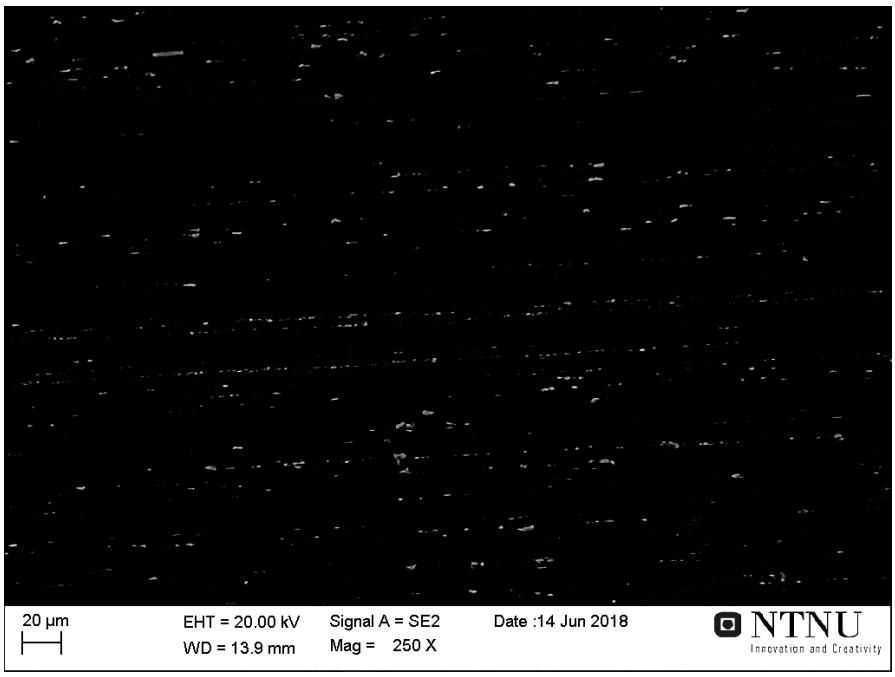

Figure 83: Particle distribution in longitudinal plane.

APPENDIX D: EBSD

The area scanned in order to generate the pole figure presented in section 4.3 is given in figure 84.

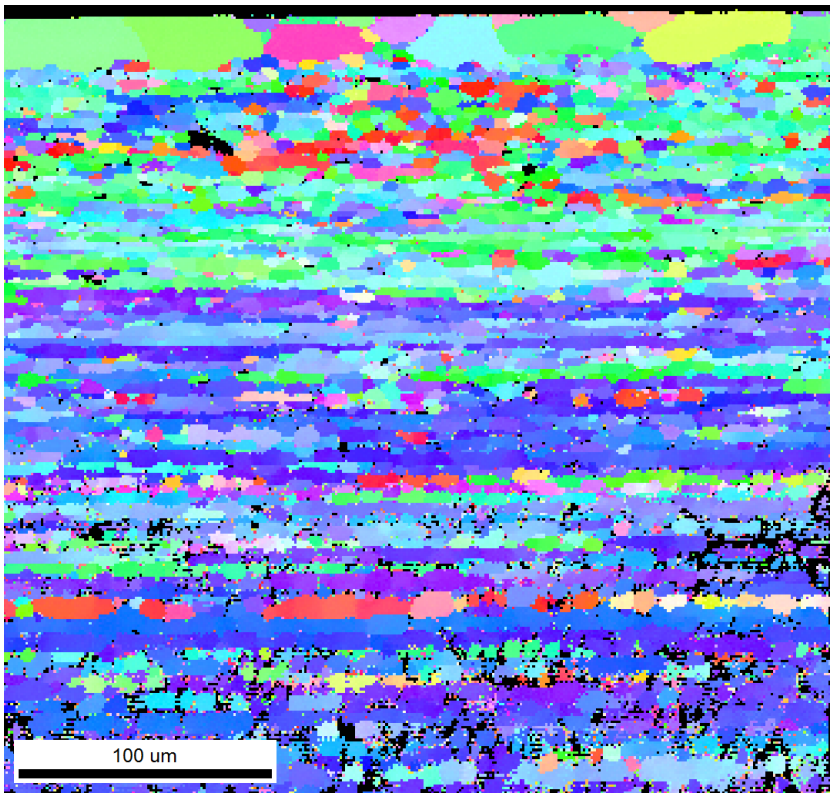

Figure 84: Area scanned to generate pole figure for 7046 alloy.